Objective Image Quality Assessment and Comparison of Ultrasound Probes

Research to Application of Trans-Balloon, Miniaturized TEE in Atrial Ablation Procedures.

L. Grandia

MSc Thesis

TU Delft Delft University of Technology

Delft Department of Biomedical Engineering

Objective Image Quality Assessment and Comparison of Ultrasound Probes

Research to Application of Trans-Balloon, Miniaturized TEE in Atrial Ablation Procedures.

MSc Thesis

L. Grandia

July 18, 2019

Faculty of Mechanical, Maritime and Materials Engineering (3mE) · Delft University of Technology

The work in this thesis was supported by Philips. Their cooperation is hereby gratefully acknowledged.

Abstract

Atrial Fibrillation (AF) is an abnormal heart rhythm that is characterized by rapid and irregular contraction of the atria. Irregular electrical activation occurs from the ostia of the Pulmonary Veins (PV), in the left atrium. AF is treated minimally invasive using catheter-based ablation of the tissue around the PV and posterior Left Atrium (LA) wall. Catheter-based ablation of the LA is a lengthy and complex procedure. Ablating the tissue too deep can induce atrioesophageal fistulas, which is a potentially fatal complication. Ablation needs to be performed accurately and at the right location to be successful. Therefore, real-time imaging of catheters and atrial anatomy is of great importance.

Currently, static 3D models of the left atrium are used for catheter navigation and ablation assistance during AF ablation procedures. However, since these models are not real-time, changes in the anatomy due to heart beating and ablation are not reflected in the model, which reduces the accuracy of these models. There is a continuous demand for real-time and more accurate imaging during AF ablation procedures.

In this thesis, it is proposed to use trans-balloon miniaturized Transesophageal Echocardiography (TEE) for real-time 3D imaging of the left atrium during AF ablation procedures. TEE imaging is a real-time ultrasound imaging modality for cardiac imaging. The TEE probe is inserted in the esophagus of the patient to acquire ultrasound images of the heart.

However, current state of the art TEE probes are not suited for real-time imaging of the left atrium during AF ablation procedures. First, due to the large diameter of the TEE probe, continuous long term imaging causes discomfort for the patient and increases the risk on laryngopharyngeal damage. Secondly, pressure of the TEE probe inside the esophagus, and the pressure and heat of the ablation catheter on the posterior LA wall increases the risk on atrioesophageal fistulas. Finally, the major practical limitation for application of TEE in AF ablation procedures is the limited Field of View (FOV). Since the esophagus direcly abuts the LA, the distance between the ostia of the PV and the transducer of the TEE probe is short. At this short distance, the conical shaped FOV is too narrow to include the ostia of the Left Superior Pulmonary Vein (LSPV), Left Inferior Pulmonary Vein (LIPV), Right Superior Pulmonary Vein (RSPV), Right Inferior Pulmonary Vein (RIPV) and a large part of the LA posterior wall entirely in the FOV. This limits the use of TEE for imaging of ablation procedures.

Therefore, it is proposed to use a novel, trans-balloon, miniaturized TEE technique for imaging of AF ablation procedures. The miniaturized probe decreases discomfort for the patient, and allows long term monitoring. The transducer of the miniaturized probe is inserted in a water-filled balloon that can be inflated and deflated. Inflating the water filled balloon in the esophagus provides acoustic coupling between transducer and the tissue, and allows to increase the distance between the transducer and anatomical landmarks of the LA. Furthermore, the water inside the balloon serves as a temperature buffer, which reduces the risk on atrioesophageal fistulas.

To investigate whether image quality of trans-balloon, miniaturized TEE is sufficient for imaging of AF ablation, image quality of a miniaturized ultrasound probe was compared to image quality of current state of the art TEE probes, and influence of the water filled balloon on image quality was investigated. A method for objective Image Quality Assessment (IQA) was developed and implemented to measure and quantify image quality. Image quality was assessed based on quantification of the contrast resolution, Contrast-to-Noise Ratio (CNR), spatial resolution and penetration depth of the ultrasound signal.

The study has shown that image quality of the miniaturized ultrasound probe is comparable to image quality of the current state of the art TEE probes. It was observed that the balloon had no negative impact on image quality, although this result is not clinically validated yet. Some limitations of the miniaturized ultrasound probe were discovered as well. The imaging depth of the miniaturized ultrasound probe is significantly less compared to the state of the art probes, but for application in AF ablation procedures this will not be a major limitation since the anatomical structures of interest are well within the imaging range. Furthermore it was observed that the spatial resolution of the miniaturized probe decreases with increasing image plane rotation angle. Rotating the imaging plane is common practice in TEE imaging, which means that rotation-dependent spatial resolution is undesired. It is therefore recommended to perform a review study involving clinical experts to judge whether image quality of the miniaturized ultrasound probe with rotated imaging plane is acceptable.

Despite these limitations, the results suggest that trans-balloon miniaturized TEE can provide real-time ultrasound imaging of the left atrium during ablation procedures. There is a continuous demand for more accurate and real-time imaging techniques during catheter based treatment of atrial fibrillation. The research in this thesis provides a theoretical framework to measure and compare image quality of ultrasound probes, which is an important first step in the development of a novel, real-time 3D imaging technique for imaging of AF ablation procedures.

Table of Contents

Acknowledgements

I would like to thank my supervisor Prof. dr. J. Dankelman for her assistance during the writing of this thesis, and I would like to thank Peter Vogels, Niels Nijhof and Andre van Doorn for their positive input, critical attitude and useful feedback during the writing of this thesis.

Delft, University of Technology L. Grandia
July 18, 2019

Chapter 1

Introduction to Thesis Assignment

Atrial fibrillation is an abnormal hearth rhythm that happens when the electrical activation of the atria is disturbed. Erroneous activation of the left atrium originates from the tissue where the pulmonary veins enter the left atrium. To stop atrial fibrillation, the tissue is electrically isolated by ablation of the tissue around the pulmonary veins. Atrial fibrillation ablation procedures are catheter-based, minimal invasive procedures that require imaging techniques to visualize the catheters and anatomy of the left atrium. Currently, navigation of the ablation catheters is based on a static 3D model of the left atrium that is acquired prior to the ablation. Since these models are not real-time, the anatomy of the left atrium is less accurate presented compared to real-time imaging techniques.

Transesophageal Echocardiography (TEE) is used for real-time ultrasound imaging of the heart. This thesis proposes miniaturized, trans-balloon TEE as real-time imaging technique during atrial fibrillation procedures. The goal of this thesis is to investigate whether image quality of trans-balloon miniaturized TEE is sufficient for intraprocedural imaging of atrial fibrillation ablation procedures. This chapter introduces the reader to the topic of this thesis. The principles of transesophageal echocardiographic imaging are explained, and the potential value of this imaging technique for atrial fibrillation ablation procedures is discussed. Finally, the research question is stated and the thesis outline is presented.

1-1 TEE Imaging

TEE is an imaging technique that is used for live ultrasound imaging of the heart. The term 'Transesophageal Echocardiography' means literally 'making ultrasound images of the heart (echocariography), through the esophagus (transesophageal)'. To acquire these ultrasound images, the TEE probe is inserted in the patient's oral cavity, navigated trough the pharynx and advanced down into the esophagus. When the probe is advanced to a sufficient depth in the esophagus, the probe tip is manipulated and rotated until the desired view is obtained [1, 2]. This section introduces the reader to the anatomy of the heart and esophagus, and explains how TEE imaging is used in clinical application.

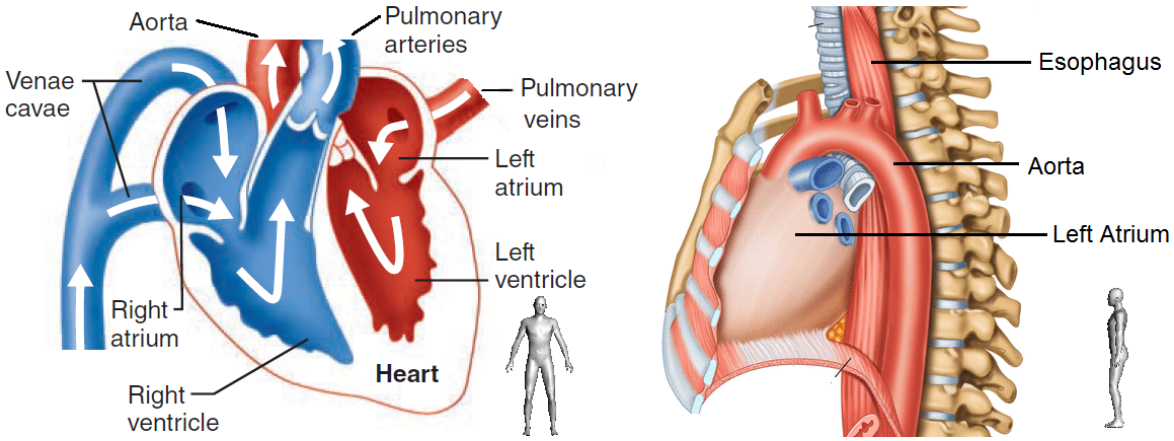

Figure 1-1: Schematic representation of the cardiac anatomy and bloodflow. Low oxygenated blood enters the right atrium via the vena cava, and is pumped into the right ventricle. The right ventricle pumps the blood to the lungs via the pulmonary arteries. Oxygenated blood enters the left ventricle via the pulmonary veins and left atrium. The left ventricle pumps oxygenated blood to the systemic circuit via the aorta. The esophagus passes the heart anteriorly, to the right side of the descending aorta. The posterior wall of the left atrium directly abuts the esophageal wall. Figure adapted from [3]

1-1-1 Heart, Esophagus and Anatomical Relation

The heart is a muscular organ that pumps blood through the human body. The heart is divided in four chambers: two atria, the Left Atrium (LA) and Right Atrium (RA) and two ventricles, the Left Ventricle (LV) and Right Ventricle (RV) respectively. Blood with low oxygen saturation from the systemic organs enters the RA via the superior and inferior vena cava. The RA pumps the low oxygenated blood into the RV. Contraction of the RV pumps the blood into the pulmonary system, where oxygen level in the blood rises. Oxygenated blood enters the LA via the four pulmonary veins: the Left Superior Pulmonary Vein (LSPV), Right Superior Pulmonary Vein (RSPV), Left Inferior Pulmonary Vein (LIPV) and Right Inferior Pulmonary Vein (RIPV) respectively. The LA pumps the oxygenated blood into the LV, and contraction of the LV pumps the blood into the systemic system. Backflow of blood is prevented by valves, the valve between the RA and RV is called the "tricuspid valve", and the valve between the LA and LV is called the "mitral valve". Backflow from the aorta in the LV is prevented by the "aortic valve". The anatomy and bloodflow of the heart is schematically represented in figure 1-1 [3]. Cardiac muscle cells have the unique property of autorhythmicity, which is the ability of spontaneous depolarization. The muscle cells in the heart contract as a response to impulses (action potentials) generated by pacemaker cells. Any disturbance in the electrical activation can lead to a disturbed contraction pattern of the heart. [4].

The esophagus is a muscular tube with a length of approximately 23 to 26 cm and diameter of approximately 17 to 19 mm, that connects the pharynx and stomach with each other, descending anteriorly to the vertebral column [5]. The upper part of the esophagus, the section just below the pharynx until the aortic arch, runs slightly to the left between the trachea and the vertebral column. It then passes behind the aortic arch and descends to the posterior mediastinum, along the right side of the descending thoracic aorta (see figure 1-1)

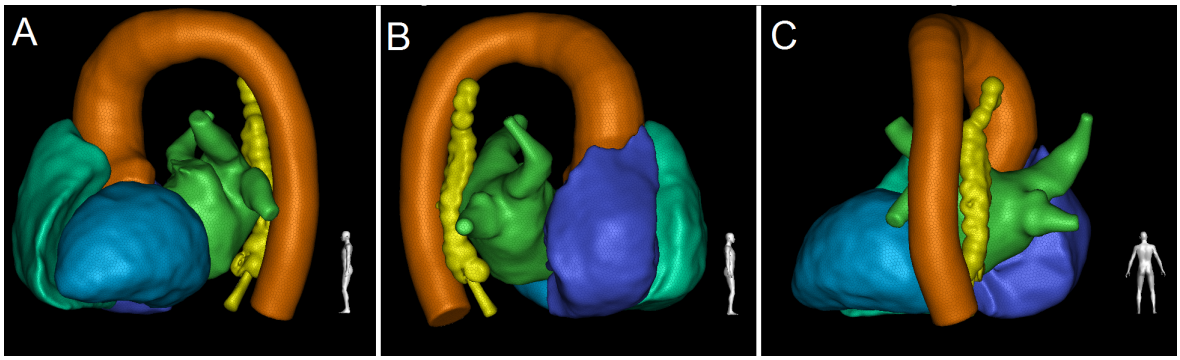

Figure 1-2: 3D segmentation of the heart and esophagus on a CT dataset. The esophagus (yellow) passes the heart posteriorly, to the right side of the descending aortic arch (orange). Part of the esophagus directly abuts the posterior wall of the left atrium (green). **A** Left view of the heart and esophagus. **B** Right view of the heart and esophagus. This view shows how the esophagus directly abuts the posterior left atrial wall. **C** Posterior view of the heart and esophagus. This view shows how the esophagus runs along the right side of the descending aortic arch.

[6].

The esophagus passes the heart posteriorly, where the posterior wall of the left atrium and the outer esophageal wall are abutting each other. The part of the esophagus that is in contact with the posterior left atrial wall has a length of approximately 45 mm [6]. The tissue thickness between the posterior LA wall and esophageal wall ranges from approximately 2 to 5mm [6]. Several studies have shown that in most cases ($> 60\%$) the esophagus passes at the left side or in the middle of the posterior left atrial wall [5, 6, 7]. Figure 1-2 shows a 3D model of the heart and esophagus, based on cardiac CT scans. The figure shows how the esophagus (yellow) anteriorly passes the left atrium (green), and that the space between the posterior LA wall and esophagus is very narrow.

1-1-2 TEE Imaging and Imaging Equipment

The TEE ultrasound probe consists of an ultrasound transducer on the distal end of a semi-flexible shaft that connects the transducer to the handle. Figure 1-3 shows an example of a TEE ultrasound probe (X8-2t, Philips, Reedsville, PA, USA). The ultrasound transducer acquires a 2D-imaging plane, or a 3D imaging volume. On the handle are turning wheels to manipulate the probe tip (flexing anteriorly, posteriorly, left and right), and buttons to rotate the imaging plane (0^o - 180^o). Turning the handle left or right turns the transducer left or right around the central axis of the probe, and pushing or pulling the handle advances or withdraws the ultrasound probe (figure 1-4).

The transducer at the distal end of the flexible shaft is pushed into the pharynx of a patient, and advanced down into the esophagus. When the probe is at sufficient depth in the esophagus, the tip of the probe is manipulated such that the transducer faces the heart and is pressed against the esophageal wall (figure 1-5). This is required to ensure acoustic coupling between the transducer and the tissue. When there is an air pocket between the esophageal wall and the transducer of the TEE probe, it is impossible to clearly visualize the heart on the ultrasound image. An example of a TEE ultrasound image is shown in figure 1-6.

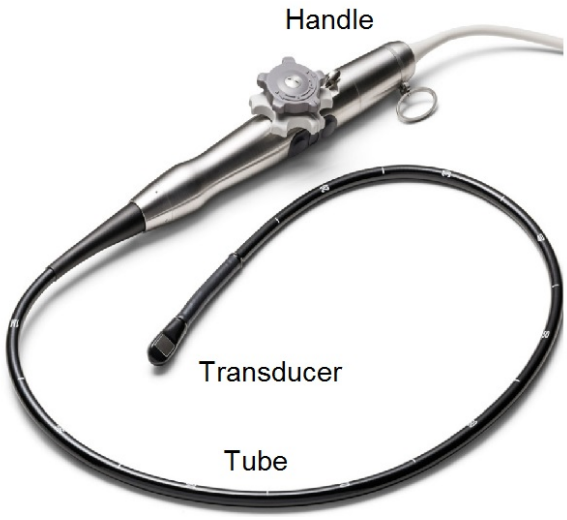

Figure 1-3: Example of a TEE probe (X8-2t, Philips, Reedsville, PA, USA). On the handle are buttons to manipulate the probe tip, and rotate the imaging plane. The transducer is located at the proximal end of the tube that is inserted in the esophagus. Figure adapted from [8].

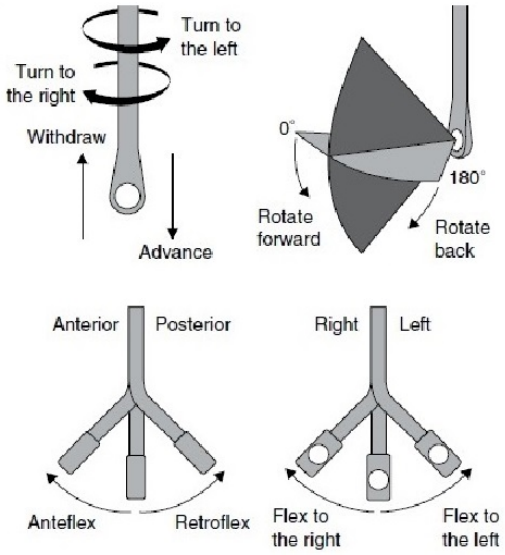

Figure 1-4: Degrees of freedom of the TEE probe. Pushing or pulling the handle advances and withdraws the transducer. Rotating the handle rotates the entire probe around its central axis. The imaging plane can be rotated 0° - 180°. The transducer on the distal end of the shaft can be flexed anteriorly, posteriorly, left and right. Figure adapted from [2].

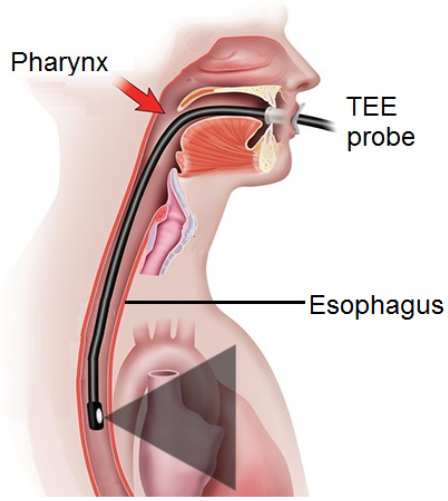

Figure 1-5: Schematic representation of the TEE probe inserted in the esophagus of the patient. The transducer faces the heart, and is pressed against the esophageal wall for ultrasound imaging. Figure adapted from [2].

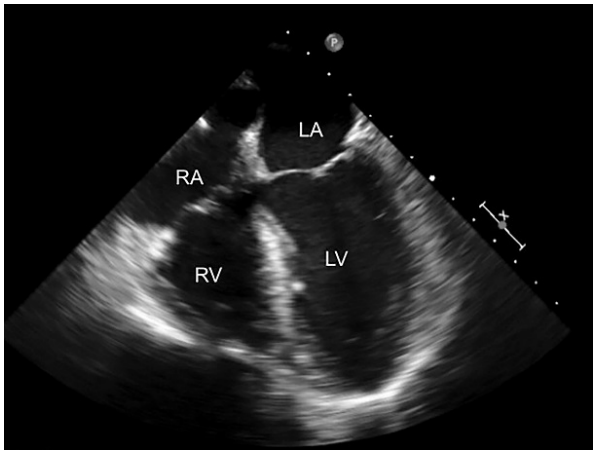

Figure 1-6: Example of a 2D ultrasound image acquired using TEE imaging. The left atrium (LA), right atrium (RA), left ventricle (LV) and right ventricle (RV) are shown.

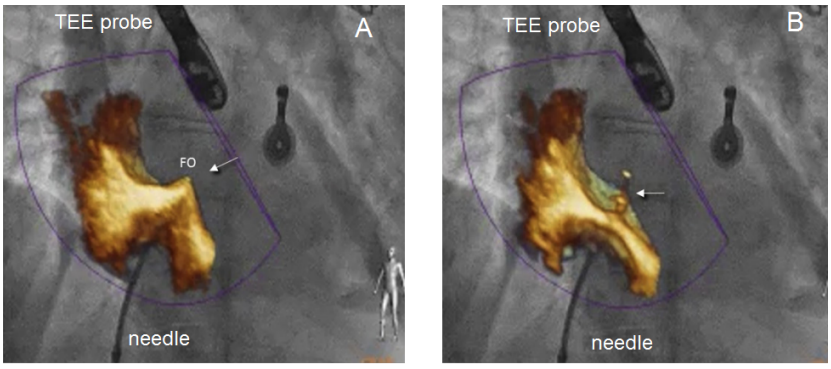

Figure 1-7: Example of ultrasound and fluoroscopy fusion imaging during transseptal puncture. The position of the neelde is visualized with fluoroscopy, and the required position for puncturing (FO) are visualized with the ultrasound images of the TEE probe. **A:** situation just before puncture. **B:** situation after succesfull puncture of the septum Figure adapted from [14].

1-1-3 Clinical Relevance and State of the Art Application of TEE

TEE is a low-risk, non-invasive imaging technique that can provide real-time high-quality anatomic imaging of the heart without using ionizing radiation [1, 9]. The non-invasive and low-risk character of TEE combined with the high clinical relevance of the ultrasound images makes TEE imaging a widely used imaging application that is used in many Structural Heart Disease (SHD) procedures. Examples of SHD procedures where TEE is used are minimal invasive replacement of the mitral valve, tricuspid valve or aortic valve [10, 11, 12]. TEE is used both preprocedural to assess the anatomy and for treatment planning [11, 10], and intraprocedural for navigation and visulasation of instruments relative to the coronary anatomy [13].

Current state of the art TEE probes are capable of 2D-, 3D-, and doppler ultrasound imaging. During catheter-based structural heart disease interventions, fusion imaging of ultrasound and fluoroscopy is applied to visualize both the catheters and the soft tissue in one image. The ultrasound image plane (2D) or volume (3D) obtained with the TEE probe provides detailed information about the cardiac structure and soft anatomy. The fluoroscopy images clearly visualizes the position of the catheters and instruments in 3D space. Real-time overlay of the ultrasound and fluoroscopy images allows to precisely navigate the instruments relative to the cardiac structure [14]. Figure 1-7 shows an example of fused ultrasound and fluoroscopy imaging (EchoNavigator, Philips, Best, Netherlands). The figure shows the transseptal puncture procedure, which requires precise placement of the needle to puncture the septum at the right place.

1-2 Application of TEE in Atrial Ablation Procedures

Although TEE imaging is a relatively safe and non-invasive imaging technique that provides real-time imaging of the cardiac structure, it is currently not commonly used for intraprocedural imaging of Atrial Fibrillation (AF) ablation procedures. During AF ablation procedures, atrial fibrillation is treated by ablation of the posterior LA wall, and ostia of the Pulmonary

Veins (PV) [15, 16, 17]. This is a catheter based minimal invasive procedure, which requires imaging of cardiac structures and instruments. This section discusses the practical and safety-related issues that limit the use of TEE for cardiac imaging during AF ablation procedures.

1-2-1 Atrial Fibrillation

Atrial fibrillation occurs when the atria are rapidly and irregularly contracting, with rates of 400 up to 600 contractions per minute [18, 17]. Normally, contraction of the heart is regulated by the sinoatrial (SA) node. Electrical initiation of the SA node causes the atria to contract. The electrical activation is conducted to the ventricles via the atrioventricular (AV) node and the Purkinje fibers. The subsequent activation of atria and ventricles pumps the blood through the body.

During atrial fibrillation, the electrical activation pattern of the atria is disturbed. Most of the irregularities are altered by the AV node, but still some propagate to the ventricles causing the heart beat to rise. The exact cause of AF is not fully understood yet, but in most cases it is triggered by rapidly firing electrical sources at the ostia of the PV [17]. Symptoms of AF vary between patients and can range from fatigue, shortness of breath, irregular heart beat, and chest pain up to heart failure [4].

1-2-2 Treatment of Atrial Fibrillation

Treatment of AF is done either pharmacological, with open surgery or minimal invasive with an electrophysiology (EP) procedure [4, 17]. Pharmacological treatment includes daily administration of anticoagulant to prevent formation of blood clots in the atria, and antiarrhythmic drugs to regulate the heart rate [17]. Another treatment to stop AF is an open surgery called the "Cox-Maze-III" procedure. During this open heart surgery, scar tissue is created around certain areas of the atrium to electrically isolate these and stop erroneous activation. This procedure is effective with succes rates above 90% but it is invasive and the accompanying risk make this procedure unsuitable for a large group of patients [19].

Due to the invasive character and high risk of the Cox-Maze-III procedure, most AF treatment procedures are performed minimally invasive using catheter ablation. During this procedure, erroneous activation of the atria is stopped by creating small lesions using RF-ablation catheters. The catheters are inserted via the groin, and enter the right atrium via the vena cava (see figure 1-8). The left atrium, where most of the ablations are done, is entered via a transseptal puncture [17, 14]. Since AF usually originates from electrical activation of the pulmonary veins, ablation is performed by encircling the ostia of the PV and, in some cases, also by linear ablation of the LA roof and posterior wall [20, 21, 22, 23]. The ablation spots are indicated figure 1-9.

AF ablation is a lengthy and complex procedure, that can take about 3 to 6 hours. The variable anatomy of the pulmonary veins, and the close proximity of the esophagus to the left atrial wall increases the risk of complications [24]. Ablating the tissue of the posterior LA wall too deep, can induce so called "atrio-esophageal fistulas". This is a puncture through the LA wall into the esophagus, which is a potentially fatal complication. It is therefore crucial to ablate accurately and at the right location.

1-2-3 Imaging during Atrial Ablation Procedures

Since ablation needs to be performed at the right spot to effectively stop the atrial fibrillation, visualization of both catheters and the anatomy is of great importance [22]. Several techniques exist for imaging during AF ablation proceduers. One technique uses Computerized Tomography (CT), Magnetic Resonance Imaging (MRI) or rotational angiography to generate a 3D model of the left atrium [24, 17, 22]. This model is superimposed on the fluoroscopic images during the procedure. Ablation catheters are monitored real-time on the fluoroscopy images, and the superimposed 3D model shows the position of these catheters relative to the LA anatomy. Figure 1-10 shows a 3D model of the LA that was acquired using CT imaging.

A more recent and common imaging technique is so called "Fast Anatomical Mapping (FAM)", where a special mapping catheter is used to generate a 3D model of the atrium. The tip of the mapping catheter is tracked using electromagnetic signals that are detected with three coils that are placed on the patient. The 3D model of the LA is obtained through acquisition of points when the mapping catheter is in touch with endocardium. A greater number of points leads to a more accurate model of the atrium, but compared to the CT models the accuracy is inferior [25]. The advantage of the FAM technique is that tracking of the ablation catheter is also done with the electromagnetic signals, which eliminates the need for fluoroscopy to visualize the ablation catheters. Figure 1-11 shows a FAM-generated model of the LA.

Although use of the 3D models has shown to be effective and helpful during EP procedures [24], this technique also has some limitations. First, the CT, MRI or FAM acquired 3D models are not real-time acquired, but are usually acquired prior to the ablation. This means that these models are static, and that changes in the atrial anatomy due to heart beating and breathing of the patient are not reflected in the model. This reduces the precision of the 3D model with respect to the actual physiological state [4]. Furthermore, the effect of the ablation on the tissue cannot be visualized using these models. Besides that, preprocedural generated models using CT or MRI brings additional costs and significant radiation burden in case of CT imaging [4, 22, 20].

1-2-4 Current Status of TEE in Atrial Ablation Procedures

TEE is an imaging technique that can provide real-time, accurate 3D images of the cardiac structure. Therefore, it was already suggested by Kettering et al. (2017) to use TEE for imaging of the left atrium during AF ablation, and Haak, A. (2015) investigated TEE for intraprocedural imaging during AF ablation procedures in his PhD thesis [22, 4]. Also Faletra et al. (2013) have published several articles where they investigate the potential use of TEE during AF ablation procedures [23].

Currently, TEE is used mainly preprocedural for assessment of the LA anatomy, and to exclude thrombus in the LA appendage (LAA). Patients suffering from AF have an increased risk on formation of blood clots, especially in the LAA. Since these blood clots can cause stroke, scanning on thrombus in the LAA is an standard procedure before AF ablation procedures [27, 28, 24]. Furthermore, TEE is in some cases also used for transseptal puncture guidance, as this is required to navigate the ablation catheter from the RV to the LV [28, 24].

Although preprocedural use of TEE is common, the intraprocedural use for visualization of anatomy and catheter guidance during the ablation procedure is not yet applied due to both

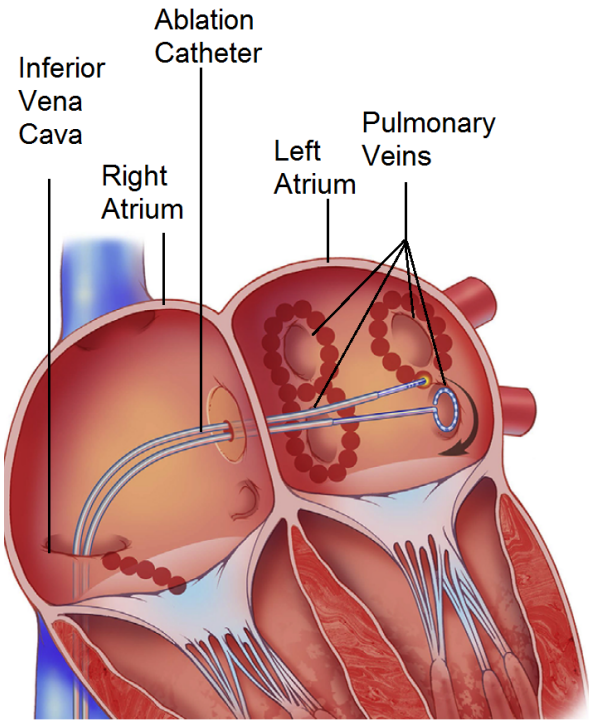

Figure 1-8: Atrial fibrillation is stopped by ablating the tissue around the ostia of the pulmonary veins. The catheters enter the right atrium via the inferior vena cava. The left atrium is accessed via a transseptal puncture. Figure adapted from [26]

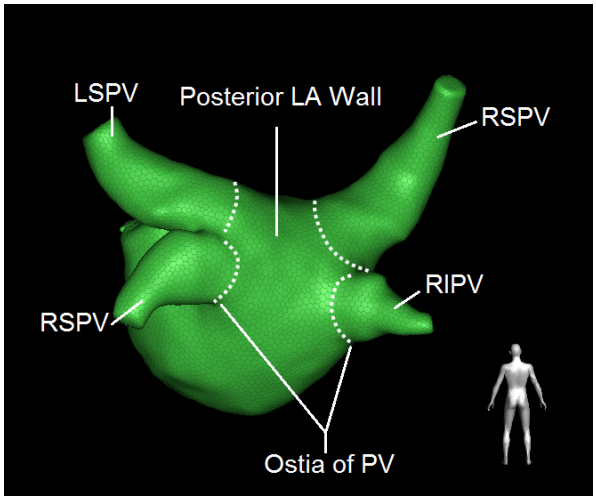

Figure 1-9: Posterior view of a 3D model of the left atrium. The four pulmonary veins and posterior left atrial wall are indicated (LSPV: Left Superior Pulmonary Vein, LIPV: Left Inferior Pulmonary Vein, RSPV: Right Superior Pulmonary Vein, RIPV: Right Inferior Pulmonary Vein). The ostia of the PV is indicated with the dotted lines. Ablation is performed at the ostia of the PV and in some cases also at the posterior LA wall.

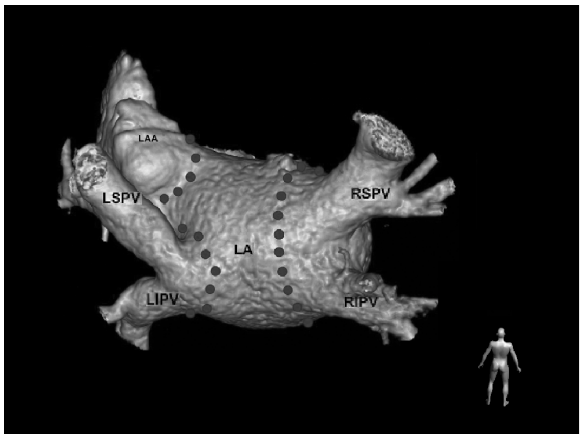

Figure 1-10: Posterior view of a CT-generated 3D model of the left atrium. Figure adapted from [24].

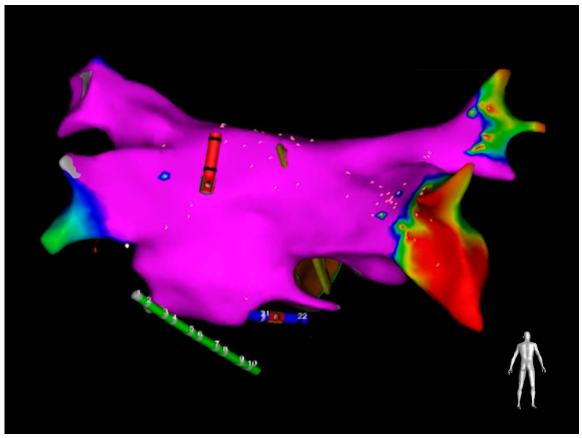

Figure 1-11: Posterior view of a FAM-generated 3D model of the left atrium. Figure adapted from [25].

Table 1-1: Distance (d) of the posterior LA wall and the ostia of the 4 PV to the esophageal wall (LSPV: Left Superior Pulmonary Vein, LIPV: Left Inferior Pulmonary Vein, RSPV: Right Superior Pulmonary Vein, RIPV: Right Inferior Pulmonary Vein). Table is adapted from [7].

Anatomical Strucure	**Distance to esophageal wall** (d) **[mm]**
Posterior LA wall	$2-5$
LSPV	$8-14$
LIPV	$3-11$
RSPV	$20-30$
RIPV	$16-20$

practical and safety-related issues. First, due to the relatively large size of the TEE probe, monitoring during the full length of an AF ablation procedure would be of great discomfort for the non-sedated patient and increases the risk on laryngopharyngeal damage [4, 28, 24, 23]. Besides that, there are also some distinct aspects of potential thermal injury for patients undergoing extensive atrial ablation. As already mentioned, the esophagus and posterior left atrial wall are directly abutting each other. The minor pressure of the TEE transducer from the esophagus on one side, and the pressure and heat of the ablation catheter on the other side might increase the risk on atrio-esophageal fistula (i.e. penetration of the left atrial wall into the esophageal wall), a potentially fatal complication [29, 30, 23].

Besides these safety-related issues, the main practical issue that limits use of TEE for intraprocedural imaging of AF ablation procedures is the limited Field of View (FOV) of the TEE probe. The TEE probe produces a conical shaped 3D volume, or triangular 2D imaging plane, with the origin located near the transducer surface. Especially close to the origin, (the "near field"), the FOV of is very limited [30].
Since the transducer of the TEE probe needs to be in contact with the esophagus, and the esophagus directly abuts the posterior LA wall, the transducer is always close to the LA wall and PV [6, 5, 7]. The distance (d) of the esophageal wall to these landmarks is listed in table 1-1. The close proximity of the esophagus to the left atrial wall places severe limitations on imaging any extent of the left atrial wall and PV since these anatomical structures appear in the narrow near field of the ultrasound image, and will be partly outside the FOV [14, 4, 30].

A research to the visibility of left atrial anatomy on 3D TEE was conducted by A. Haak (2015), where he concluded the following: "The atrial anatomy such as the pulmonary veins, the atrial appendages, and the atrial septum are of importance for AF ablations. It has been shown that these landmarks can be visualized with 3D TEE. However, (...) landmarks such as the pulmonary veins may not always be visible. Secondly, the atria are in the near field of the TEE probe and especially the left atrium is impossible to image entirely with a single 3D view. (...) The posterior wall of LA was always lost in the 3D TEE datasets, because the currently used matrix TEE probe (Philips CX7-2t) is not capable of visualising the structures in the very near field of the ultrasound beam." [4].

Figure 1-12 shows an example that illustrates above mentioned limitations of the TEE FOV. The 2D and 3D FOV of standard TEE probe (X8-2t, Philips) was simulated using a 3D model of the esophagus and LA. The figure shows that the LA is partly outside the FOV, especially the posterior atrial wall and ostia of some of the PV. This example supports the conclusion of Haak (2015) that it is impossible to entirely image the LA with 3D TEE.

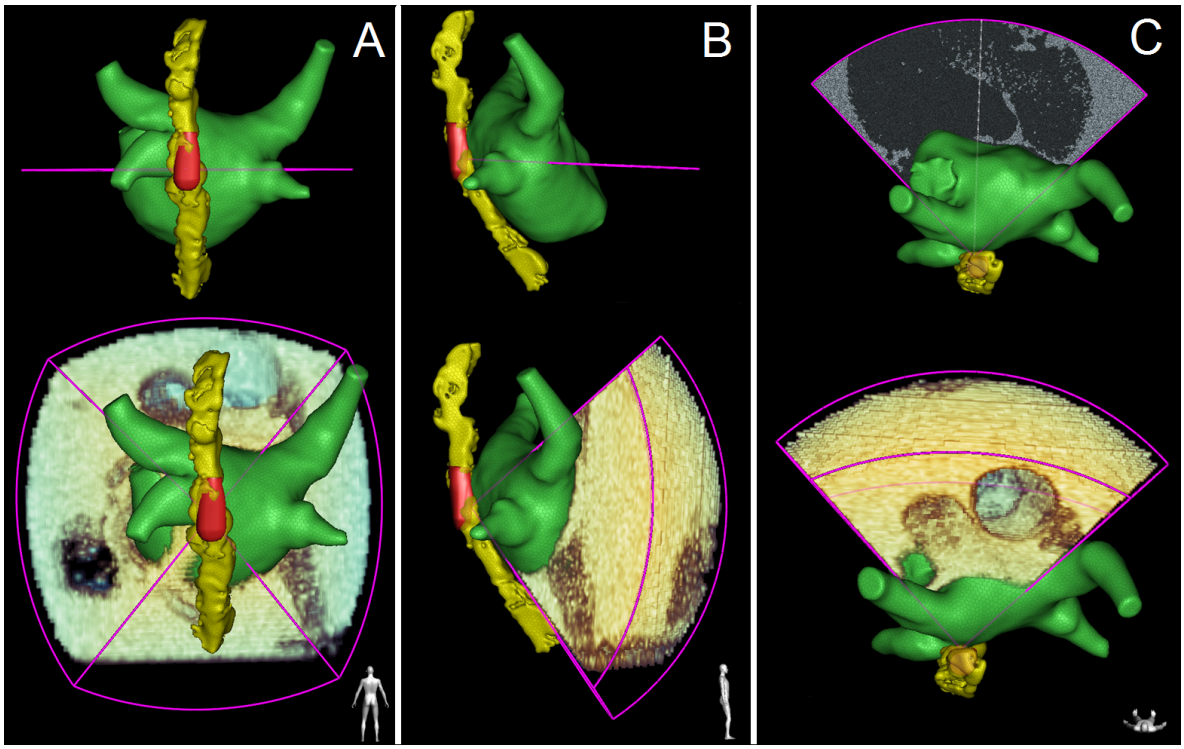

Figure 1-12: A: Simulated 2D and 3D view of a standard TEE probe (Cardiac Navigator, Philips, Best, the Netherlands). The 3D model of the left atrium and esophagus is based on a 3D CT dataset. The LA is shown in green, esophagus in yellow and the probe in red. **A:** posterior view of the simulated probe. **B:** right view on the simulated probe. **C:** top view of the simulated probe in the esophagus. This image shows that the posterior atrial wall, and part of the PV are outside the 2D and 3D FOV due to the narrow FOV close to the transducer.

1-3 Improve Atrial Ablation Procedures using Miniaturized TEE

The safety-related and practical limitations of TEE mentioned in the previous section limit the use of TEE for intra-procedural monitoring of AF ablation procedures. However, TEE has significant clinical relevance as it is able to provide non-invasive, real-time imaging of the cardiac anatomy, without using ionizing radiation as explained in section 1-1-3. Real-time, accurate imaging of the cardiac structure is of great clinical relevance, and could improve outcomes and efficacy of AF ablation procedures significantly, as this requires precise localization of catheters with respect to the cardiac anatomy. Therefore, intraprocedural TEE imaging could still be of great importance for AF ablation procedures, when it is used in a way that excludes the limitations explained in section 1-2-4. To make TEE a suitable method for intraprocedural imaging of AF ablation procedures, some adaptations to the standard TEE probes are required.

First, as mentioned earlier, the ablation procedures are very lengthy and can take up to 6 hours. Therefore, the standard TEE probes cannot be used, as the large diameter of the probe causes great discomfort for the patient when it is in place for such a long time [4, 28, 24]. There are already some smaller TEE probes at the market (mini-TEE, micro-TEE, Philips), and several studies have shown that patient comfort increases markedly, and long term monitoring

is possible using smaller TEE probes [28, 31].

Secondly, apart from the perspective of patient comfort, also the FOV has to be improved to make TEE useful for monitoring of AF ablation procedures. As already mentioned in section 1-2, direct contact between esophageal wall and transducer is required for TEE imaging. Therefore, the LA is always in the near-field of the ultrasound image. Furthermore, with miniaturized TEE probes, the transducer area is smaller, and maintaining tissue contact within the esophagus will be even more challenging. A possible way to facilitate better acoustic coupling between the transducer and esophagus, is to insert the transducer of the miniaturized TEE probe in a balloon, and inflate the balloon with water. The water-filled balloon acts as a coupling medium between the esophageal wall and transducer, and the articulated transducer tip can be rotated, flexed and moved within the balloon without loosing acoustic coupling with the tissue. This method potentially increases the clinical relevance of TEE imaging as it allows to increase the distance between the esophageal wall and the transducer, which reduces the near-field issues as described by Haak (2015). Next to its function as an acoustic coupling medium, the water inside the balloon serves as a temperature buffer, which potentially reduces the change on thermal injury of the esophageal wall due to the increased temperature of atrial ablation. The method to use a water-filled balloon as a coupling medium between the tissue and transducer is already applied in endoscopic ultrasound applications, but use of a balloon to assist for miniaturized TEE imaging is not yet described in literature [32, 33].

With above mentioned adaptations, TEE could be a valuable imaging tool for intraprocedural imaging of AF ablation procedures. The ultrasound image of the TEE probe can provide real-time visual feedback of the left atrial anatomy, which is currently not possible with preprocedural generated 3D models of the LA. Miniaturization of the TEE probe reduces discomfort for the patient, and a water-filled balloon around the transducer facilitates the possibility to create a distance between the transducer and esophageal wall, while acoustic coupling is maintained. This increases visibility of the posterior LA wall and pulmonary veins in the ultrasound FOV.

Figure 1-13 shows the FOV improvement of trans-balloon miniaturized TEE compared to conventional TEE. With conventional TEE, the transducer is pressed against the esophageal wall resulting in a short distance d to the left atrium. Since the esophagus has a diameter of approximately 20 mm, the distance between the transducer and esophageal wall can be increased with approximately 20 mm using a water-filled balloon. Figure 1-13A shows the situation for conventional TEE imaging. In this case, the ostia of the PV and posterior LA wall are outside the FOV. Figure 1-13B shows the situation for trans-balloon miniaturized TEE imaging. With increased distance between the esopheal wall, the FOV covers the ostia of the PV and posterior LA wall.

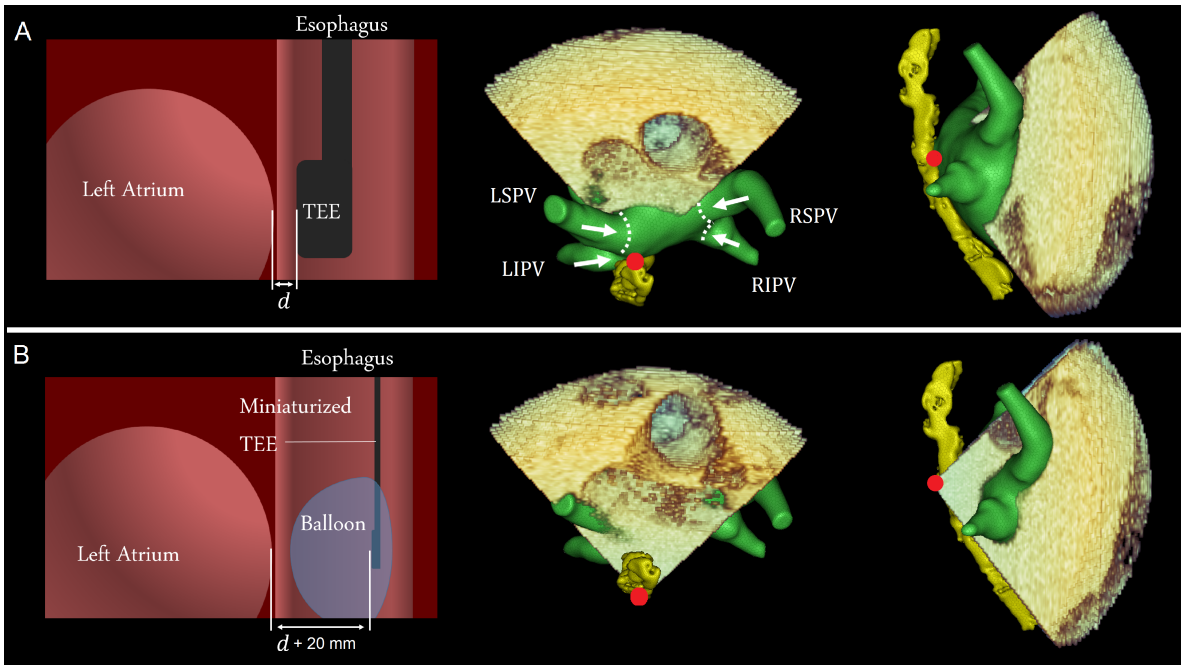

Figure 1-13: **A:** With conventional TEE imaging, the distance d between transducer and left atrium is very short. The simulated FOV shows that ostia of the Left Superior Pulmonary Vein (LSPV), Left Inferior Pulmonary Vein (LIPV), Right Superior Pulmonary Vein (RSPV) and Right Inferior Pulmonary Vein (RIPV) are not within the FOV. The probe position is indicated with the red dot. **B** With trans-balloon miniaturized TEE imaging, the distance d between transducer and left atrium is increased with approximately 20 mm. The simulated FOV shows that LSPV, LIPV, RSPV and RIPV are covered in the FOV when the distance d is increased with approximately 20 mm.

1-4 Definition of Thesis Research Scope

The preceding sections have shown the current state of the art application of TEE imaging, and its limitations during AF ablation. Furthermore, it was shown that clinical value of TEE imaging during AF ablation procedures could improve markedly when more of the LA and PV anatomy is visible in the ultrasound image. The proposed solution to achieve better visualization of the atrial anatomy is to apply a water-filled balloon around the transducer of a miniaturized TEE probe. This balloon acts as a coupling medium between the transducer and esophagus, and eliminates the need to press the transducer against the esophageal wall to achieve acoustic coupling. Application of this method allows to increase the distance between the transducer and esophageal wall, and brings the anatomical structures of interest for AF ablation further into the FOV.

Since this method is entirely new within the application of TEE imaging, and not yet investigated on large scale, many open questions remain before this method can be applied in a clinical setting. Questions that need to be answered are:

1. Is acoustic coupling in the esophagus attainable using a water filled balloon around the tip of the ultrasound transducer?

2. Can the system maintain this coupling, and is it possible to manipulate the balloon inside the esophagus?

3. Is it possible to manipulate the probe tip inside the balloon to view different cardiac structures?

4. Is image quality and depth of miniaturized TEE probes sufficient for imaging of cardiac structures?

5. How is image quality affected by the water-filled balloon around the transducer?

Next to these questions, also the clinical safety and applicability of this method has to be investigated. Since answering all these questions is not possible in the limited time frame available for this thesis work, a research scope has to be defined. Some of the above mentioned questions were already investigated in a preliminary study of Philips Research North America (PRNA), Cambridge. In this preliminary study, Balicki, M., Sutton, J., Stanton, D., Buizza, R. Kyne, S. and Raju, B. (PRNA, 2018) investigated whether stable acoustic coupling using trans-balloon miniaturized TEE is possible. In their research, they showed that it was possible to introduce a small ultrasound catheter in a sheath, with a water-filled balloon at the distal end of the sheath. They introduced the sheath and catheter in the esophagus of a phantom model, and successfully obtained acoustic coupling between transducer and esophageal wall of the phantom. Furthermore, they showed that flexion, rotation and advancing of the probe inside the balloon is possible, while stable acoustic coupling was maintained. The results of this preliminary study show that a water-filled balloon around the transducer of a miniaturized echocardiographic catheter can serve as acoustic coupling medium.

1-4-1 Research Scope

The preliminary study of Balicki et al. did not address quantification of image quality of the trans-balloon miniaturized ultrasound probe. To investigate whether trans-balloon, miniaturized TEE image quality is sufficient for intraprocedural monitoring of AF ablation procedures, the image quality of trans-balloon miniaturized TEE has to be compared to image quality of current state of the art TEE probes.

Therefore, this thesis focuses on quantification and comparison of image quality of the miniaturized TEE probe and the current state of the art TEE probes. The scope of this thesis is confined to the following items:

1. Development of a method to objectively compare image quality of ultrasound probes.
2. Objective image quality comparison of the standard TEE probes and miniaturized TEE probe using the developed image quality assessment method.
3. Investigation to the effect of a balloon on image quality of the miniaturized TEE probe using the developed image quality assessment method.

1-4-2 Research Questions

Main question The main question that is answered in this thesis work is:

> *Is image quality of trans-balloon, miniaturized ultrasound probes sufficient for transesophageal echocardiograpic imaging during atrial fibrillation ablation procedures?*

Sub-questions The main question is subdivided in the following sub-questions

- Sub-question 1: *What is image quality of the miniaturized ultrasound probe compared to the image quality of the currently used standard TEE probes?*
- Sub-question 2: *How does a transducer balloon influence the image quality of the miniaturized ultrasound probe?*

1-5 Thesis Outline

This thesis has the following structure. Chapter 2 introduces the reader to the topic of ultrasound, and explains the basic principles of ultrasound physics, equipment and image acquisition. Chapter 3 presents the image quality assessment method that was developed to compare image quality of the miniaturized, trans-balloon probe to the conventional TEE probes. In chapter 4, the research method is explained. Chapter 5 contains the results of the image quality measurements, and these results are discussed in chapter 6. Chapter 7 presents the conclusion, which answers the main question of this thesis. Appendix A and B present the measurement method and results in a summarizing article. Appendix C contains details of the measurement setup.

Chapter 2

Fundamental Principles of Ultrasound Imaging

This chapter introduces the reader to the basic principles of ultrasound imaging. It contains an introduction to the fundamental ultrasound physics and interaction of ultrasound waves with the insonated tissue. Furthermore, it is explained how the echo signal is obtained using transducers, and how the signal is converted to a 2D image. This chapter provides the background information for a basic understanding of the following chapters in this thesis.

2-1 Ultrasound Physics

2-1-1 Wavelength, Frequency and Speed

Ultrasound waves are generated by compression and rarefaction of a medium. Compression of a medium results in a region with a high pressure, and rarefaction results in a region with low pressure relative to the surrounding medium. One cycle of compression and rarefaction is defined as a 'wave'. The wavelength (λ) is defined as the distance between two pressure peaks in the medium. The frequency (f) is the number of times the wave oscillates per second. Ultrasound waves oscillate with a frequency above 20 kHz. Medical ultrasound usually has a frequency around 2 to 10 Mhz. The speed of sound (c) is the distance traveled by the wave per unit time, and is related to the speed of sound and wavelength according to equation 2-1:

$$c = \lambda \cdot f \tag{2-1}$$

The frequency of the ultrasound waves never changes, but the speed of sound does change within different media.

2-1-2 Ultrasound Intensity, and the dB Scale

The areas of compression and rarefaction in the ultrasound wave cause variations in local pressure amplitude, (P) in the medium. The pressure amplitude of an ultrasound wave is defined as the peak maximum (or minimum) in the pressure with respect to the surrounding medium. The intensity (I) of the ultrasound beam is the amount of power per unit area, and is proportional to the square of the pressure amplitude ($I \propto P^2$). The intensity is always measured relative to a reference intensity (e.g.: The intensity of the returning echo with respect to the intensity of the incident ultrasound signal.). The relative intensity between two ultrasound signals with intensity (I_1 and I_2) expressed in dB is defined as:

$$\text{relative intensity (dB)} = 10 \cdot \log\left(\frac{I_2}{I_1}\right) \tag{2-2}$$

2-1-3 Ultrasound Interaction with Matter

The ultrasound waves have various modes of interaction as they propagate trough the insonated medium. Each mode of interaction (reflection, refraction, scattering and absorption) is shortly discussed in this section.

Reflection

Reflection occurs at the boundary between two media with different acoustic impedance (Z) (e.g. the boundary between an organ and surrounding tissue). When an incident ultrasound beam is perpendicular to the boundary, a fraction of the beam is reflected (an echo), and a fraction is transmitted in the adjacent medium. The fraction of the incident intensity that is reflected is determined by the intensity reflection coefficient (R_I). A large difference in acoustic impedance, results in a high intensity reflection coefficient, which results in a large reflected fraction of the incident ultrasound signal. The intensity reflection coefficient is defined as:

$$R_I = \frac{I_r}{I_i} = \left(\frac{Z_2 - Z_1}{Z_2 + Z_1}\right)^2 \tag{2-3}$$

The acoustic impedance difference between air and tissue is very large, resulting in an intensity reflection coefficient of almost one. This means that almost all ultrasound energy is reflected on an air-tissue boundary, which makes it impossible to see structures behind the boundary. Therefore, acoustic coupling gel is applied between the transducer and the insonated tissue to eliminate air pockets.

Nonperpendicular incident ultrasound waves are reflected at an angle θ_r equal to the incident angle, $\theta_i = \theta_r$. The echos are directed away from the transducer, and thus undetected (figure 2-1B).

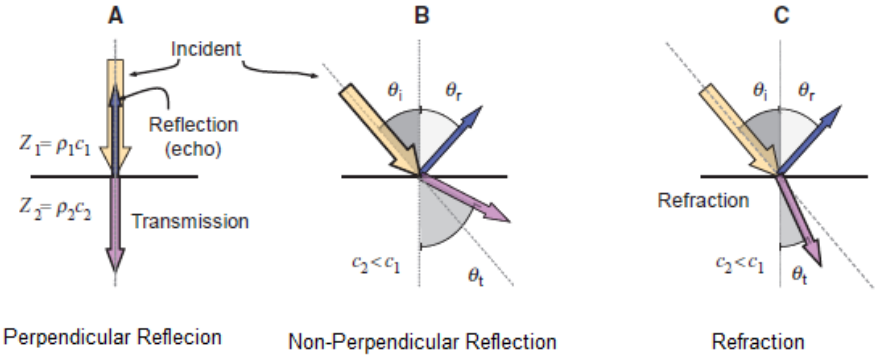

Figure 2-1: **A:** Perpendicular reflection. Ratio between the reflected intensity and incident intensity is the reflection coefficient (R_I). The transmitted intensity equals the difference between the incident and the reflected intensity. **B:** Non-perpendicular reflection. The incident angle equals the reflection angle ($\theta_i = \theta_r$). **C:** Refraction refers to the change in direction of the transmitted ultrasound beam. Figure adapted from [9].

Refraction

Refraction refers to the change in direction when an ultrasound beam propagates from one medium to another with a different speed of sound. The angle of incidence (θ_i) and refraction (θ_t) are measured relative to the axis perpendicular to the boundary, as shown in figure 2-1C. The angle of refraction depends on the angle of incidence, and the speed of sound in the two media, c_1 and c_2:

$$\frac{\sin(\theta_t)}{\sin(\theta_i)} = \frac{c_2}{c_1} \tag{2-4}$$

Scattering

Scattering arises from reflections of objects within the tissue that are of equal or smaller size as the wavelength of the ultrasound signal. Specular (smooth) reflectors are reflectors with dimensions much larger than the wavelength, and reflect the sound in only one direction (similar to reflection of light in a mirror). Non-specular reflectors reflect the sound in all directions, and consequently, the echo of a nonspecular reflector is of lower intensity than the echo of a specular reflector. Contrary to the specular reflectors, the intensity of the returning echo is independent of angle of incidence (see figure 2-2).

Attenuation

Ultrasound attenuation refers to the loss of intensity of the ultrasound signal with distance traveled. Attenuation is caused mainly by absorption and scattering of the ultrasound signal. Ultrasound attenuation is expressed as the intensity of the ultrasound signal at a given depth (I) relative to the initial intensity (I_0). Usually, the ratio (I/I_0) is expressed in decibel, and is proportional to the product of probe frequency (f) expressed in MHz, the frequency

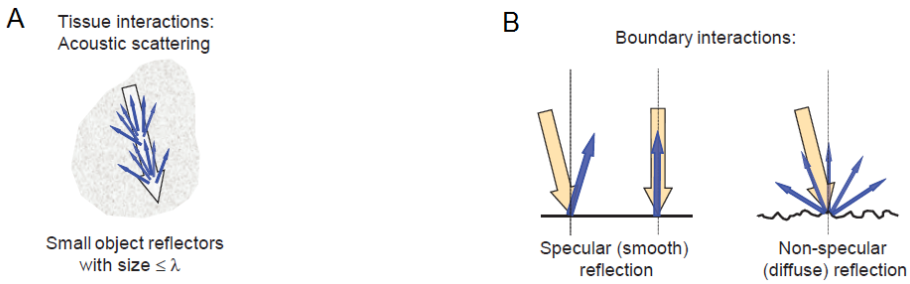

Figure 2-2: A: The ultrasound beam is scattered by small objects in the tissue that are of similar dimension as the wavelength. **B:** Specular reflectors reflect the incident beam in only one direction. Nonspecular reflectors reflect the beam in all directions. The echo intensity of nonspecular reflectors is (approximately) independent of the incedent angle. Figure adapted from [9].

dependent attenuation coefficient (μ_f) expressed in dB/(MHz·cm) and the distance from the transducer (d) expressed in cm [9]:

$$10 \cdot \log\left(\frac{I}{I_0}\right) = -\mu_f \cdot f \cdot d \tag{2-5}$$

The attenuation coefficient, μ, expressed in units of dB/cm, is the relative intensity loss per centimeter of travel for a given medium and frequency. The product of the ultrasound frequency (in MHz) with the frequency dependent attenuation coefficient μ_f, (dB/cm)/MHz gives the approximate attenuation coefficient in dB/cm. Increasing frequency increases the attenuation coefficient, which increases ultrasound attenuation.

2-2 Ultrasound Transducers

The ultrasound signal is generated with an ultrasound transducer. The ultrasound transducer consists of an array of piezoelectric elements. Each piezoelectric element in the transducer serves both as an emitter and receiver. A potential difference over the element induces rapid expansion and contraction of the piezoelectric element. Contraction and expansion of the element emits an ultrasound wave. In the receiving mode, the pressure amplitude of the returning echo causes mechanical compression of the piezoelectric element, which induces an electric signal. The combined electric signal of all the piezoelectric elements in the transducer array is used the reconstruct the ultrasound image.

2-2-1 Piezoelectric Elements

The piezoelectric elements in the transducer operate in a resonance mode. A short voltage spike (usually 150 V, 1 μs) is applied to the element, which causes the material initially to contract and then subsequently vibrate at a natural resonance frequency. The wavelength (λ) of the emitted ultrasound signal equals two times the material thickness of the piezoelectric element. This means that higher ultrasound frequencies are achieved with thinner elements, and lower frequencies with thicker elements.

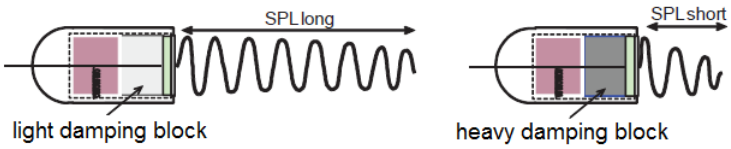

Figure 2-3: The damping block on the back of the piezoelectric elements determines the SPL. Heavy damping reduces the number of waves n in the emitted pulse, which reduces the SPL. Figure adapted from [9].

On the back of the piezoelectric element is a block of absorbing material. This so called 'damping block' damps the resonance vibration of the piezoelectric element, to reduce the Spatial Pulse Length (SPL). SPL is the spatial length of the pulse that is emitted when the element is activated with the voltage peak. The SPL is determined by wavelength (λ) and the number of waves (n):

$$\text{SPL} = \lambda \cdot n \tag{2-6}$$

SPL influences spatial resolution. A short SPL has a positive impact on spatial resolution. The damping block on the back of the elements reduces the number of waves in the pulse, n, which reduces the SPL. The relation between spatial resolution and SPL is furhter elaborated in section 2-3.

2-2-2 Phased Array Transducers

Most modern ultrasound equipment acquires ultrasound images with so called "phased array transducers". All piezoelectric elements in a phased array transducer are involved in formation of the ultrasound beam. The elements are activated nearly simultaneously with a voltage peak to generate a single ultrasound beam. Small time delays between the activation of the individual elements in the array are used to steer and focus the beam electronically, using constructive and destructive wave summations. In the receiving mode, all elements of a phased array are involved in the reconstruction of the returning echo from the emitted pulse.

2-3 Ultrasound Beam Properties

The interaction of all elements in a phased array transducer induces a longitudinal wave that travels from the transducer surface into the propagation medium, where it is reflected by structures within the medium. The ultrasound beam exhibits two distinct beam patterns. Close to the transducer surface, the beam converges to a certain point at a distance determined by transducer geometry and frequency. Beyond that point, the beam diverges.

2-3-1 Transmit Focus

The point where the beam converges is called the "focal point" of the ultrasound beam. The distance of the focal point can be manipulated by changing the time delays between the

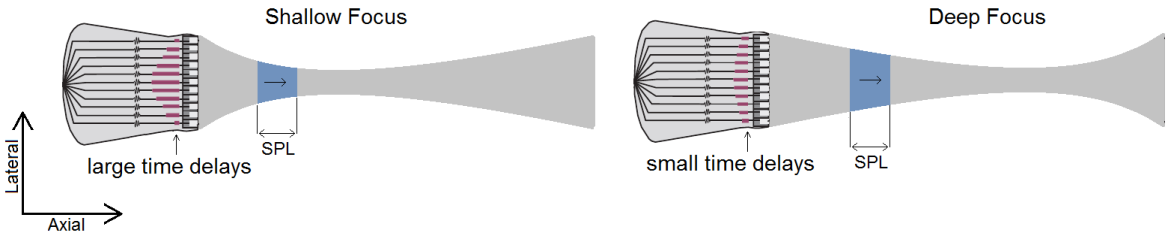

Figure 2-4: Simultaneous interaction of the piezoelectric elements induces an ultrasound pulse that travels through the tissue. The length of the pulse (SPL) is determined by damping of the elements. The point where the beam converges is determined by small time delays between the activation of the individual elements. Focal depth is increased by decreasing the time delays. Figure adapted from [9].

activation of the individual elements in the transducer array. A shallow focal zone is created by activating the outer elements before the inner elements of the transducer array. The focal distance is increased by reducing the time delay difference over the elements in the array (see figure 2-4).

2-3-2 Spatial Resolution

The visibility of detail in the ultrasound images, "spatial resolution", depends on the dimensions of the emitted ultrasound pulse. A short and narrow pulse creates less overlapping echos, which allows to visualize small details in the tissue. The width of the pulse is determined by focussing the ultrasound beam. The length of the pulse (SPL) is determined by damping of the elements and frequency of the signal (figure 2-4). The length and width of the ultrasound signal determine the "axial resolution" and "lateral resolution" of the ultrasound probe.

Axial Resolution

Axial resolution (Δ_A) is the closest distance of two objects along the axis of the ultrasound beam that can be resolved as separate [9]. The axial resolution depends on the SPL of the emitted ultrasound pulse. Resolvablity of two distinct objects along the axis of the emitted pulse requires the echos to be distinct without overlap. Objects spaced further than 1/2 SPL are resolved as two separate objects (figure 2-5A,B). Objects spaced closer than 1/2 SPL cannot be resolved, since their echos are overlapping (figure 2-5C). Equation 2-7 shows the relation between axial resolution and SPL:

$$\Delta_A = \frac{1}{2} \cdot \text{SPL} = \frac{n \cdot \lambda}{2} = \frac{n \cdot c}{2 \cdot f} \tag{2-7}$$

Equation 2-7 shows that axial resolution is improved by increasing the frequency of the ultrasound signal (f), or by increasing the damping of resonance, which reduces the number (n) of waves in the pulse (figure 2-5D). The axial resolution depends only on transducer frequency, and is independent of ultrasound beam geometry. Consequently, axial resolution does not change with distance from the transducer.

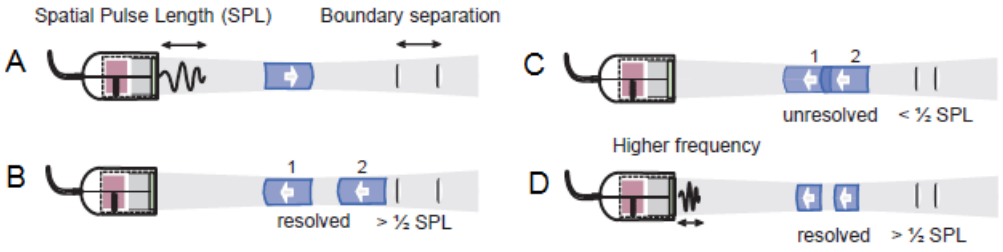

Figure 2-5: A: The axial resolution depends on the Spatial Pulse Length (SPL) of the ultrasound pulse that is emitted by the transducer. **B:** Objects spaced further than 1/2 SPL are resolved in the ultrasound image. **C:** Objects spaced closer than 1/2 SPL cannot be resolved as two separate objects in the image. **D:** Increasing the frequency decreases the SPL, which allows to resolve closely spaced objects (increased axial resolution). Figure adapted from [9].

Lateral Resolution

Lateral resolution refers to the ability to discern two closely separated objects perpendicular to the axis of the ultrasound beam. Lateral resolution depends on the lateral width of the ultrasound beam, which depends on distance from the transducer. The best lateral resolution is at the narrowest point in the ultrasound beam. When two points are spaced further than the lateral beam widht, these points can be resolved as two separate points in the ultrasound image (figure 2-6A,B). Objects spaced closer than the lateral beam dimension cannot be resolved as two distinct objects, unless the lateral beam width is reduced by focussing 2-6C,D). So, contrary to the axial resolution, the lateral resolution is depth-dependent, and depends on beam geometry [34, 9].

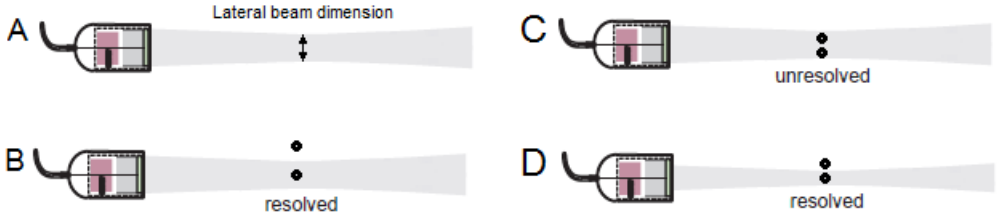

Figure 2-6: A: The lateral resolution depends on the lateral dimension of the ultrasound beam. **B:** Objects spaced further than the lateral beam dimension are resolved in the ultrasound image. **C:** Objects spaced closer than the lateral beam dimension cannot be resolved as two separate objects in the image. **D:** Reducing the lateral beam width by focussing allows to resolve closely spaced objects (increased lateral resolution). Figure adapted from [9].

2-4 Ultrasound Image Acquisition

This section explains how a 2D ultrasound image is reconstructed from the sequence of returning echos. Each single pulse of the ultrasound transducer results in single line of echo information. Emitting multiple pulses under a small incrementing angle (δ_θ) allows to reconstruct a 2D ultrasound image from the multiple lines of echo information.

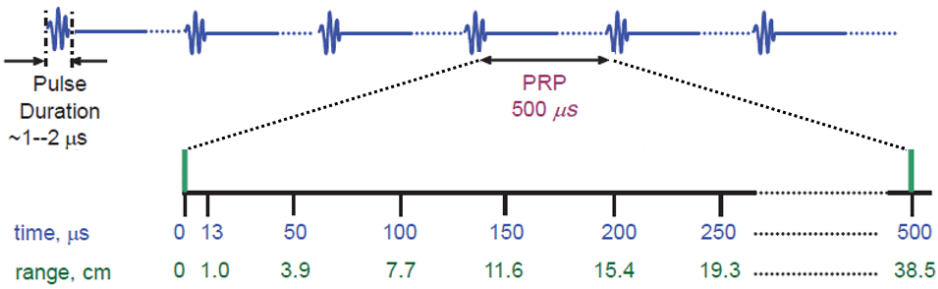

Figure 2-7: After a short ultrasound pulse is emitted (1-2 μs), a period of approximately 500 μs is occupied with receiving the echos of the emitted pulse. The timepoint of the returning echo is directly related to its depth. The time between two pulses is called the Pulse Repetition Period. Figure adapted from [9].

2-4-1 Pulse-Echo Operation

The transducer array of an ultrasound probe serves both as emitter of ultrasound pulses, and receiver of the returning echos. After the pulse is emitted, the system switches to the receiving mode to detect echos. The majority of the time is occupied by listening to the returning echos. The time interval (T) between excitation of the transducer, and the received echo is directly related to the depth (D) of the object that causes the echo:

$$T = \frac{2 \cdot D}{c} \tag{2-8}$$

where c, the speed of sound, is expressed in cm/μs (0.154 cm/μs in soft tissue); distance from the transducer to the reflector, D, is expressed in cm; the constant 2 represents the round-trip distance; and time is expressed in μs (figure 2-7) [9].

The time interval between two emitted ultrasound pulses is called the Pulse Repetition Period (PRP). The PRP is determined by the time required of the most distinct echos to return to the transducer. When echos from the previous pulse return after the second pulse is already emitted, these echos are confused with prompt echos of the second pulse in stead of distinct echos from the previous pulse, and artifacts occur. Therefore, the PRP cannot be shorter as the time required for the most distinct echo to return to the transducer. The inverse of PRP is Pulse Repetition Frequency (PRF). For imaging purposes, typical a PRF of 2 kHz to 4 kHz is required.

2-4-2 2D Image Reconstruction

The sequence of echos returning from one emitted pulse results in a digital signal, proportional to the amplitude of the returning echos. This amplitude-modulated signal as function of time is the so called 'A-line' of image data.

This amplitude modulated signal is converted to a brightness-modulated signal, by conversion of the amplitude of the signal to brightness-modulated dots along the A-line trajectory. The location of the dot on the line is determined by the timepoint of the signal in the A-line

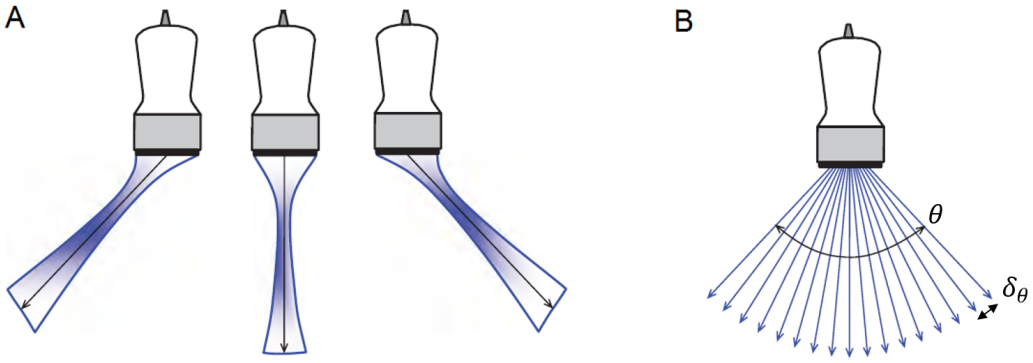

Figure 2-8: A: The phased array transducer electronically adjust the angle under which the ultrasound beam is emitted. **B:** One single frame is acquired by emitting ultrasound beams under an incrementing angle δ_θ until the full angle θ of the Field of View (FOV) is covered. Figure adapted from [9].

according to equation 2-8, and the brightness of the dot is determined by the amplitude of the signal at that point. The brightness modulated signal is called a 'B-line' of image data.

One single frame in a sequence of 2D-ultrasound images is reconstructed from a number of B-lines. The phased-array transducer 'scans' the image within the FOV by emitting each ultrasound pulse under a small incrementing angle (δ_θ) until the total angle θ of the FOV is covered. Decreasing δ_θ increases the number (N) of B-lines that is used to build the image, which results in a higher image quality. However, since more B-lines are used, more pulses are required to generate one image, which increases the time required to generate one ultrasound frame (T_{frame}). The time required to produce one frame is the product of the number of B-lines (N) and the time required to generate one B-line (T_{line}). T_{line} is determined by the imaging depth (D), according to equation 2-8. The relation between frame rate, number of lines per frame, and imaging depth is as follows:

$$\text{Frame Rate} = \frac{1}{T_{frame}} = \frac{1}{N \cdot T_{line}} = \frac{1}{N \cdot \left(\frac{2 \cdot D}{c}\right)} \tag{2-9}$$

Chapter 3

Development of an Objective Image Quality Assessment Method

In the introduction of this thesis it was stated that real-time imaging of the left atrium could improve efficacy and outcome of Atrial Fibrillation (AF) ablation procedures. Currently used Transesophageal Echocardiography (TEE) equipment is not suitable for real-time imaging during ablation, due to the limited Field of View (FOV). Anatomical landmarks such as the ostia of the Pulmonary Veins (PV), and the posterior Left Atrium (LA) wall are of importance to visualize during AF ablation procedures, but are (partly) outside the FOV.

Furthermore, it was shown that a miniaturized, trans-balloon TEE imaging probe possibly solves the aforementioned limitations of the FOV, which makes miniaturized trans-balloon TEE a candidate for real-time imaging of the left atrium during atrial ablation procedures.

However, before miniaturized, trans-balloon TEE can be applied in clinical practice, it is required to validate that the image quality of the miniaturized probe is sufficient for the intended application. Therefore, the image quality of the miniaturized probe has to be compared to the image quality of the currently used TEE probe.

To compare image quality of ultrasound probes, a method to objectively measure the image quality has to be developed. This chapter presents the objective Image Quality Assessment (IQA) method that was used in this thesis. Standardized ultrasound phantoms and IQA software were used, and measurement methods are in accordance with the standards specified in IEC 62736 and IEC 61391 [35, 36]. The developed IQA method is applied to compare the image quality of the miniaturized, trans-balloon TEE probe with the currently used TEE probes.

This chapter discusses the ultrasound phantoms and software that were used. Furthermore, the image quality parameters are discussed and quantification of these parameters is explained.

3-1 Ultrasound Image Quality Assessment Phantoms

Objective assessment of ultrasound image quality requires the use of standardized ultrasound IQA phantoms. These phantoms are made of a base material with similar speed of sound, attenuation and scattering characteristics as parenchymal soft tissue [37, 38, 34]. The base material contains several "targets" of specific size and contrast with respect to the background. Scanning the phantom and analysis of the ultrasound images allows to quantify certain image quality parameters [37, 39].

In this thesis, image quality measurements were carried out using the UltraiQ uniformity phantom (figure 3-1A), and the UltraiQ general purpose ultrasound phantom (figure 3-1B) from CablonMedical, Leusden, the Netherlands.

The UltraiQ uniformity phantom (figure 3-1A) consists of a uniform block of silicone gel, that contains no targets. This phantom is used to generate uniform ultrasound images for measurement of the signal to noise ratio.

The base material of the UltraiQ general purpose ultrasound phantom (figure 3-1B) contains a vertical line of monofilament nylon wires, the so called "pins", and a group of 6 echogenic, cylindrical grey targets. Target dB level is defined as the echo intensity of the targets (I_T) with respect to the echo intensity of the background (I_{BG}). The relative echo intensity of targets and background is expressed in decibel (dB):

$$\text{target dB level} = 10 \cdot \log\left(\frac{I_T}{I_{BG}}\right) \tag{3-1}$$

The echogenic grey targets have a relative echo intensity with respect to the background of -9dB, -6dB, -3dB, 3dB, 6dB and 15dB respectively (figure 3-1C). Ultrasound images of the general purpose phantom are used to measure the contrast resolution, contrast to noise ratio and spatial resolution of the ultrasound probe. Image quality parameter quantification is explained in section 3-3.

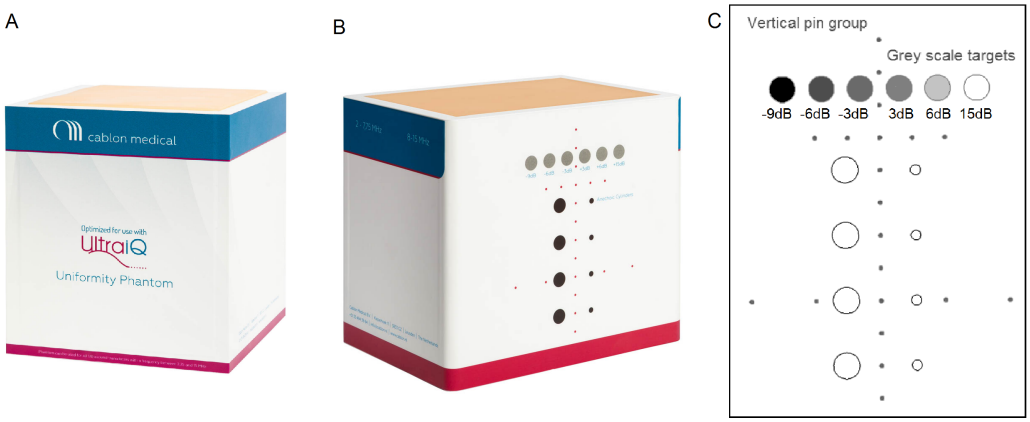

Figure 3-1: **A:** The ultraIQ uniformity phantom (Cablon Medical, Leusden, Netherlands) [40]. **B**:The UltraiQ general purpose phantom (Cablon Medical, Leusden, Netherlands) [40]. **C** Target pattern in the general purpose phantom.

3-2 Image Quality Assessment Software

The ultrasound images of the IQA phantoms were analyzed using IQA software for quantification of the image quality. In this thesis, the "UltraiQ" software tool (CablonMedical, Leusden, the Netherlands) was used. Several studies have shown that the results are accurate and repeatable, and that the software provides objective, quantitative assessment of image quality [41, 39].

The UltraiQ software tool is able to quantify image quality parameters using pixel grey value analysis of the ultrasound images obtained from scanning the ultrasound phantoms. These ultrasound phantom images were imported in the software tool, and the relevant targets for measurement were selected by placing a Region of Interest (ROI) over the targets. Image quality parameters such as contrast resolution, spatial resolution and penetration depth are quantified based on pixel grey value analysis within the ROI. The quantification process is explained in detail in the following sections of this chapter.

The results obtained with the UltraiQ software tool were exported to Excel. The data from the Excel files was analyzed using several MATLAB function files.

3-3 Image Quality Parameters

In this thesis, ultrasound image quality and probe characteristics were measured by quantification of the following image quality parameters: The *contrast resolution*, which is the smallest detectable difference in echo intensity. The *Contrast-to-Noise Ratio (CNR)*, which is the ratio between contrast and noise in the ultrasound image. The *spatial resolution*, which is the smallest distance between two points in the ultrasound image that can be resolved as separate. And finally, the *penetration depth* of the ultrasound signal, which is defined as the depth in the ultrasound image where the Signal-to-Noise Ratio (SNR) drops below one. This section discusses each image quality parameter, and describes the parameter quantification process using the UltraIQ software.

3-3-1 Contrast Resolution

The contrast resolution is defined as the smallest difference in echo intensity of an object (I_{OBJ}) with respect to the echo intensity of the background (I_{BG}) that can be detected in the ultrasound image [38, 34].

The ability to distinguish an object as separate from the background, depends on the mapping of differences in echo intensity to grey values. When a small difference in echo intensity results in a large difference in grey value at the screen, even objects with low contrast w.r.t. the background (low I_{OBJ}/I_{BG}) can be detected in the ultrasound image. The grey step per dB echo level is called the "gamma" of the ultrasound probe [39, 34]. Probes with a high gamma have a better contrast resolution as probes with a low gamma.

Quantification
The gamma of ultrasound probes can be quantified by scanning objects with known echo intensity w.r.t. the background [39, 42]. For this purpose, the group of grey targets in

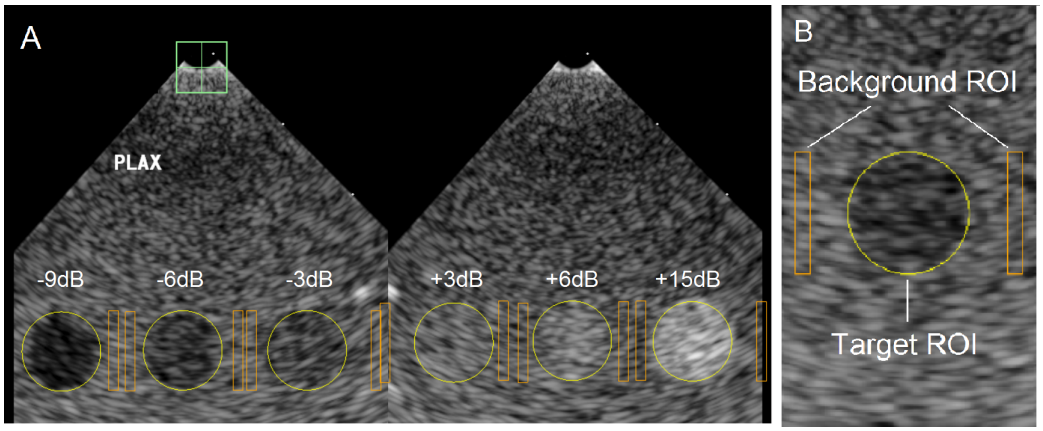

Figure 3-2: **A**:Ultrasound image of the grey targets in the Cablon ultrasound phantom. The targets in the image have a known echo dB level with respect to the background. **B** Close up of one of the targets in the image. The target grey value (GV_T) and background grey value (GV_{BG}) are determined by averaging the pixel grey values within the target Region of Interest (ROI) and background ROI respectively.

the UltraiQ general purpose phantom is scanned (see figure 3-2A). The UltraiQ software calculates the grey value of each target (GV_T) by averaging grey values of the pixels within the circular ROI (figure 3-2B). The gamma is determined by plotting the grey value of the targets against the dB level of the targets. Plotting a linear fit through the datapoints yields a straight increasing line. The steepness of this line is the average increase in grey value per echo dB level, which is the gamma.

3-3-2 Contrast to Noise Ratio

Visibility of objects with respect to the background is not only determined by the contrast difference between background and object, but also by the noise in the image. The ratio between contrast and noise, CNR, is a measure for the visibility of structures relative to the noise level in the image.

The contrast between background and target is the absolute difference between the mean grey value of the target (GV_T) and the mean grey value of the background (GV_{BG}). The noise is the variance in pixel grey values within the target (σ_T^2) and background (σ_{BG}^2). The ratio between the contrast and the noise yields the CNR [34, 38]:

$$\text{CNR} = \frac{|GV_T - GV_{BG}|}{\sqrt{\sigma_T^2 + \sigma_{BG}^2}} \tag{3-2}$$

Quantification
The UltraiQ software tool was used to calculate the CNR for each grey target in the ultrasound image (figure 3-2). The software calculates GV_T and GV_{BG} as the average grey value of the target and background ROI respectively (figure 3-2B). The variance of grey values, σ_T^2 and σ_{BG}^2, is determined by calculation of the variance of pixel grey values within the target ROI and background ROI. CNR is calculated according to equation 3-2.

3-3-3 Spatial Resolution

Spatial resolution refers to the ability to discern two closely spaced objects in the ultrasound image as separate. Objects spaced closer than the spatial resolution cannot be resolved as two distinct points in the image. In chapter 2, section 2-3, it was explained that spatial resolution depends on the spatial dimensions of the emitted ultrasound pulse.

Since it is impossible to measure the spatial dimensions of the ultrasound pulse directly, the spatial resolution is indirectly measured by measuring the dimensions of the so called "Point Spread Function (PSF)". The PSF determines how an infinitely small point is represented in the ultrasound image. Convolution of the object with the PSF yields the image. A narrow PSF will spread out the points over a smaller area as a wide PSF, which will result in a high spatial resolution (figure 3-3B,C). So, a *high* spatial resolution corresponds to a *narrow* PSF, and vice versa, a *low* spatial resolution corresponds to a *wide* PSF [9].

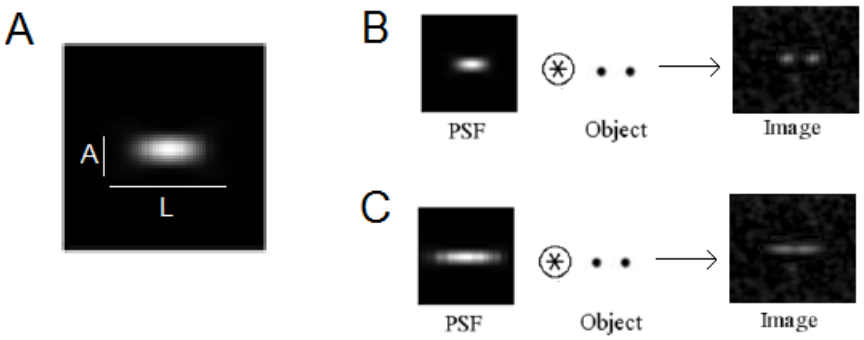

Figure 3-3: A: Typical Point Spread Function (PSF) of an ultrasound probe. The PSF is wider in lateral direction (L) as in axial direction (A). Convolution of the Point Spread Function (PSF) with the objects yields the image. **B:** A narrow PSF yields an image with two resolvable points (high spatial resolution). **C:** A wide PSF yields an image where the two points cannot be resolved (low spatial resolution).

The PSF of the ultrasound probe is asymmetrical: the PSF is wider in lateral direction as in axial direction (figure 3-3A). Therefore, the spatial resolution of the ultrasound probe is measured in 'axial resolution' and 'lateral resolution' [39, 42, 34, 9]. Axial direction refers to the direction along the axis of the ultrasound beam. Lateral direction is perpendicular to the axial direction.

Quantification

To quantify the spatial resolution of the ultrasound probes, the vertical pin group of the UltraiQ general purpose phantom was scanned. The line of pins in the phantom appears as line of bright spots in the ultrasound image (figure 3-4A). The axial and lateral dimension (Δ_A, Δ_L) of each pin, are a measure for the lateral and axial resolution: a small, sharp pin in the image indicates good spatial resolution, and a wide, faded pin indicates poor spatial resolution (figure 3-4B). Measuring the lateral and axial dimension of each pin along the line allows to calculate the lateral and axial resolution of the ultrasound probe as function of distance from the transducer [39].

The lateral and axial dimension of the pins were calculated by the UltraiQ image quality assessment software. The software automatically detects the pin in the selected ROI, and

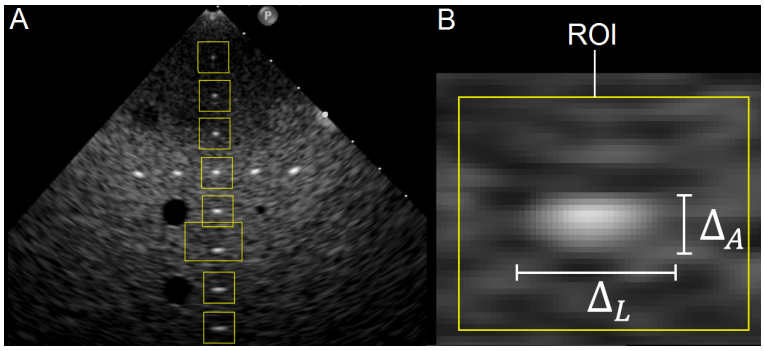

Figure 3-4: **A**: The vertical line of pins in the ultrasound phantom is displayed as a line of bright spots in the ultrasound image. Axial direction is along the line of pins, lateral direction is perpendicular to the axial direction, in the plane of the image. **B**: Close-up of one of the pins in the image. The axial dimension (Δ_A) and lateral dimension (Δ_L) of the pin are shown.

determines the central axes of the pin. The lateral and axial pin dimensions are determined by grey value analysis along the horizontal and vertical central axis of the pin respectively. Figure 3-5 shows an example of the grey value analysis along the lateral axis of one of the pins in the ultrasound image.

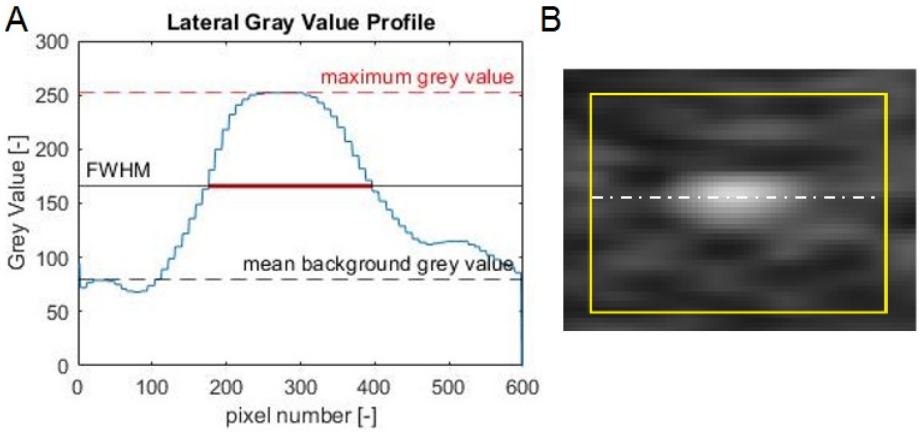

Figure 3-5: **A**:Grey value profile along the lateral axis of one of the pins in the ultrasound image **B**: Close up of the pin, with the lateral axis indicated with the dashed line.

The pixel grey value analysis along the central line of the pin results in a graph representing the grey value of each pixel along that axis (figure 3-5A). The width of the pin is defined as the width of the grey value curve at the point where the curve intersects a certain threshold. In this thesis, the "Full-Width, Half-Maximum (FHWM)" threshold was used. The FWHM threshold is standardized by IEC 61391-1 as the threshold for spatial resolution measurement of ultrasound equipment [36].

The maximum grey value along the axis (GV_{max}) and the mean grey value of the background pixels within the ROI (GV_{BG}) are determined. The nominal peak value is the difference between the maximum grey value and the mean background grey value ($GV_{max} - GV_{BG}$). The 'FWHM-width' is the width of the graph at grey level one half of the nominal peak value above the mean background grey value:

$$GV_{FWHM} = GV_{BG} + \frac{GV_{max} - GV_{BG}}{2} \tag{3-3}$$

In the example in figure 3-5, the maximum grey value is 252 ($GV_{max} = 252$) and the mean background grey value is 80 ($GV_{BG} = 80$). According to equation 3-3, the FWHM-grey value is 166. The width of the graph, measured at grey value 166 is 221 pixels; i.e.: the lateral pin size, measured with the FWHM threshold is 221 pixels.

The software calculates the lateral axial dimension of each pin along the line according to the method described above. This yields the lateral and axial resolution of the ultrasound probe, as function of distance from the transducer.

3-3-4 Penetration Depth

The penetration depth of the ultrasound signal is defined as the depth in the ultrasound image where the SNR drops below one [35, 43, 41]. In chapter 2, section 2-1-3, it was explained that the intensity of the returning ultrasound echos reduces with increasing depth. This means that the amplitude of the "signal" reduces with depth. On the other hand, the noise originating from signal amplification and electronic components is independent of the depth in the image. This means that the SNR reduces over depth: close to the transducer SNR is high, and far from the transducer the SNR is low [39, 42, 9].

The SNR is defined as the ratio between the the power of the signal (P_S) and the power of the noise (P_N). Since the signal power scales with the amplitude squared, the SNR can be expressed as the ratio between the amplitude of the signal (A_S) and the amplitude of the noise (A_N):

$$\text{SNR} = \frac{P_S}{P_N} = \frac{A_S^2}{A_N^2} \tag{3-4}$$

Quantification
In this thesis, penetration depth of the ultrasound signal was determined according the method described in IEC 62736 [35]. This method uses the combined information of two ultrasound images to determine the penetration depth. The penetration depth was determined using an ultrasound image of the UltraiQ uniformity phantom and an ultrasound image holding the probe in air. The ultrasound image holding the probe in air shows the noise originating from transducer elements and electronic amplification. This is the background noise in the ultrasound image. The ultrasound image of the uniform phantom shows the echo signal of the phantom, combined with the background noise. Figure 3-6 shows an example of these ultrasound images.

The UltraiQ software calculates the grey value profile along the central axis of both ultrasound images by laterally averaging the grey values in the rectangular ROI (figure 3-6). The grey value profile of the air-scan image shows the grey values of the noise as a function of depth (d) in the image: $GV_N(d)$. The grey value profile of the uniform phantom image shows the grey values of the noise added to the echo signal as a function of depth $GV_{S+N}(d)$.

Assuming uncorrelated noise, the power of the pure ultrasound signal (without noise) is computed by subtracting the power of the noise from the power of the noisy signal:

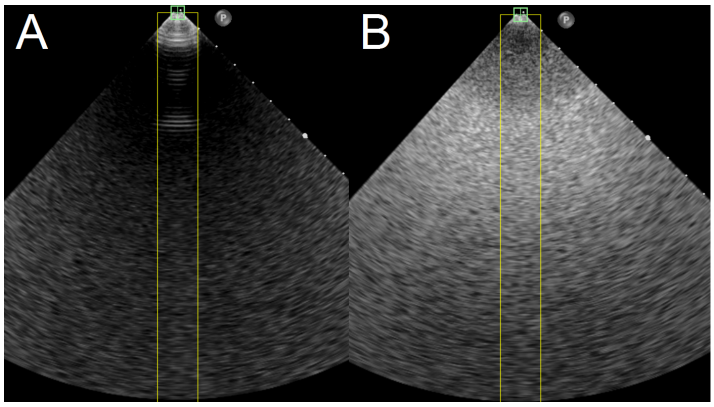

Figure 3-6: **A**: Ultrasound image of the probe in air. This shows the background noise originating from transducer elements and electronic amplification. **B**: Ultrasound image of the uniform phantom. This shows the pure ultrasound signal added to the background noise.

$$P_S = P_{S+N} - P_N \tag{3-5}$$

Using equation 3-5, the SNR in equation 3-4 is rewritten as:

$$\text{SNR} = \frac{P_S}{P_N} = \frac{P_{S+N} - P_N}{P_N} = \frac{P_{S+N}}{P_N} - 1 \tag{3-6}$$

Since signal power scales with amplitude squared, and since the amplitude of the signal is directly correlated to the grey values in the ultrasound image, the SNR in equation 3-6 can be rewritten as:

$$\text{SNR}(d) = \frac{P_{S+N}}{P_N} - 1 = \frac{A_{S+N}^2}{A_N^2} - 1 = \frac{GV_{S+N}(d)^2}{GV_N(d)^2} - 1 \tag{3-7}$$

The penetration depth is the depth where the signal-to-noise ratio is less than one. With SNR equal to one, equation 3-7 is rewritten as:

$$\frac{GV_{S+N}^2(d)}{GV_N^2(d)} = 2 \rightarrow \frac{GV_{S+N}(d)}{GV_N(d)} = \sqrt{2} \tag{3-8}$$

Using equation 3-8, the penetration depth (PD) is calculated as the depth where the grey value profile of the uniform phantom minus the grey value profile of the air image multiplied with the square root of 2 intersects zero. written as equation this yields:

$$\text{PD} := GV_{S+N}(d) - \sqrt{2} \cdot GV_N(d) = 0 \tag{3-9}$$

Chapter 4

Method

This chapter presents the structure of the research that was conducted in this master thesis. The goal of this thesis was to investigate whether image quality of miniaturized trans-balloon Transesophageal Echocardiography (TEE) is sufficient for intraprocedural imaging of Atrial Fibrillation (AF) ablation procedures. The main research question was divided in the following two sub-questions:

- Sub-question 1: What is image quality of the miniaturized ultrasound probe compared to the image quality of the currently used standard TEE probes?
- Sub-question 2: How does a transducer balloon influence the image quality of the miniaturized ultrasound probe?

To answer these sub-questions, two separate studies were performed. In each study, the Image Quality Assessment (IQA) method as described in chapter 3 was applied to measure image quality. This chapter provides a summary of the applied research method. Detailed information is in the measurement report of the two studies (attached in appendix A and B).

4-1 IQ Comparison: Miniaturized TEE vs. Normal TEE

In the first study of this thesis, image quality of a miniaturized ultrasound probe was compared to the image quality of the currently used standard TEE probes. The miniaturized ultrasound probe that was used in this study was the Philips Intra-Cardiac Echocardiography (ICE) ultrasound probe. This is a small, high frequency ultrasound probe with a diameter of approximately 3mm. The image quality of this miniaturized probe was compared to the Philips X8-2t and Philips S7-3t TEE ultrasound probes. The Philips X8-2t is the current state of the art probe used for TEE imaging. This probe has a lower frequency as the ICE ultrasound probe, and a transducer diameter of approximately 18 mm. The S7-3t is a probe used for peadiatric TEE imaging with transducer diameter of approximately 12 mm. The frequency of the S7-3t probe is higher than the X8-2t, but lower than the ICE. Figure 4-1 shows the transducers of the three probes.

4-1-1 Workflow

The workflow in this paragraph describes the procedure that was followed to measure image quality of the probes. This workflow was followed three times: First to measure image quality of the X8-2t TEE probe, next to measure the image quality of the S7-3t TEE probe, and finally to measure image quality of the ICE ultrasound probe.

First, the UltraiQ general purpose phantom and the UltraiQ uniformity phantoms were scanned with the ultrasound probe. The scans were repeated 6 times, which reduced the influence of stochastic effects. The ultrasound images were stored on the ultrasound system, and copied to USB. The next step was to import and analyze these images in the UltraiQ software tool. The contrast resolution, contrast to noise ratio, spatial resolution and penetration depth were determined according to the method described in chapter 3. Finally, the data was imported in MATLAB to visualize the measurement results in graphs.

Above described workflow was followed for the X8-2t, S7-3t and ICE miniaturized ultrasound probe, which allowed to objectively compare the image quality of these probes to each other. The workflow is schematically presented in figure 4-3.

4-2 IQ Comparison: Trans-Balloon vs. Direct US Imaging

In the second study of this thesis, the influence of a water-filled balloon on image quality was studied. To measure this, the Philips ICE ultrasound probe was inserted in a water-filled balloon and image quality of the trans-balloon ultrasound images was compared to the ultrasound images of the ICE probe without balloon around the transducer. Figure 4-2 shows the transducer of the ICE ultrasound probe and the sheath with balloon where the ICE probe was inserted in. Details of the setup are provided in appendix C.

4-2-1 Workflow

The workflow in this paragraph describes the procedure that was followed to measure the influence of the water-filled balloon on image quality. This workflow was followed two times: First to measure image quality of the ICE ultrasound probe without interference of the balloon. Next, the ICE probe was inserted in the water-filled balloon as described in appendix C, and the same workflow was followed again to measure image quality of the trans-balloon ultrasound images. Comparing the results of the image quality measurements with and without balloon allows to evaluate the influence of the balloon on image quality.

First, the UltraiQ general purpose phantom and the UltraiQ uniformity phantoms were scanned with the ultrasound probe. The scans were repeated 20 times, which reduced the influence of stochastic effects. The ultrasound images were stored on the ultrasound system, and copied to USB. The next step was to import and analyze these images in the UltraiQ software tool. The contrast resolution, contrast to noise ratio, spatial resolution and penetration depth were determined according to the method described in chapter 3. Finally, the data was imported in MATLAB to visualize the measurement results in graphs.

These steps were first applied to the ICE ultrasound probe, and then applied to the ICE ultrasound probe inserted in the water-filled balloon. This method allows to objectively

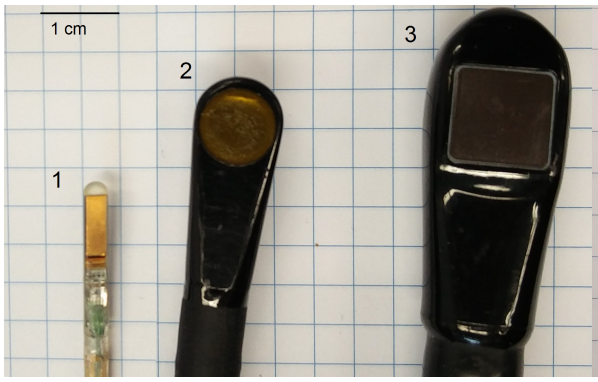

Figure 4-1: Transducer of the Intra-Cardiac Echocardiography (ICE) ultrasound probe (1) compared to the transducer of the S7-3t (2) and X8-2t TEE ultrasound probe (3). Image quality of the ICE ultrasound probe was compared to image quality of the X8-2t and S7-3t TEE probe.

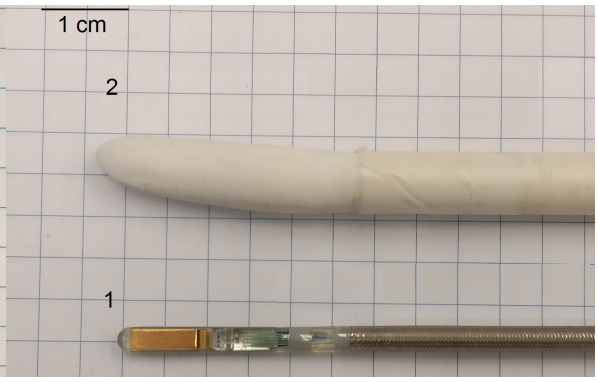

Figure 4-2: The Intra-Cardiac Echocardiography (ICE) ultrasound probe (1), and the sheath with balloon (2). Image quality of the ICE ultrasound probe was compared to image quality of the ICE inserted in the sheath to study the influence of the balloon on image quality.

compare trans-balloon to direct ultrasound image quality of the miniaturized ultrasound probe. The workflow is schematically presented in figure 4-3.

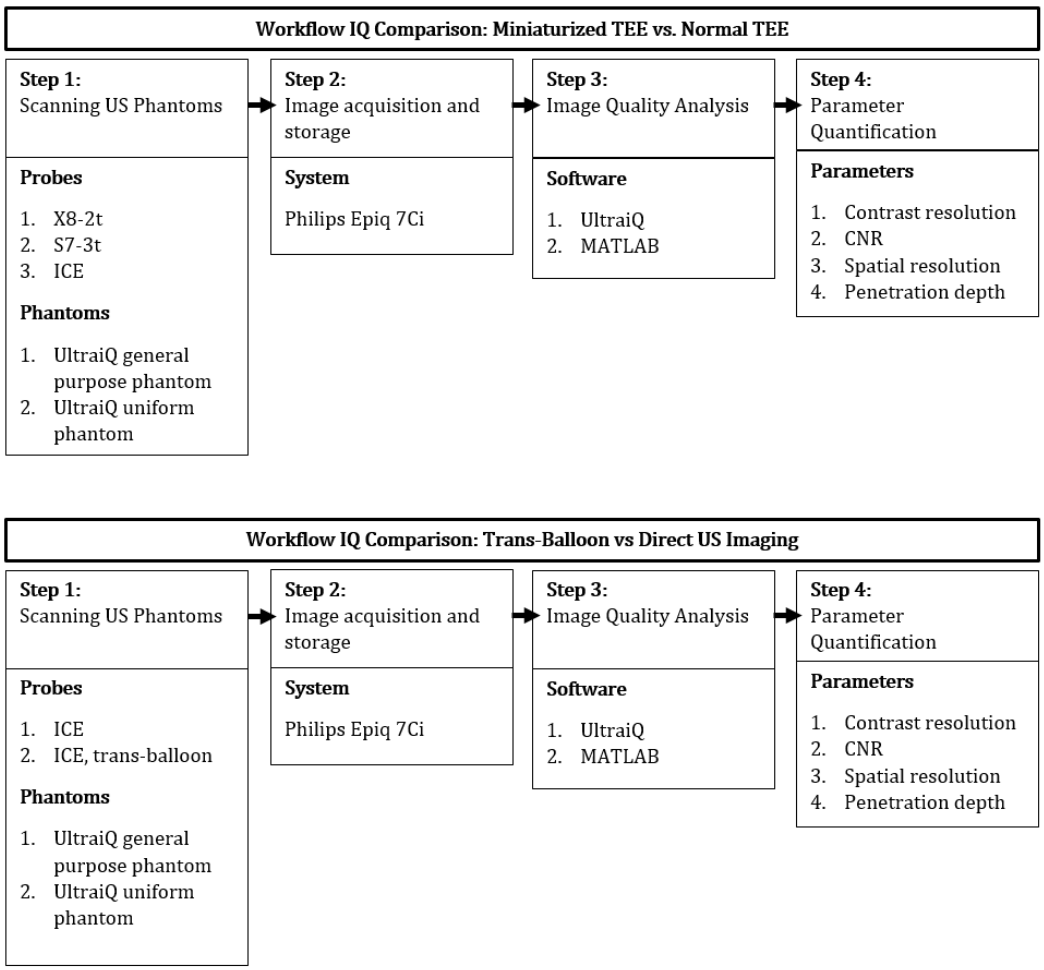

Figure 4-3: Workflow of the two studies that were performed to answer the two sub-questions of this thesis.

Chapter 5

Results

This chapter presents the results of the image quality measurements. The chapter is split up in two sections, corresponding to the two sub questions in which the main research question was divided. Mean value and standard deviation of the measurements were calculated, and the results were graphically presented using MATLAB. The graphical representation makes it easier to observe differences and interpret the results.

5-1 IQ Comparison: Miniaturized TEE vs. Normal TEE

This section presents the results of the first study of this master thesis. In this study, the image quality of a miniaturized ultrasound probe (Intra-Cardiac Echocardiography (ICE) ultrasound probe) was compared to the image quality of the currently used Transesophageal Echocardiography (TEE) probes (X8-2t probe, S7-3t probe). Image quality was assessed based on measurement of the contrast resolution, Contrast-to-Noise Ratio (CNR), spatial resolution and penetration depth. Measurements were repeated 6 times, and results are reported with mean and standard deviation ($\mu \pm \sigma$).

5-1-1 Contrast Resolution

Figure 5-1A shows the measured grey value of each target plotted against the target dB value. Figure 5-1B shows a linear regression line through the datapoints in figure 5-1A. The errorband indicates the 95% confidence interval of the linear fit. The regression coefficient of the line is defined as the "gamma" (γ), which is a measure for the contrast resolution.

Multiple regression analysis was used to test if the regression coefficient for the ICE probe and the X8-2t probe, and the regression coefficient for the ICE probe and S7-3t probe were significantly different. The gamma of the ICE probe ($\gamma_{\text{ICE}} = 5.0$) and the X8-2t probe ($\gamma_{\text{X8-2t}} = 5.0$) were not significantly different, t(1) = -0.00, p = 0.997. The gamma of the ICE probe ($\gamma_{\text{ICE}} = 5.0$) and the S7-3t probe ($\gamma_{\text{S7-3t}} = 4.2$) were not significantly different, t(1) = -1.11, p = 0.298.

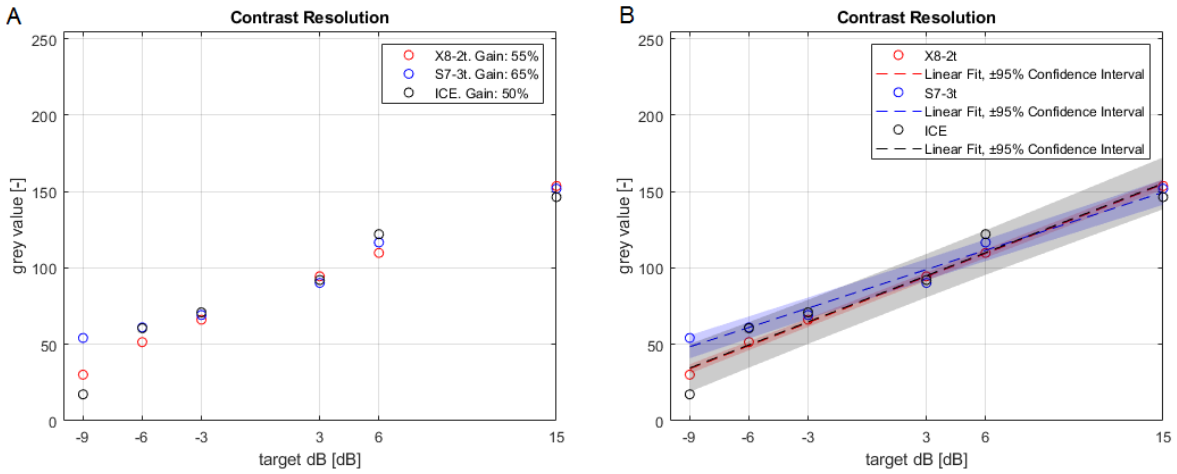

Figure 5-1: A: Mean grey value of each target plotted against target echo level (dB). **B:** Linear fit through datapoints, the errorband indicates the 95% confidence interval of the linear fit.

5-1-2 Contrast to Noise Ratio

Figure 5-3 shows the results of the CNR measurements. Data points in the graphs are mean values of the repeated measurements, variance is indicated with the errorband ($\mu \pm \sigma$). No significant difference between the CNR of the ICE ultrasound probe was observed compared to CNR of the X8-2t and S7-3t ultrasound probe, except for the -9 dB target. At the -9 dB target, the CNR of the ICE probe ($\text{CNR}_{\text{ICE}} = 4.3 \pm 0.6$) was higher than the CNR of the X8-2t and S7-3t ($\text{CNR}_{\text{X8-2t}} = 3.2 \pm 0.3, \text{CNR}_{\text{S7-3t}} = 1.4 \pm 0.1$).

5-1-3 Spatial Resolution

Figure 5-2 shows the lateral and axial dimension (Δ_L, Δ_A) of the pins in the ultrasound image as a function of depth (d). Data points in the graphs are mean values of the repeated measurements, variance is indicated with the errorband ($\mu \pm \sigma$). The spatial resolution measurements in figure 5-2A show that the lateral and axial resolution of the ICE probe are superior to the lateral and axial resolution of the X8-2t and S7-3t probe.

The average ratio between the lateral pin size (Δ_L) of the ICE ultrasound probe and X8-2t ($\Delta_{\text{L, ICE}}/\Delta_{\text{L, X8-2t}}$) $= 0.8 \pm 0.2$, and for the S7-3t ($\Delta_{\text{L, ICE}}/\Delta_{\text{L, S7-3t}}$) $= 0.6 \pm 0.2$. The average ratio between the axial pin size (Δ_A) of the ICE ultrasound probe and X8-2t ($\Delta_{\text{A, ICE}}/\Delta_{\text{A, X8-2t}}$) $= 0.7 \pm 0.1$, and for the S7-3t ($\Delta_{\text{A, ICE}}/\Delta_{\text{A, S7-3t}}$) $= 0.7 \pm 0.1$.

It was observed that the lateral resolution of the ICE ultrasound probe strongly depends on imaging plane rotation. Rotating the imaging plane 60° decreases lateral resolution of the ICE ultrasound probe with a factor of approximately 2 (figure 5-2B). ($\Delta_{\text{L, ICE}}/\Delta_{\text{L, X8-2t}}$) $= 1.4 \pm 0.3$, and ($\Delta_{\text{L, ICE}}/\Delta_{\text{L, S7-3t}}$) $= 1.2 \pm 0.2$. Axial resolution was not significantly affected by rotation of the imaging plane. ($\Delta_{\text{A, ICE}}/\Delta_{\text{A, X8-2t}}$) $= 0.6 \pm 0.1$, and ($\Delta_{\text{A, ICE}}/\Delta_{\text{A, S7-3t}}$) $= 0.7 \pm 0.1$.

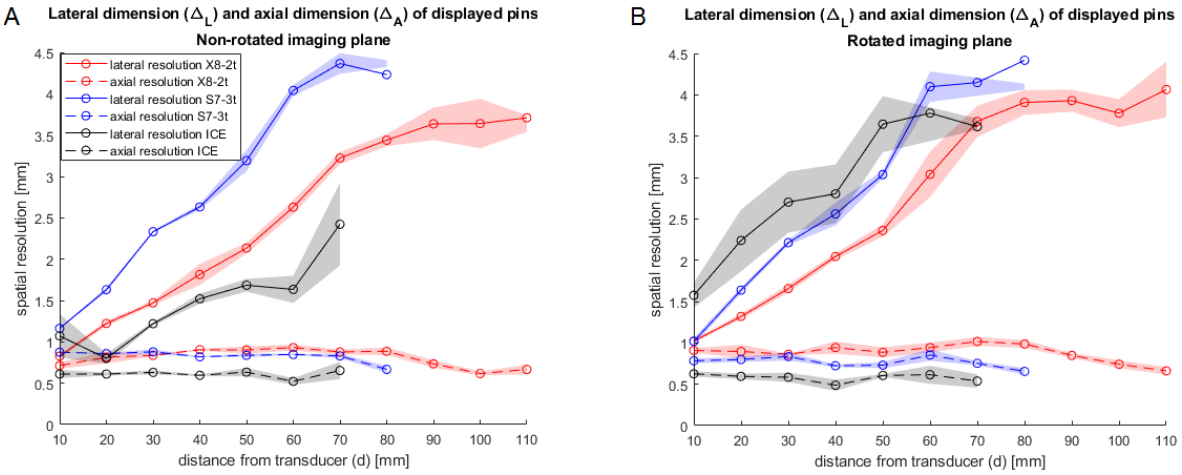

Figure 5-2: A: The lateral and axial dimension (Δ_L, Δ_A) [mm] of the pins at depth (d) [mm]. **B:** $\Delta_L(d), \Delta_A(d)$, measured with rotated imaging plane (X8-2t, S7-3t $90°$; ICE ultrasound probe $60°$). Data points are mean values of the measurement $(N = 6)$, variance is indicated with the errorband $(\mu \pm \sigma)$.

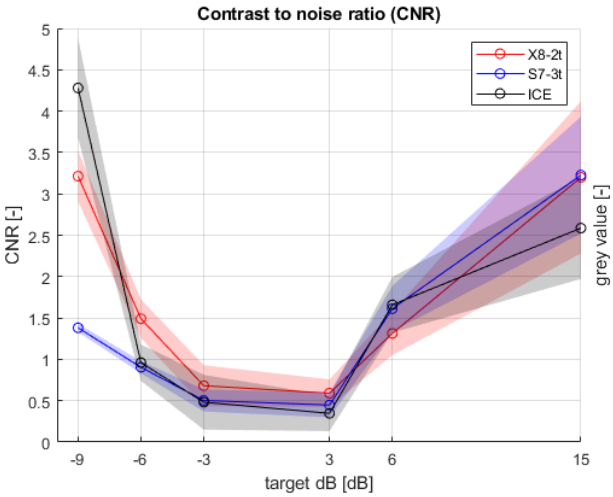

Figure 5-3: CNR for the X8-2t, S7-3t and ICE ultrasound probe. Data points are mean values of the measurement $(N = 6)$, variance is indicated with the errorband $(\mu \pm \sigma)$.

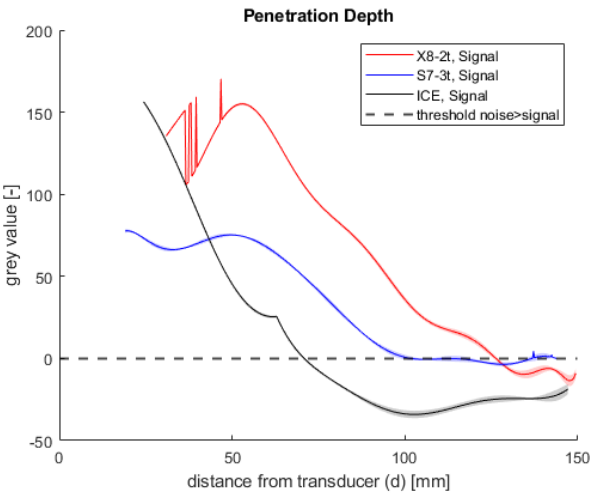

Figure 5-4: Penetration depth of the signal. Data points are mean values of the measurement $(N = 6)$, variance is indicated with the errorband $(\mu \pm \sigma)$.

5-1-4 Penetration Depth

Figure 5-4 shows the results of the ultrasound penetration depth measurements. Ultrasound penetration depth of the ICE ultrasound probe ($PD_{ICE} = 70.9 \pm 0.8$ mm) was significantly less as the penetration depth of the X8-2t and S7-3t probe ($PD_{X8\text{-}2t} = 126.4 \pm 0.7$ mm, $PD_{S7\text{-}3t} = 100.7 \pm 0.3$ mm).

5-2 IQ Comparison: Trans-Balloon US vs. Direct US Imaging

This section presents the results of the second study of this master thesis. In this study, the image quality of the ICE ultrasound probe was compared to image quality of the intra-balloon ICE ultrasound probe to investigate the influence of the balloon on image quality. Image quality was assessed based on measurement of the contrast resolution, CNR, spatial resolution and penetration depth. Measurements were repeated 20 times, and results are reported with mean and standard deviation ($\mu \pm \sigma$).

5-2-1 Contrast Resolution

Figure 5-5A shows the measured grey value of each target plotted against the target dB value. Figure 5-5B shows a linear least-square regression line through the datapoints in figure 5-5A. The errorband indicates the 95% confidence interval of the linear fit. The regression coefficient of the line is defined as the "gamma" (γ), which is a measure for the contrast resolution.

Multiple regression analysis was used to test if the regression coefficient for the ICE probe without balloon and the ICE probe with balloon are significantly different. The gamma of the ICE probe without balloon ($\gamma_{ICE,\ no\ balloon} = 5.1$) and the ICE probe with balloon ($\gamma_{ICE,\ balloon} = 5.0$) were not significantly different, $t(1) = 0.11$, $p = 0.913$.

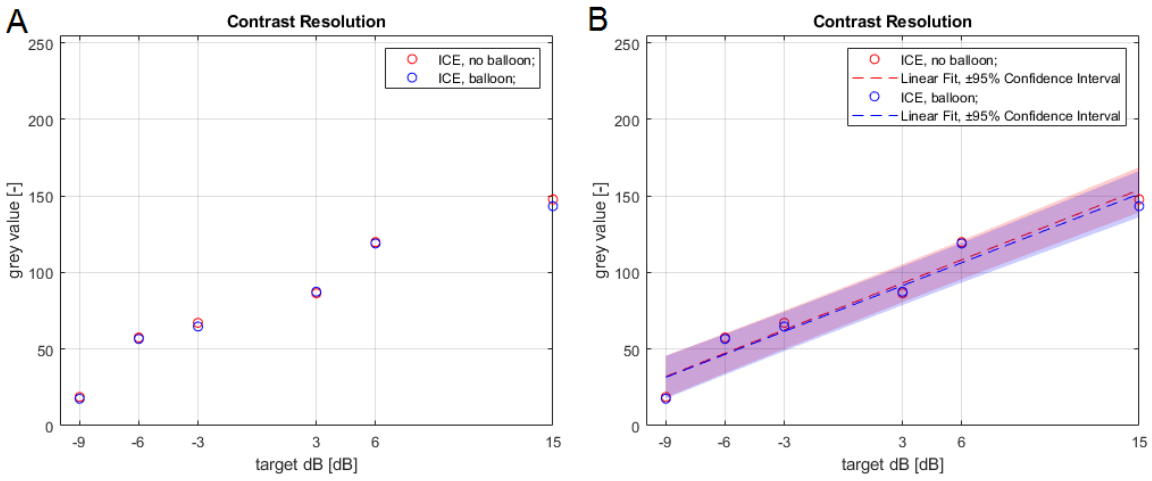

Figure 5-5: A: Mean grey value of each target plotted against target echo level (dB). **B:** Linear fit through datapoints, the errorband indicates the 95% confidence interval of the linear fit. Steepness of the line is the contrast resolution of the probe.

5-2-2 Contrast to Noise Ratio

Figure 5-7 shows the results of the CNR measurements. Data points in the graphs are mean values of the repeated measurements, variance is indicated with the errorband ($\mu \pm \sigma$). No significant difference between the CNR of the ICE probe without balloon and the probe with balloon was observed.

5-2-3 Spatial Resolution

Figure 5-6 shows the lateral and axial resolution (Δ_L, Δ_A) as a function of depth (d). Data points in the graphs are mean values of the repeated measurements, variance is indicated with the errorband ($\mu \pm \sigma$). The lateral and axial resolution show no significant differences between the probe without balloon and the probe with balloon.

The average ratio between the lateral pin size (Δ_L) of the ICE ultrasound probe with balloon and without balloon ($\Delta_{\text{L, balloon}}/\Delta_{\text{L, no balloon}}$) $= 1.1 \pm 0.1$,

The average ratio between the axial pin size (Δ_A) of the ICE ultrasound probe with balloon and without balloon ($\Delta_{\text{A, balloon}}/\Delta_{\text{A, no balloon}}$) $= 1.0 \pm 0.1$.

5-2-4 Penetration Depth

Figure 5-8 shows the penetration depth of the probe with and without balloon. No significant difference between the penetration depth of the ICE ultrasound probe without balloon ($69.8 \pm$ 1.8 mm) and the ICE ultrasound probe with balloon (71.1 ± 1.3 mm) was observed, t(1) = 1.43, p = 0.185.

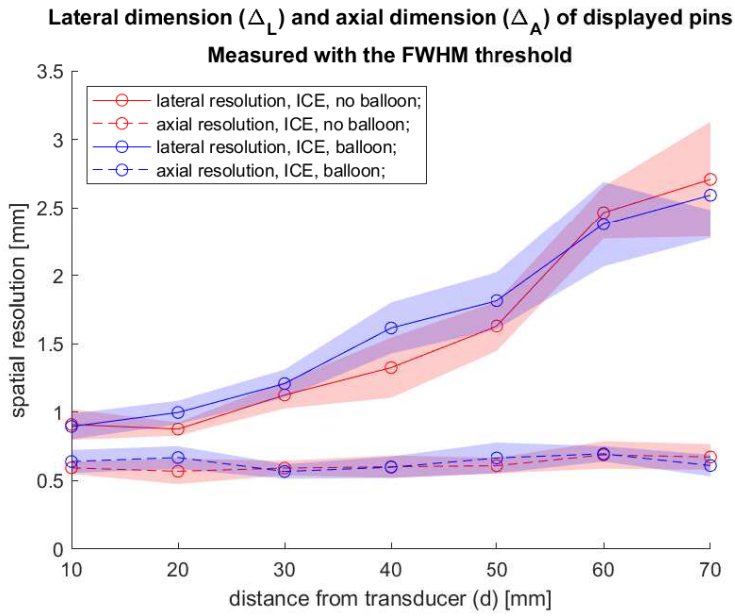

Figure 5-6: The lateral and axial dimension (Δ_L, Δ_A) [mm] of the pins at depth (d) [mm]. Data points are mean values of the measurements $(N = 20)$, variance is indicated with the errorband $(\mu \pm \sigma)$.

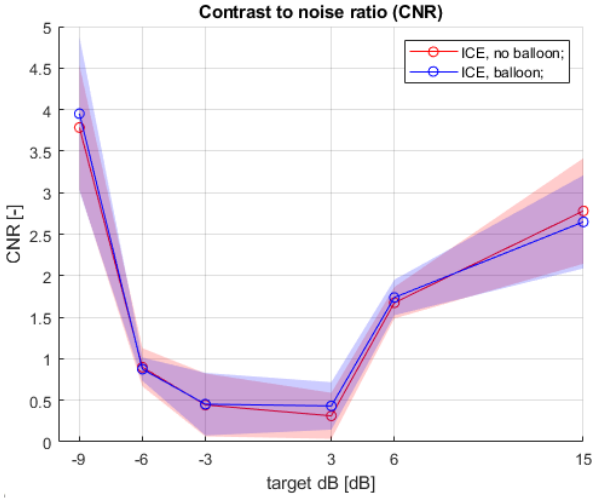

Figure 5-7: CNR for the probe without balloon and the probe with balloon. Data points are mean values of the measurement $(N = 20)$, variance is indicated with the errorband $(\mu \pm \sigma)$.

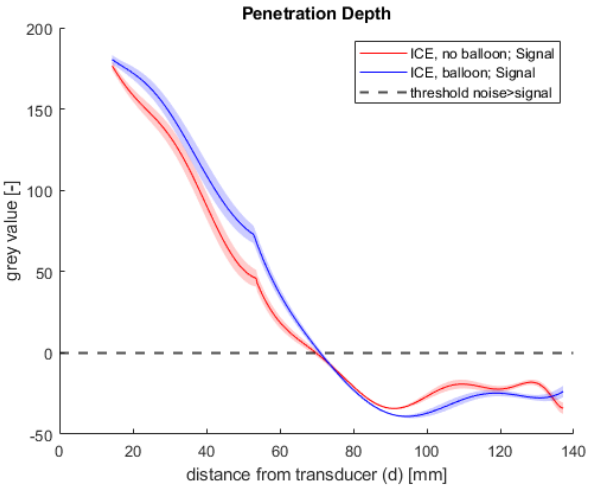

Figure 5-8: Penetration depth of the signal. Data points are mean values of the measurement $(N = 20)$, variance is indicated with the errorband $(\mu \pm \sigma)$.

Chapter 6

Discussion

The goal of this thesis was to investigate whether image quality of miniaturized trans-balloon Transesophageal Echocardiography (TEE) is sufficient for real-time imaging during Atrial Fibrillation (AF) ablation procedures. To investigate this, a research question was formulated, which was divided in the following sub-questions:

- Sub-question 1: What is image quality of the miniaturized ultrasound probe compared to the image quality of the currently used standard TEE probes?
- Sub-question 2: How does a transducer balloon influence the image quality of the miniaturized ultrasound probe?

To answer these questions, a method for objective image quality assessment was developed, and two studies were conducted.

First, the developed image quality assessment method was applied in a study to compare the image quality of a miniaturized ultrasound probe to image quality of current state of the art TEE probes. In this study, the image quality of the Intra-Cardiac Echocardiography (ICE) miniaturized ultrasound probe was compared to to the X8-2t and S7-3t TEE ultrasound probe.

In a second study, the influence of a water-filled transducer balloon on image quality was studied by comparing the image quality of the ICE ultrasound probe without a balloon to the image quality of the ICE ultrasound probe with the balloon around the transducer.

This chapter summarizes and discusses the results and study limitations. Furthermore, the clinical relevance of the results is discussed, and some recommendations for further research are given. Finally, other areas of application for miniaturized, trans-balloon ultrasound imaging are discussed.

6-1 Summary and Discussion of Measurement Results

6-1-1 IQ Comparison: Miniaturized TEE vs. Normal TEE

In the first study of this master thesis, image quality of the ICE ultrasound probe was compared to image quality of the X8-2t and S7-3t TEE probe. The results have shown that, despite its significantly smaller size, image quality of the miniaturized ultrasound probe is comparable to image quality of the larger TEE probes, but that spatial resolution strongly depends on image plane rotation and that the ultrasound penetration depth of the miniaturized probe is less than that of the TEE probes.

The linear fit through the points in figure 5-1 shows how the grey value changes as function of echo dB level. The steepness of the line is the contrast resolution of the probe. A steep line means that a small difference in echo intensity results in a large change in grey value, which corresponds to a good contrast resolution. Figure 5-1 shows that the contrast resolution lines of the ICE, X8-2t and S7-3t are approximately overlapping, which means that contrast resolution of the probes is not significantly different.

The Contrast-to-Noise Ratio (CNR) measurements in figure 5-3 show no important differences between CNR of the probes. However, it is important to note that CNR measurements were performed using targets at a depth of 25 mm below the scanning surface. At this depth, the observed differences in CNR between the probes were minor. At greater depth it is expected that the CNR of the X8-2t, S7-3t and ICE shows larger differences as attenuation of the signal increases exponentially with depth.

The lateral and axial resolution as function of depth (d) in the ultrasound image are shown in figure 5-2. It is observed that the axial resolution remains constant with depth, but that the lateral resolution changes as function of depth. This observation is in accordance with the theory in chapter 2, section 2-3, where it was stated that the axial resolution is independent of beam geometry and depends on Spatial Pulse Length (SPL) only. The lateral resolution depends on the width of the ultrasound beam, which changes with distance from the transducer. Consequently, the lateral resolution is depth dependent.

Figure 5-2 shows that the lateral resolution of the ICE probe is superior to that of the X8-2t and S7-3t probe. However, it is important to mention that the lateral resolution of the ICE probe strongly depends on the rotation angle of the imaging plane, due to the geometry of the transducer array. The transducer array of the ICE has a rectangular shape, which means that more piezo-elements are along the long axis of the array than on the short axis of the array. When the imaging plane is aligned with the long axis of the transducer array (0^o rotation), the maximum amount of elements is involved in forming the image, resulting in maximum achievable image quality. In the worst case, the image plane is rotated 90^o (aligned with the short axis of the rectangular transducer), and a lower amount of piezo-elements is involved in forming the image, resulting in a significantly lower spatial resolution compared to the situation where the image plane is not rotated. Figure 6-1 shows a sketch of the rotated and non-rotated imaging plane.

The measurement results in figure 5-2A were obtained with 0^o rotation of the imaging plane. Figure 5-2B shows the results when the imaging plane of the X8-2t, S7-3t and ICE are rotated 90^o, 90^o, and 60^o respectively. Increasing the image plane rotation angle of the ICE above 60^o resulted in a too low image quality to perform measurements.

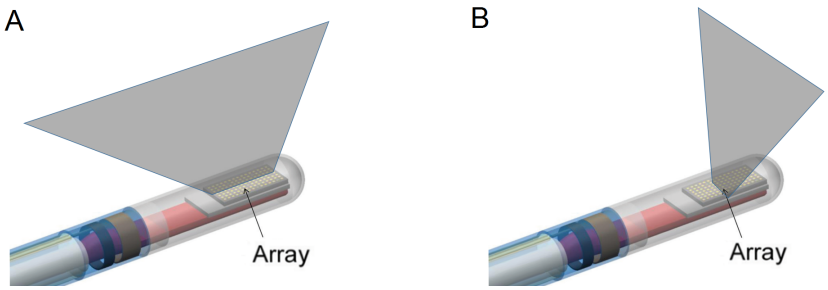

Figure 6-1: A: Imaging plane rotated 0°, the plane is aligned with the long axis of the rectangular transducer array. **B:** Imaging plane rotated 90°, the plane is aligned with the shortest axis of the array. Figure adapted from [44].

Figure 5-2B shows that the lateral resolution of the ICE decreases with a factor of approximately 2, while the lateral resolution of the X8-2t and S7-3t does not significantly change compared to the results in figure 5-2A. Lateral resolution of the X8-2t and S7-3t does not change because the transducer array of these probes is designed such that spatial resolution is independent of the image plane rotation angle. Contrary to this, the rectangular design of the transducer array of the ICE results in a strongly rotation angle-dependent spatial resolution. Figure 5-2A and 5-2B show that the axial resolution of the X8-2t, S7-3t and ICE probe does not depend on the imaging plane rotation angle. This is as expected, since the axial resolution is independent of beam geometry. Therefore, rotation of the imaging plane does not affect axial resolution.

Figure 5-4 shows that the penetration depth of the ICE probe is significantly less compared to the penetration depth of the S7-3t and X8-2t ultrasound probe (70.9 ± 0.8 mm vs. 126.4 ± 0.7 mm, 100.7 ± 0.3 mm). This difference is mainly explained by power (P [W]) and frequency (f [MHz]) of the ultrasound probe. Ultrasound penetration depth decreases exponentially with decreasing power and increasing frequency. The ICE has the lowest penetration depth due to the high frequency and lower power compared to the X8-2t and S7-3t ultrasound probe.
The difference in penetration depth was also observed in the spatial resolution measurements in figure 5-2. The curve of the ICE probe ends at 70 mm, because pins for the spatial resolution measurement in the ultrasound image could not be resolved at greater depth.

6-1-2 IQ Comparison: Trans-Balloon US vs. Direct US Imaging

In the second study of this master thesis, the image quality of the ICE ultrasound probe was compared to the image quality of the intra-balloon ICE ultrasound probe to study the influence of the balloon on image quality.

Compared to direct ultrasound imaging, trans-balloon ultrasound imaging adds extra interfaces between the transducer and the insonated tissue: the ultrasound waves travel from the transducer in the medium inside the balloon (water), than from the medium into the balloon wall, and from the balloon wall into the insonated tissue. It was expected that these extra interfaces would absorb some of the ultrasound energy, which results in a lower ultrasound image quality. However, the results in figure 5-5 to 5-8 have shown that the influence of the water-filled balloon on image quality is negligible.

6-2 Study Limitations and Recommendations

A limitation of the applied Image Quality Assessment (IQA) method is that this method is suitable for measurements in the 2D imaging mode only. In clinical practice, a 3D ultrasound volume is used to select a 2D plane through the 3D ultrasound volume, and this 2D imaging plane is used for clinical diagnostics or treatment guidance. Therefore, a 3D ultrasound IQA method would possibly give more valuable results. However, since 3D ultrasound IQA software and phantoms are not available yet, it was decided to measure and compare image quality using a 2D IQA method. The authors decided that this 2D IQA method still yields valid and useful results, since in clinical practice the 3D volume is only used to select a 2D plane, while the 2D imaging plane is used for diagnosis and assessment of the anatomy. An advantage of the IQA method that was developed in this thesis, is that it can be used to assess image quality of any ultrasound probe, and is not just limited to the probes that were assessed in this thesis.

Another limitation is that the ICE catheter that was used for image quality measurements is not intended for TEE imaging. In the first study of this master thesis, image quality of the Philips ICE catheter was compared to image quality of the Philips X8-2t and S7-3t TEE probe. The goal of this study was to investigate whether the image quality of a miniaturized TEE probe is comparable to that of currently used TEE probes. Due to its small size, the ICE catheter was used as miniaturized ultrasound probe for comparison with TEE probes, although the ICE catheter is not intended for TEE imaging. The ICE probe is developed as a catheter for intracardiac ultrasound imaging during minimally invasive Structural Heart Disease (SHD) procedures.
However, since imaging characteristics of the ICE catheter are likely to be very similar to a TEE probe of the same size as the ICE catheter, results of this study are useful as a first estimate of the image quality of a miniaturized TEE probe. In a follow-up study, the image quality of standard TEE probes can be compared to the miniaturized TEE probe but this was not possible during this study because the miniaturized TEE probe is still under development.

In the second study of the thesis, trans-balloon ultrasound image quality was compared to direct ultrasound image quality to study the influence of the water-filled balloon around the transducer of the miniaturized ultrasound probe. The results have shown no significant influence of the balloon on image quality. However, a limitation to these results is that the balloon was inflated with only 10 ml of water, which does not fully deploy the balloon (figure 6-2B). For the intended application of trans-balloon TEE imaging, the water-filled balloon needs to be inflated to a diameter of approximately 20 mm (30 ml) to be fully in contact with the esophagus (figure 6-2A).
The reason why the balloon was not further inflated, was that inflating the balloon to a diameter of 20 mm induced severe mirroring artifacts of the balloon wall, which influenced the image quality such that measurements could not be performed (see figure 6-3A). It was observed that these artifacts became stronger with increasing balloon diameter. Therefore, it was decided to perform measurements with a minimum diameter of the balloon (figure 6-3B). The mirroring artifacts are due to the balloon-air interface where the balloon is not in contact with the flat scanning surface of the phantom. At the balloon-air interface, all scattered ultrasound waves are reflected back, and are detected by the transducer as an echo. This echo causes an artifact in the image (see figure 6-4).

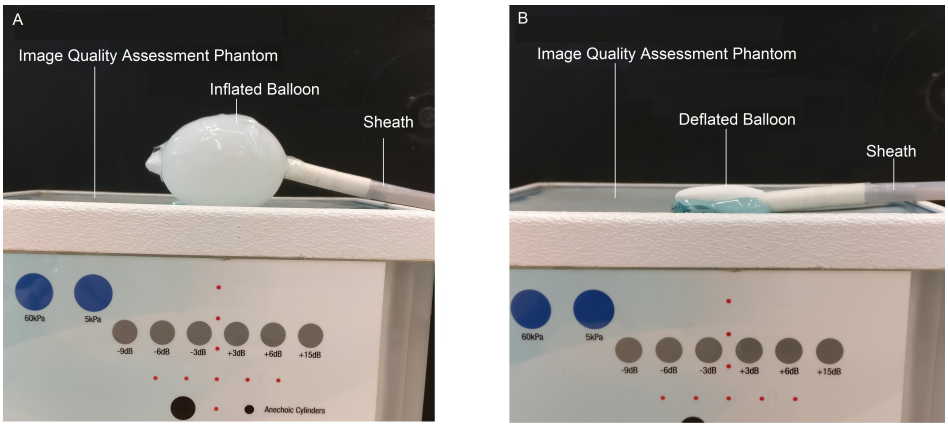

Figure 6-2: A: Picture of the ICE ultrasound probe inserted in the fully inflated balloon. **B:** Picture of the ICE ultrasound probe inserted in the deflated balloon.

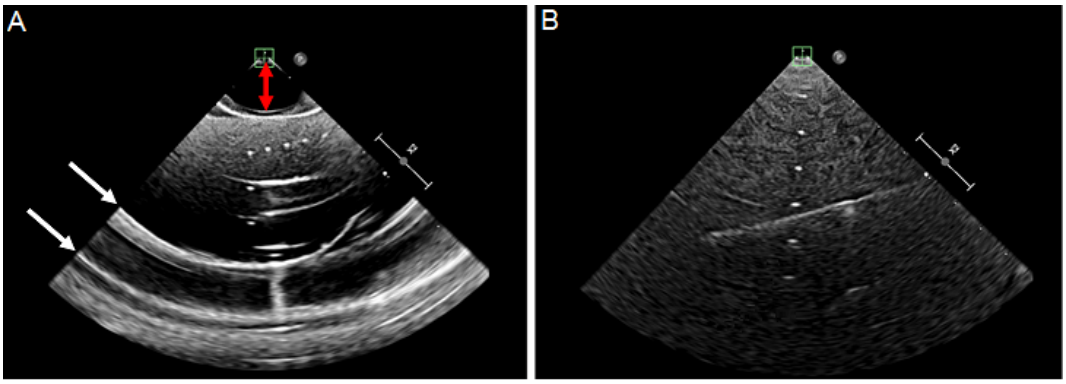

Figure 6-3: A: Ultrasound image of the phantom with the balloon inflated to a diameter of 20 mm (red arrow). The balloon-air interface causes severe mirroring artifacts of the balloon wall (indicated with the white arrows). **B:** Mirroring artifacts disappear when the diameter of the balloon was reduced.

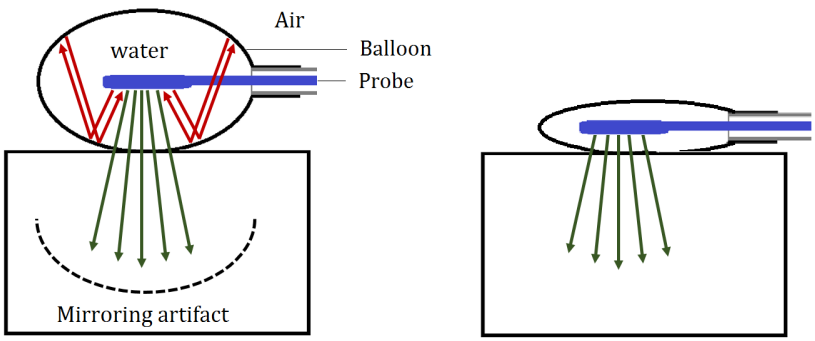

Figure 6-4: When the balloon was fully inflated, mirroring of the balloon wall causes artifacts in the ultrasound image. These mirroring effects occur from reflected ultrasound waves at the balloon-air interface, where the balloon is not in contact with the phantom surface. It was observed that deflating the balloon reduced the mirroring artifacts.

It is expected that these mirroring artifacts will not occur when the balloon is inserted in the esophagus, because the esophageal wall entirely surrounds the balloon. When the tissue entirely surrounds the balloon, scattered ultrasound signals are absorbed in the tissue, and will not reflect on the balloon-air interface as it was the case in the measurement setup.
It is recommended to perform a follow-up study, where the balloon is inserted in a phantom with a tubular cavity that entirely surrounds the balloon to validate whether this reduces the mirroring artifacts.

6-3 Clinical Relevance of Thesis Research

The previous sections discussed the results and study limitations. In this section, the clinical relevance, and limitations of trans-balloon miniaturized TEE for application in AF ablation are discussed.

6-3-1 FOV improvement

In the introduction of this thesis it was stated that conventional TEE provides a limited view of the Pulmonary Veins (PV) and posterior Left Atrium (LA) wall, due to the close proximity of these structures to the transducer surface. At this short distance, the conical shaped Field of View (FOV) is too narrow to include te ostia of the Left Superior Pulmonary Vein (LSPV), Left Inferior Pulmonary Vein (LIPV), Right Superior Pulmonary Vein (RSPV) and Right Inferior Pulmonary Vein (RIPV) entirely in the FOV [6, 5, 7, 4, 23]. This limits the use of TEE for imaging of ablation procedures.

Miniaturized trans-balloon TEE was proposed as a solution for the limited FOV, as the balloon serves as primary coupling medium between the transducer and esophageal wall. This eliminates the need to press the transducer to the esophageal wall, and allows to shift the transducer posteriorly, increasing the distance between the transducer and esophageal wall. Increasing the distance between the transducer and the esophageal wall brings the ostia of the PV and LA wall further in the FOV.

Figure 6-5 illustrates the FOV improvement using trans-balloon miniaturized TEE. Figure 6-5A shows the current situation, where the TEE probe is pressed against the esophageal wall, resulting in a suboptimal view of the LA where the ostia of the PV are outside the FOV. In this situation, the distance d between transducer and LA wall is typically in the range of 3 to 5 mm [6]. The esophagus has a diameter of approximately 20 mm [5], which means that the distance d between transducer and LA wall can be increased with approximately 20 mm using a trans-balloon miniaturized ultrasound probe. Figure 6-5B shows the situation when a miniaturized trans-balloon TEE probe is used for imaging. Increasing the distance d with 20 mm results in an improved FOV, including the ostia of the PV and LA posterior wall.

Research in this thesis has shown that trans-balloon ultrasound imaging is possible, and that image quality is not negatively affected by the water-filled balloon surrounding the transducer of the miniaturized ultrasound probe. However, some limitations regarding the spatial resolution and penetration depth of the miniaturized ultrasound probe were discovered as well. The impact of these limitations for clinical application of trans-balloon miniaturized ultrasound is discussed in the following subsections.

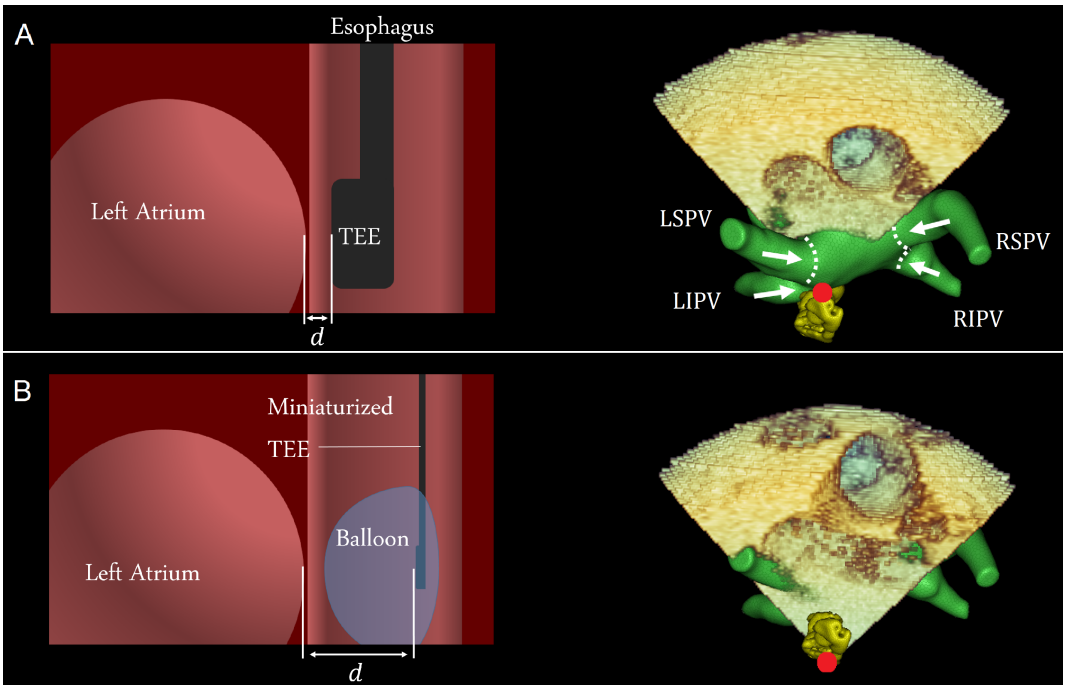

Figure 6-5: **A:** Due to the short distance d between transducer and LA, ostia of the PV and posterior LA wall are outside the FOV. **B:** The distance d is increased with 20 mm using a water-filled miniaturized TEE probe. Ostia of the PV and posterior LA wall are now in the FOV.

6-3-2 Spatial Resolution

The results have shown that spatial resolution of the ICE miniaturized ultrasound probe strongly depends on rotation of the imaging plane. In section 6-1 it was explained that this rotation-dependency of the spatial resolution is caused by the geometry of the transducer array. Spatial resolution of the ICE is optimal when imaging plane is not rotated, and decreases with rotation angle of the imaging plane. It was observed that the lateral resolution decreases with a factor 2 when imaging plane was rotated from 0^o to 60^o.

In clinical practice, the 2D image plane is often rotated such that it is aligned with the anatomical structure of interest. Examples of frequently used standard TEE views for assessment of the LA are the mid-esophageal, four-chamber view (image plane rotated 90^o), mid-esophageal short axis view (image plane rotated 30^o to 45^o), or the mid-esophageal long axis view (image plane rotated -40^o to -50^o) [2, 45]. Figure 6-6 shows the image plane in its neutral position, and in the standard views for LA assessment.

With the imaging plane rotated above +/-60^o, the ICE ultrasound probe operates in its sub-optimal range and the lateral resolution is decreased with a factor >2 w.r.t zero rotation of the imaging plane. Especially the mid-esophageal four-chamber view is a sub-optimal view for the miniaturized ultrasound probe, as the imaging plane is rotated 90^o. For monitoring of AF ablation, good spatial resolution is required to visualize for example tissue-catheter contact during ablation.

Although this study enables to quantify the spatial resolution of the miniaturized ultrasound probe and its relation with plane rotation angle, it is difficult to conclude from the measure-

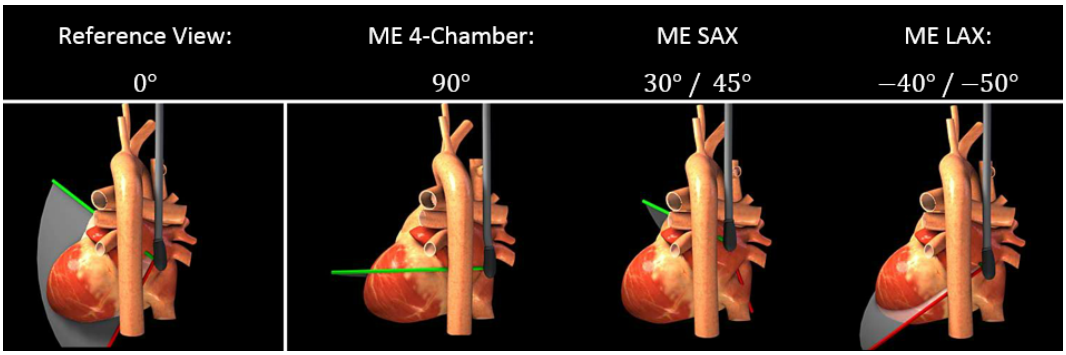

Figure 6-6: Image plane rotation of the mid-esophageal four-chamber view, mid-esophageal short axis view and mid-esophageal long axis view.

Table 6-1: Distance (d) of the posterior LA wall and the ostia of the 4 PV to the esophageal wall. Distance to the transducer is approximately $d + 20$mm when the distance between esophageal wall and transducer is 20 mm.

Anatomical Strucure	Distance to esophageal wall d mm	Distance to transducer $d + 20$ mm
Posterior LA wall	$2 - 5$	$22 - 25$
LSPV	$8 - 14$	$28 - 34$
LIPV	$3 - 11$	$23 - 31$
RSPV	$20 - 30$	$40 - 50$
RIPV	$16 - 20$	$36 - 40$

ment results whether image quality is sufficient for AF ablation. It is recommended to perform an in-vivo experiment with experts to judge whether image quality of the miniaturized probe with rotated imaging plane is sufficient for the intended application of TEE imaging.

6-3-3 Penetration Depth

Another limitation of the miniaturized ultrasound probe is its limited ultrasound penetration depth. Results have shown that the large TEE probes reach a penetration depths of ±120 mm, while the miniaturized ultrasound probe reached a penetration depth of only ±70mm. In section 6-1 it was explained that the lower penetration depth is due to the low power and high frequency of the miniaturized ultrasound probe.

However, it is expected that the limited penetration depth will not be a major limitation for application in AF ablation procedures, since the anatomical structures of interest are relatively close close to the transducer. The distance d of the posterior LA wall and four PV to the esophageal wall is shown in table 6-1. When the distance between the transducer and the esophageal wall is 20 mm, the distance between these anatomical structures and the transducer is approximately $d + 20$ mm. Table 6-1 shows that, even with maximum distance between the esophageal wall and transducer, the anatomical structures of interest are at a distance well below 70 mm from the transducer, which is in the range of the penetration depth of the ultrasound signal.

6-4 Other Areas of Application

Trans-balloon miniaturized ultrasound is relevant in more clinical settings as just in AF ablation procedures.

One example is pediatric TEE imaging. Usually, smaller TEE probes are used for TEE examination of infants and children. However, due to the smaller transducer area, achieving stable acoustic coupling in the esophagus is more difficult. A water-filled balloon around the transducer increases the area that is in contact with the esophagus, providing a more stable acoustic coupling.

Another area of application that can benefit from miniaturized trans-balloon TEE is hemodynamic TEE (hTEE). In the critically ill patient on the intensive care unit, the hemodynamic status is continously monitored using small hTEE probes. Since the hTEE probe is in place for such a long time (up to 72 hours), it is miniaturized to reduce the risk on laryngopharyngeal damage [46]. However, similar to pedeatric TEE, the small transducer area makes it difficult to maintain acoustic coupling for such a long time. To facilitate a more stable acoustic coupling, the transducer can be inserted in a water-filled balloon.

A more far-fetched area of application is Endobronchial Ultrasound (EBUS). EBUS elastography is an imaging modality that uses ultrasound to detect and monitor cancer tumors in the lungs. Tumor tissue is stiffer as the surrounding tissue, and this difference in elasticity is used to visualize tumors using EBUS [47]. Since the lungs are filled with air, a water-filled balloon is required to achieve acoustic coupling. Miniaturizing the ultrasound probe allows to navigate the probe deeper in the lungs, which enables to image a greater extend of the lung tissue using EBUS.

Chapter 7

Conclusion

Atrial fibrillation (AF) ablation requires accurate tracking of catheter position and tissue contact for successful and effective treatment. Therefore, real-time imaging of the catheters and anatomical structure is of great importance. In this thesis, trans-balloon, miniaturized Transesophageal Echocardiography (TEE) is proposed as imaging modality for real-time imaging during AF ablation procedures.

This thesis aimed to investigate whether image quality of trans-balloon, miniaturized TEE is sufficient for intraprocedural imaging of AF ablation procedures. To investigate this approach, a method for objective Image Quality Assessment (IQA) was developed. This IQA method was used to compare image quality of a miniaturized ultrasound probe to current state of the art TEE probes, and to investigate influence of the balloon on image quality. The results indicate that the developed IQA method was effective, providing accurate and repeatable image quality measurements.

The study has shown that image quality of the miniaturized ultrasound probe was comparable to image quality of the current state of the art TEE probes. Furthermore, it was observed that the balloon not negatively impacts image quality in the test setup, but this result has to be validated in an in-vivo setting. Imaging depth of the miniaturized probe is less compared to state of the art probes, but this will not be a major limitation during AF ablation procedures, since the anatomical structures of interest are well within the imaging range of the transducer. A limitation of the miniaturized ultrasound probe is that spatial resolution decreases with increasing image plane rotation angle. Rotating the imaging plane is common practice in TEE imaging, which means that rotation-dependent spatial resolution is undesired. It is therefore recommended to perform a review study involving clinical experts to judge whether image quality of the miniaturized ultrasound probe with rotated imaging plane is acceptable.

The results of this research indicate that trans-balloon miniaturized TEE can provide real-time ultrasound imaging of the left atrium during ablation procedures. There is a continuous demand for more accurate and real-time imaging techniques during catheter based treatment of atrial fibrillation. The research in this thesis provides a theoretical framework to measure and compare image quality of ultrasound probes, which is an important first step in the de-

velopment of a new, real-time and non invasive imaging technique for imaging of AF ablation procedures.

Appendix A

Article 1

Objective Image Quality Assessment of Ultrasound Probes used for Trans Esophageal Echocardiography (TEE) - Report I

Grandia, L.

Abstract— **Miniaturized, trans-balloon transesophageal echocardiography (TEE) potentially improves intraprocedural imaging of atrial ablation procedures. This study aims to investigate whether image quality of a miniaturized TEE probe is sufficient for intraprocedural imaging of atrial ablation procedures. Image quality of the miniaturized ultrasound probe was compared to image quality of current state of the art TEE probes based on objective assessment of ultrasound phantom scans. Results have shown that contrast resolution and contrast to noise ratio of the miniaturized probe are equal to the large TEE probes, but that penetration depth is significantly less. Furthermore it was observed that spatial resolution of the miniaturized probe decreases with rotation of the imaging plane.**

Keywords—Ultrasound, Image quality, Objective assessment, Performance testing, Quality assurance, Contrast resolution, Spatial resolution, UltraIQ

I. Introduction

This article is part of a MSc thesis research study. The goal of the thesis is to investigate the feasibility of miniaturized, trans-balloon, trans-esophageal echocardiography (TEE) as imaging modality for intraprocedural monitoring of atrial ablation (AF) procedures.

During AF ablation procedures, atrial fibrillation is treated by catheter-based ablation of the left atrial tissue. These lesions in the tissue isolate parts of the left atrium, which prevents electrical signals to spread over the atria. During AF ablation procedures, real time imaging of the cardiac structure and the ablation catheters is required in order to perform ablation accurately in the left atrium. Effectiveness and success rates of ablation procedure strongly depend on the accuracy of ablation.

Currently used TEE probes are not suitable for real time imaging during ablation, due to their high level of discomfort for the patient, and limitations in the field of view (FOV).

In this MSc thesis study it is proposed that miniaturized, trans-balloon TEE can provide real-time imaging of the cardiac anatomy during ablation procedures, which potentially improves efficacy and outcome of AF ablation procedures. However, before miniaturized trans-balloon TEE can be applied in clinical practice, it is required to validate that the image quality of the miniaturized probe is sufficient for the intended application.

In this study, the image quality of the Philips IntraCardicac Echocardiography (ICE) miniaturized ultrasound probe is compared to image quality of current state of the art TEE probes (Philips X8-2t TEE probe and Philips S7-3t TEE probe). The image quality is assessed based on objective analysis of phantom scan images using the image quality assessment software of UltraiQ. This paper presents the method and results of the image quality comparison.

A. Research Objective

This study aims to objectively compare the image quality of the miniaturized ultrasound probe (Philips ICE ultrasound probe) to current state of the art TEE probes (Philips X8-2t TEE probe, Philips S7-3t TEE probe). The results of this study are used in a feasibility study to the miniaturized trans-balloon ultrasound imaging for TEE imaging.

II. Materials

A. Image Quality Assessment Phantoms

Standardized ultrasound image quality assessment phantoms were used for measurement of the image quality. Image quality parameters were quantified by objective analysis of the ultrasound images of these phantoms.

Contrast resolution and spatial resolution were measured using the UltraIQ general purpose ultrasound phantom (CablonMedical, Leusden, Netherlands). The attenuation coefficient and speed of sound of the phantom base material are similar to those in parenchymal soft tissue (0.5 dB/(cm·Mhz) $\pm 5\%$ and 1450 m/s respectively). The base material contains a vertically aligned group of 'pins', and a group of 6 echogenic, cylindrical grey targets. Each grey target reflects the incident ultrasound signal with a specific echo intensity (I_T). The background material reflects the incident ultrasound signal with intensity (I_{BG}). The echo intensity of the targets (I_T) with respect to the echo intensity of the background (I_{BG}) is expressed in decibel (dB):

$$\text{target dB level} = 10 \cdot \log\left(\frac{I_T}{I_{BG}}\right) \tag{1}$$

The echogenic grey targets have a relative echo intensity with respect to the background of -9dB, -6dB, -3dB, 3dB, 6dB and 15dB respectively. The distance between the center of the targets and the surface of the phantom is 25 mm (figure 1).
Penetration depth of the ultrasound signal was measured using the UltraiQ uniformity phantom (CablonMedical, Leusden, Netherlands). This phantom consists of a block of uniform echogenic material without any targets.

B. Ultrasound Probes

Ultrasound images were obtained using the 3D-TEE (X8-2t, Philips, Reedsville, PA, USA), 2D-TEE-mini (S7-3t, Philips, Reedsville, PA, USA) ultrasound probes and the Intra-Cardiac Echocardiography (ICE) ultrasound catheter (Philips, Alajuela, Costa-Rica) (figure 2).

C. Ultrasound System and Software

The ultrasound images were acquired and stored in DICOM format using the Epiq 7Ci Ultrasound system (Philips, Bothell, WA, USA). The DICOM images

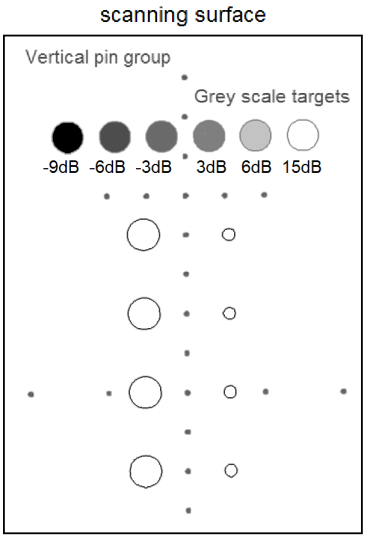

Fig. 1: The target pattern in the UltraIQ General Purpose Phantom (Cablon Medical, Leusden, Netherlands).

Fig. 2: From left to right: ICE, S7-3t, X8-2t

were analyzed with the UltraIQ ultrasound image quality assessment software (CablonMedical, Leusden, Netherlands). The results of the UltraiQ software were stored in Excel, and imported in MATLAB (R2018b) to visualize the data in graphs.

III. Methods

A. Image Quality Parameters

Image quality of the ICE ultrasound probe was compared to image quality of the X8-2t and S7-3t probe by objective image quality assessment of the ultrasound phantom scans. Image quality of the ultrasound images was assessed based on the following image quality parameters: contrast resolution, contrast-to-noise ratio (CNR), spatial resolution and penetration depth of the ultrasound signal. Each parameter is shortly discussed in this section. For a more detailed explanation of the image quality parameters, please refer to the thesis document, chapter 3.

The *contrast resolution* is defined as the smallest difference in echo intensity of a target (I_T) with respect to the echo intensity of the surrounding background (I_{BG}) that can be detected in the ultrasound image [1]. The contrast resolution depends on the mapping of echo intensity (I), to grey values (GV) in the ultrasound image. Good contrast resolution means that objects with low difference in echo intensity w.r.t. background ($I_T/I_{BG} \approx 1$), still can be resolved in the ultrasound image ($GV_T/GV_{BG} > 1$). Contrast resolution is determined by measuring the "gamma", defined as the increase in grey level per dB echo level (grey value/echo dB).

The *contrast-to-noise ratio* (CNR) is the contrast between background and target divided by the noise in the image [1]. The contrast between background and target is the absolute difference between the mean grey value in the target (GV_T) and the mean grey value in the background (GV_{BG}). The noise is the variance in pixel grey values within the target (σ_T^2) and background (σ_{BG}^2). The ratio between the contrast and the noise yields the CNR:

$$\text{CNR} = \frac{|GV_T - GV_{BG}|}{\sqrt{\sigma_T^2 + \sigma_{BG}^2}} \tag{2}$$

Spatial resolution is defined as the smallest distance between two closely spaced objects in the ultrasound image that can be resolved as separate. Points spaced closer as the spatial resolution cannot be resolved as two distinct points in the image. The spatial resolution of an ultrasound probe is determined by measuring the width of the point spread function (PSF) in axial and lateral direction. [1, 2]. Spatial resolution of ultrasound images is measured with 'axial resolution' and 'lateral resolution'.

The *penetration depth* (PD) of the ultrasound signal is defined as the depth in the ultrasound image where the signal-to-noise ratio (SNR) drops below one.
SNR is defined as the amplitude of the signal squared (A_S^2) divided by the amplitude of the noise in the signal (A_N^2) squared [3]:

$$\text{SNR} = \frac{A_S^2}{A_N^2} \tag{3}$$

Since the signal (amplitude of the returning echos) decreases with depth, and the noise originating from electronic components and signal amplification is depth-independent, the SNR decreases with depth. The depth where SNR is lower than one is the penetration depth of the ultrasound signal [4]:

$$\text{PD} := \text{SNR} < 1 \tag{4}$$

B. Experimental Design

In this study, three experiments were performed:
Experiment 1: scanning the image quality assessment phantoms with the X8-2t ultrasound probe;
Experiment 2: scanning the image quality assessment phantoms with the S7-3t ultrasound probe;
Experiment 3 scanning the image quality assessment phantoms with the ICE ultrasound probe.
A single experiment consists of a series of scans on the ultrasound image quality assessment phantoms. The scans were repeated $N = 6$ times to reduce the influence of stochastic effects.

C. Measurement Protocol

To objectively compare image quality of the ICE ultrasound probe to image quality of the X8-2t and S7-3t ultrasound probes, influence of system settings had to be eliminated. Therefore, the image acquisition and processing parameters were equal across all experiments. To compensate for the different pre-amplification levels of the probes, the overall gain of each probe was adjusted such that the average grey value in the ultrasound images was equal for all probes. The overall gain for the X8-2t,

S7-3t and ICE was 55%, 65% and 50% respectively. A list of the ultrasound system settings and gains is provided in appendix A.
After selecting the system settings as described in appendix A, the experiments were carried out. A single experiment consists of a series of scans, which were repeated six times to reduce the influence of stochastic effects. The scans were executed in a fixed order, which is described below:

Step 1: Scanning the grey targets. First, the system settings for this measurement were adjusted according to appendix A. The scanning surface of the UltraiQ general purpose phantom was covered with coupling gel to ensure consistent acoustic coupling. The 'dual' mode was selected on the ultrasound system which enables the user to acquire two images in one screen. First, the probe was positioned such that the -9, -6 and -3 dB appeared in the ultrasound image. When these targets were visible in the image, the 'dual' button was clicked to switch screen. After that, the probe was repositioned, such that the +3, +6 and +15 dB target were visible in the image, and the 'acquire' button was clicked to store both ultrasound acquisitions in one image. This process was repeated 6 times.

Step 2: Scanning the vertical pin group. The settings were adjusted according to appendix A. The probe was repositioned on the scanning surface of the UltraiQ general purpose phantom, such that the line of vertical pins was aligned with the central axis of the ultrasound image. The 'acquire' button was clicked 6 times to store the ultrasound images.

Step 3: Scanning the uniformity phantom The settings were adjusted according to appendix A, and any coupling gel was removed from the transducer. An ultrasound image was acquired holding the probe in air to measure the noise. After acquiring the image in air, the probe was positioned on the scanning surface of the UltraiQ uniformity phantom, and the 'acquire' button was clicked 6 times to store the ultrasound images.

The acquired ultrasound images were stored in DICOM format by the ultrasound system. After finishing the measurement, the DICOM files were exported to USB, and imported in the UltraIQ software. Analysis of the DICOM images with the UltraiQ software yielded the data to quantify the image quality assessment parameters. The data processing is described in the next section.

D. Data Processing

The ultrasound images of the series of scans in the experiments were stored in DICOM format. These DICOM files were imported in the UltraIQ software for analysis. Analysis of the ultrasound images using UltraiQ was used to quantify the image quality parameters. The quantification of these parameters using UltraiQ software is described in this section.

The *contrast resolution* was determined by analysis of the ultrasound images of the grey targets. After the grey target images were imported in the UltraiQ image quality assessment tool, the software automatically created a circular Region Of Interest (ROI) which was manually placed over the grey targets in the image, by clicking on each target in an order from -9dB to +15dB (see figure 3). The UltraiQ software calculated the grey value of each target (GV_T) by averaging pixel grey values within the circular ROI (figure 3B). Knowing the grey value and echo dB value of each target allows to calculate the average increase in grey value per unit change of echo dB value. This grey step per unit change of echo dB is called the "gamma", and is a measure for contrast resolution.

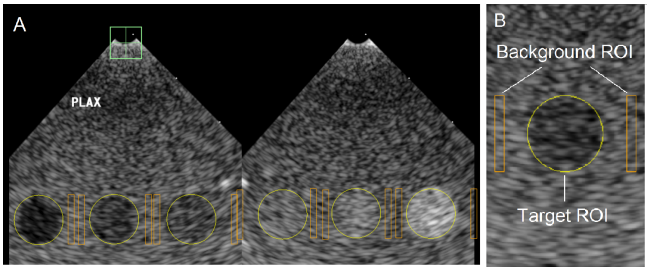

Fig. 3: A: Grey targets in the ultrasound image (-9dB, -6dB, -3dB, 3dB, 6dB, 15dB). **B:** close up of one of the targets. The software automatically calculates the mean value and standard deviation of the grey values in the target ROI and the background ROI. These values are used to determine the contrast resolution and CNR.

The *contrast-to-noise ratio* of each target in figure 3A was calculated according to the definition of CNR in equation 2. The UltraiQ software automatically calculated the mean grey value of each target (GV_T) and background (GV_{BG}), and the the variance of grey values, σ_T^2 and σ_{BG}^2, within the target ROI and background ROI respectively (figure 3B). These values are used to calculate the CNR for each target according to equation 2.

The *spatial resolution* was determined by analysis of the vertical pins in the ultrasound image (figure 4). The images obtained from scanning the vertical pin group were imported in the UltraIQ software. The software automatically created a rectangular ROI that was manually placed over each pin in the image by clicking on it, starting from to upper most pin to the bottom one in the image (see figure 4). After all pins were selected, the software automatically calculated the lateral and axial dimensions of each pin in the image using the 'Full Width, Half Maximum' (FWHM) measurement method. Details of this measurement method are explained in appendix B. The point spread in lateral direction (Δ_L) and axial direction (Δ_A) are a measure for the lateral and axial resolution respectively.

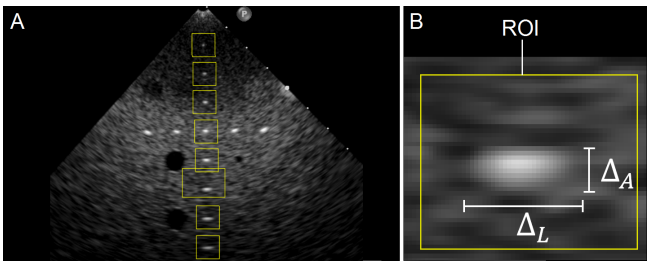

Fig. 4: A Vertical pins in the ultrasound image. **B:** Close-up of one of the pins in the ultrasound image. The software automatically calculates the lateral (Δ_L) and axial (Δ_A) dimension of each pin.

The *penetration depth* of the ultrasound signal was determined by analysis of the "air scan" image (figure 5A) and the "uniform-phantom scan" image (figure 5B). First, the air scan image was loaded in, and a rectangular ROI was placed over the central axis of the ultrasound image (figure 5A). The software automatically calculated the grey levels along the central axis of the ultrasound image

by laterally averaging the grey levels in the ROI. The grey value profile along the central axis of the air-scan image shows the grey values of the noise as a function of depth (d) in the image: $GV_N(d)$. Next, the uniform scan image was loaded in, and the same process was repeated (figure 5B). The grey value profile of the uniform phantom image shows the grey values of the noise added to the echo signal as a function of depth $GV_{S+N}(d)$. The penetration depth was calculated using these values according to the theory as explained in chapter 3 of the thesis document.

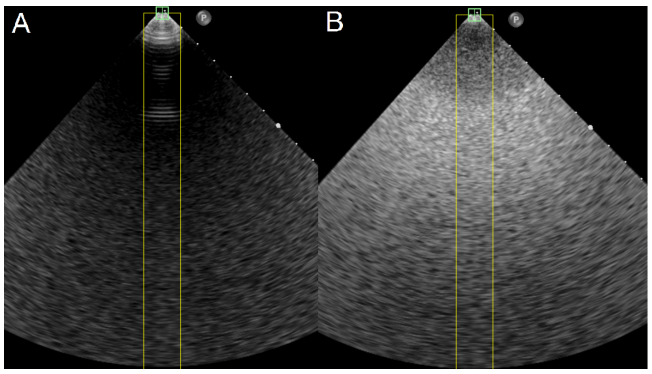

Fig. 5: A: Ultrasound image of the probe in air. **B**: Ultrasound image of the uniform phantom. A rectangular ROI is placed over the central axis of the images, and the laterally averaged grey value profile along the central axis is calculated.

After finishing the analysis of all DICOM images, the results were saved and exported to Excel. A self written MATLAB-function was used to read the data from the Excel file. The output of the MATLAB-function consists of the following figures:

1) The grey value for each grey target dB level (-9dB - +15dB);
2) The contrast-to-noise ratio (CNR) for each grey target (-9dB - +15dB);
3) The axial and lateral dimension of the pins in the ultrasound image;
4) The penetration depth based on the SNR measurement.

IV. Results

Figure 6A shows the measured grey value of each target plotted against the target dB value. In figure 6B, a linear least square regression line is plotted through the datapoints. The errorband indicates the 95% confidence interval of the linear fit. The regression coefficient of the line is defined as the "gamma" (γ), which is a measure for the contrast resolution.

Multiple regression analysis was used to test if the regression coefficient for the ICE probe and the X8-2t probe, and the regression coefficient for the ICE probe and S7-3t probe were significantly different. The gamma of the ICE probe ($\gamma_{\text{ICE}} = 5.0$) and the X8-2t probe ($\gamma_{\text{X8-2t}} = 5.0$) were not significantly different, t(1) = -0.00, p = 0.997. The gamma of the ICE probe ($\gamma_{\text{ICE}} = 5.0$) and the S7-3t probe ($\gamma_{\text{S7-3t}} = 4.2$) were not significantly different, t(1) = -1.11, p = 0.298.

Figure 8 shows the results of the CNR measurements. Data points in the graphs are mean values of the repeated measurements, variance is indicated with the errorband ($\mu \pm \sigma$). No significant difference between the CNR of the ICE ultrasound probe was observed compared to CNR of the X8-2t and S7-3t ultrasound probe, except for the -9 dB target. At the -9 dB target, the CNR of the ICE probe ($\text{CNR}_{\text{ICE}} = 4.3 \pm 0.6$) was higher than the CNR of the X8-2t and S7-3t ($\text{CNR}_{\text{X8-2t}} = 3.2 \pm 0.3, \text{CNR}_{\text{S7-3t}} = 1.4 \pm 0.1$).

The spatial resolution measurements in figure 7A show that the lateral and axial resolution of the ICE ultrasound probe are superior to the lateral and axial resolution of the X8-2t and S7-3t.

The average ratio between the lateral pin size (Δ_L) of the ICE and X8-2t $(\Delta_{\text{L, ICE}}/\Delta_{\text{L, X8-2t}}) = 0.8 \pm 0.2$, and for the S7-3t $(\Delta_{\text{L, ICE}}/\Delta_{\text{L, S7-3t}}) = 0.6 \pm 0.2$.

The average ratio between the axial pin size (Δ_A) of the ICE and X8-2t $(\Delta_{\text{A, ICE}}/\Delta_{\text{A, X8-2t}}) = 0.7 \pm 0.1$, and for the S7-3t $(\Delta_{\text{A, ICE}}/\Delta_{\text{A, S7-3t}}) = 0.7 \pm 0.1$.

It was observed that the lateral resolution of the ICE ultrasound probe strongly depends on imaging plane rotation. Rotating the imaging plane 60^{o} decreases lateral resolution of the ICE ultrasound probe with a factor of approximately 2 (figure 7B). $(\Delta_{\text{L, ICE}}/\Delta_{\text{L, X8-2t}}) = 1.4 \pm 0.3$, and $(\Delta_{\text{L, ICE}}/\Delta_{\text{L, S7-3t}}) = 1.2 \pm 0.2$

Axial resolution was not significantly affected by rotation of the imaging plane 60^{o}. $(\Delta_{\text{A, ICE}}/\Delta_{\text{A, X8-2t}}) = 0.6 \pm 0.1$, and $(\Delta_{\text{A, ICE}}/\Delta_{\text{A, S7-3t}}) = 0.7 \pm 0.1$

Figure 9 shows the results of the ultrasound penetration depth measurements. Ultrasound penetration depth of the ICE ultrasound probe ($\text{PD}_{\text{ICE}} = 70.9 \pm 0.8$ mm) was significantly less as the penetration depth of the X8-2t and S7-3t probe ($\text{PD}_{\text{X8-2t}} = 126.4 \pm 0.7$ mm, $\text{PD}_{\text{S7-3t}} = 100.7 \pm 0.3$ mm).

Details of the measurement results are presented in tables III and IV, Appendix C. Table III contains the results of the grey target scans for each probe. Table IV contains the results of the spatial resolution measurements.

V. Discussion

The results in figure 6 show that mean grey value of the targets increases with dB level, which is as expected. The steepness of the line indicates the change in grey value per step in echo dB level, which is defined as the contrast resolution. Figure 6 shows that contrast resolution of the ICE is not significantly different from the contrast resolution of the X8-2t and S7-3t probe.

The CNR curves in figure 8 have a characteristic U-profile, which is explained by the fact that targets with a lower dB level have a lower contrast with respect to the background and, consequently, have a lower CNR. Figure 10 shows that the -3dB and +3dB targets are barely visible in the surrounding background, which is represented with the low CNR in figure 8.

In general, CNR of the ICE probe is not significantly different from CNR of the X8-2t and S7-3t ultrasound probe, except for the -9dB targets, where the ICE probe has a significantly higher CNR than the S7-3t probe (4.3 ± 0.6 vs. 1.4 ± 0.1)

It is important to note that CNR measurements were performed using targets at a depth of 25 mm below the scanning surface. At this depth, the differences in CNR between the probes are minor. However, at greater depth it is expected that the CNR of the X8-2t, S7-3t and ICE shows larger differences.

The spatial resolution of the ultrasound probe is measured with the axial and lateral dimension of the pins in the ultrasound image. The results of the measurements are shown in figure 7.

As expected, the lateral resolution of the probes changes with depth: the resolution decreases with increasing depth

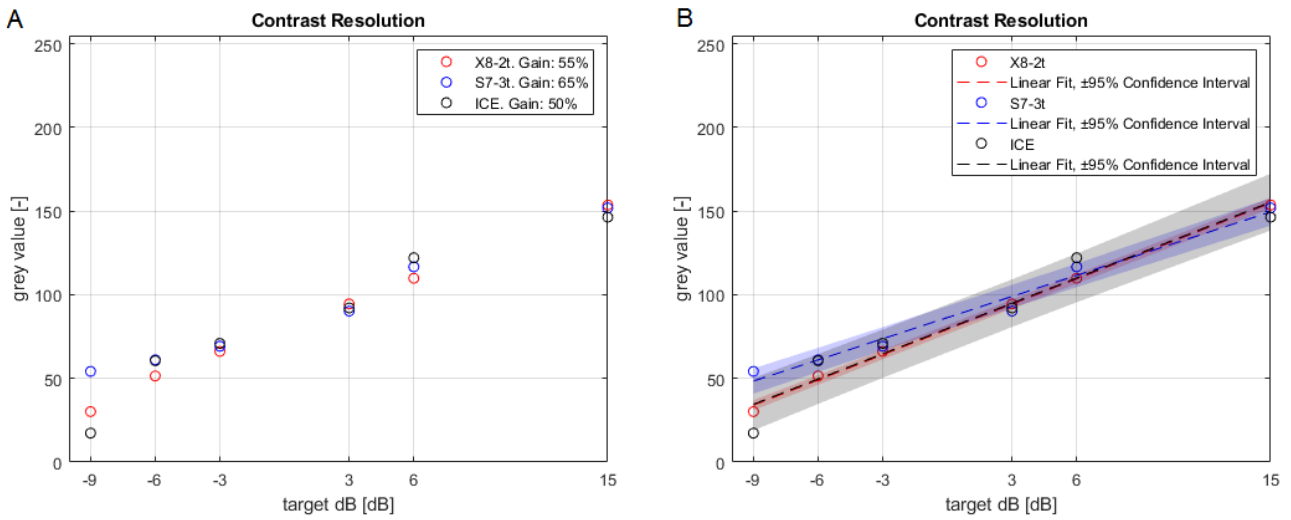

Fig. 6: A: Mean grey value of each target plotted against target echo level (dB). **B:** Linear fit through datapoints, the errorband indicates the 95% confidence interval of the linear fit. Steepness of the line is the contrast resolution of the probe.

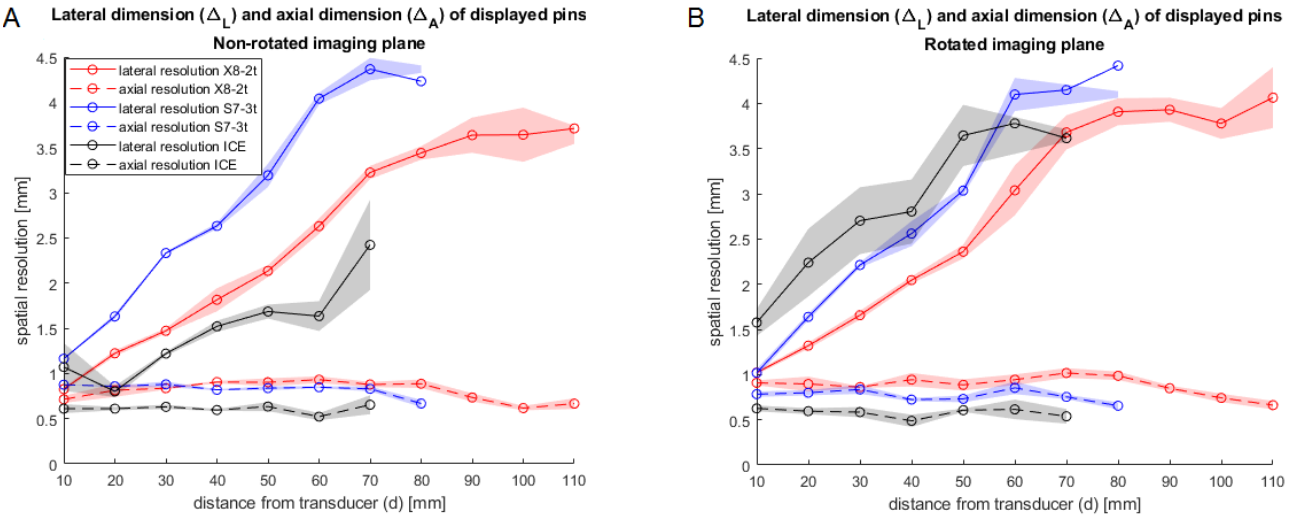

Fig. 7: A: The lateral and axial dimension (Δ_L, Δ_A) [mm] of the pins at depth (d) [mm]. **B:** Axial and lateral resolution of the probes, measured with rotated imaging plane (X8-2t, S7-3t: 90°; ICE: 60°). Data points are mean values of the measurement ($N = 6$), variance is indicated with the errorband ($\mu \pm \sigma$).

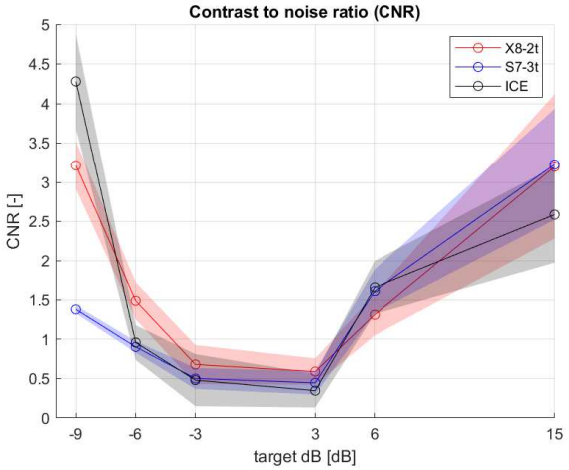

Fig. 8: The contrast-to-noise ratio for the X8-2t, S7-3t and ICE probe. Data points are mean values of the measurement ($N = 6$), variance is indicated with the errorband ($\mu \pm \sigma$).

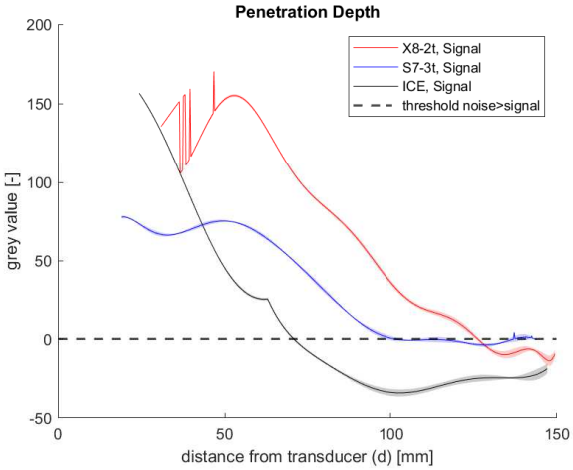

Fig. 9: Penetration depth of the signal. The dashed lines shows the threshold where the signal is lower than the noise (SNR $\leq$ 1).

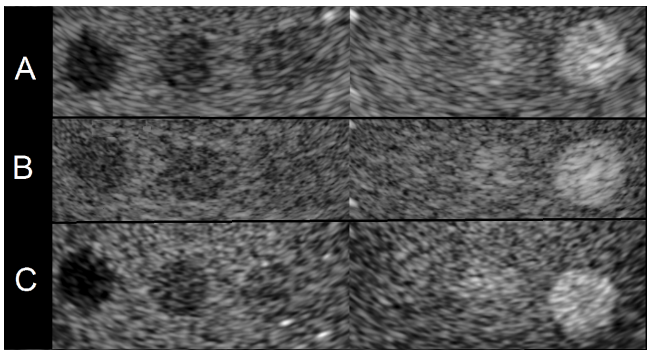

Fig. 10: Ultrasound images of the grey targets. **A**: Ultrasound image acquired with the X8-2t probe, **B**: Ultrasound image acquired with the S7-3t probe, **C**: Ultrasound image acquired with the ICE probe. The target dB from left to right: -9dB, -6dB, -3dB, +3dB, +6dB and +15dB.

(i.e. the lateral dimension of the pins in the image increases). Figure 7A shows that the lateral resolution of the ICE probe is superior to that of the other two probes. However, it is important to mention that the lateral resolution of the ICE probe strongly depends on the rotation angle of the imaging plane, due to the geometry of the transducer array. The transducer array of the ICE has a rectangular shape, which means that more piezo-elements are along the long axis of the array than on the short axis of the array. When the imaging plane is aligned with the long axis of the transducer array (0^o rotation), the maximum amount of elements is involved in forming the image, resulting in maximum achievable image quality. In the worst case, the image plane is rotated 90^o (aligned with the short axis of the rectangular transducer), and a lower amount of piezo-elements is involved in forming the image, resulting in a significantly lower spatial resolution compared to the situation where the image plane is not rotated. The measurement results in figure 7A were obtained with 0^o rotation of the imaging plane. Figure 7B shows the results when the imaging plane of the X8-2t, S7-3t and ICE are rotated 90^o, 90^o, and 60^o respectively. Increasing the image plane rotation angle of the ICE above 60^o resulted in a too low image quality to perform measurements.

Figure 7B shows that the lateral resolution of the ICE decreases with a factor of approximately 2, while the lateral resolution of the X8-2t and S7-3t does not significantly change compared to the results in figure 7A. Lateral resolution of the X8-2t and S7-3t does not change because the transducer array of these probes is designed such that spatial resolution is independent of the image plane rotation angle. Contrary to this, the rectangular design of the transducer array of the ICE results in a strongly rotation angle-dependent spatial resolution.

Figure 7A and 7B show that the axial resolution of the X8-2t, S7-3t and ICE probe does not depend on the imaging plane rotation angle. This is as expected, since the axial resolution is independent of beam geometry. Therefore, rotation of the imaging plane does not affect axial resolution.

Figure 9 shows that the penetration depth of the ICE probe is significantly less compared to the penetration depth of the S7-3t and X8-2t ultrasound probe (70.9 ± 0.8 mm vs. 126.4 ± 0.7 mm, 100.7 ± 0.3 mm). This difference is mainly explained by power (P [W]) and frequency (f [MHz]) of the ultrasound probe. Ultrasound penetration depth decreases exponentially with decreasing power and increasing frequency. The ICE has the lowest penetration depth due to the high frequency and lower power compared to the X8-2t and S7-3t ultrasound probe.

A. Study Limitations and Recommendations

In this study, image quality of the ICE ultrasound probe was compared to the image quality of the Philips X8-2t TEE probe and S7-3t TEE probe. The ICE probe is not intended for TEE imaging, but is developed as a catheter for intracardiac ultrasound imaging. However, since imaging characteristics are likely to be very similar for a TEE probe of the same size as the ICE catheter, results of this study are useful as a first estimate of the image quality of a miniaturized TEE probe. In a follow-up study, the image quality of standard TEE probes can be compared to the miniaturized TEE probe but this was not possible during this study because the miniaturized TEE probe is still under development.

This study did not take into account the effects of the balloon on image quality for trans-balloon ultrasound imaging. It is recommended to perform a follow-up study to investigate the effects of a water-filled balloon on image quality of the ICE miniaturized ultrasound probe.

VI. Conclusion

The ultrasound image quality assessment method developed for this study has proven to be an effective method, with repeatable and consistent results that allow objective comparison of ultrasound probe image quality. In this study, the image quality of the ICE miniaturized ultrasound probe was compared to the image quality of the standard X8-2t TEE probe and S7-3t TEE probe. Image quality was assessed based on measurement of the contrast resolution, contrast-to-noise ratio (CNR), spatial resolution and penetration depth.

Despite its significantly smaller design, the ICE probe performed well compared to X8-2t and S7-3t probe. Contrast resolution and CNR of the probes was not significantly different.

Spatial resolution of the ICE miniaturized ultrasound probe was superior to spatial resolution of the X8-2t and S7-3t, although the lateral resolution of the ICE was strongly limited by imaging plane rotation angle. Rotating the imaging plane significantly reduced the lateral resolution of the ICE ultrasound probe, while lateral resolution of the X8-2t and S7-3t remained unaffected.

A major difference in ultrasound penetration depth was observed between the ICE miniaturized ultrasound probe and the X8-2t and S7-3t. Penetration depth of the ICE probe is 70 mm, where penetration depth of the other probes exceeded 100 mm, with a maximum of 126 mm.

References

[1] J. Thijssen, G. Weijers, and C. de Korte, "Objective performance testing and quality assurance of medical ultrasound equipment.," *Ultrasound in Medicine and Biology*, vol. 33, no. 3, pp. 460–471, 2007.

[2] "Ultrasonics - pulse-echo scanners - techniques for calibrating spatial measurement systems and measurement of system point-spread function response," standard, International Electrotechnical Commission, Geneva, CH, july 2017.

[3] J. T. Bushberg, J. A. Seibert, E. M. Leidholdt, and J. M. Boone, *The Essential Physics of Medical Imaging*. Wolters Kluwer/Lippincott Williams Wilkins, 2012.

[4] “Ultrasonics - pulse-echo scanners - simple methods for periodic testing to verify stability of an imaging system’s elementary performance,” standard, International Electrotechnical Commission, Geneva, CH, july 2016.

APPENDIX A
SYSTEM SETTINGS EPIQ

For consistent comparison of image quality it is important that the image acquisition and image processing settings of the ultrasound system are equal for the probes that are compared. The system settings were adjusted according to the settings listed in table I and II. The settings in table I are the same for all measurements. The gain, scanning depth, focal depth and autoscan are dependent on the measurement and are listed in table II.

TABLE I: System settings for the Epiq. The Touch Screen Module (TSM) on the Epiq has two screens for selecting image aquisition and processing settings. The settings for each screen are shown in the collumns 'TSM screen 1' and 'TSM screen 2'.
* These settings are only applicaple to the X8-2t and ICE probe.

TSM screen 1		**TSM screen 2**	
Chroma Map	'off'	Grey Map	'4'
Harmonics	'off'	Xres	'off'
Quick Angle*	'0'	LGC	'off'
		Autoscan	See table II
Capture Type	'prospective'		
ECG Lead	'II'	Up/Down	'up'
		Left/Right	'left'
View	PLAX2D	Elevation Compounding*	'off'
Xplane	'off'	Temp.	'Celsius'
3D-Zoom	'off'	Temp. Disp.	'on'
Full Volume	'off''		
		Output power	'-0.5dB'
2Dopt	'gen'		
Res/Spd	'middle'		
Compress	'50'		
Loop Length	'2 beats'		
Sector Widht	'max'		
Seek Angle*	'0'		

TABLE II: Measurement dependent system settings.

	Grey Target Measurement	**Vertical Pin Measurement**	**Penetration Depth Measurement**
X8-2t	Gain: 55%	Gain: 55%	Gain: 80%
	Scanning Depth: 50mm	Scanning Depth: 120mm	Scanning Depth: 150mm
	Focal Depth: at targets	Focal Depth: deep	Focal Depth: deep
	Autoscan: 'On'	Autoscan: 'On'	Autoscan: 'Off'
S7-3t	Gain: 65%	Gain: 65%	Gain: 90%
	Scanning Depth: 50mm	Scanning Depth: 120mm	Scanning Depth: 150mm
	Focal Depth: at targets	Focal Depth: deep	Focal Depth: deep
	Autoscan: 'On'	Autoscan: 'On'	Autoscan: 'Off'
ICE	Gain: 50%	Gain: 50%	Gain: 75%
	Scanning Depth: 50mm	Scanning Depth: 91mm	Scanning Depth: 150mm
	Focal Depth: at targets	Focal Depth: deep	Focal Depth: deep
	Autoscan: 'On'	Autoscan: 'On'	Autoscan: 'Off'

APPENDIX B
AXIAL AND LATERAL PIN SIZE MEASUREMENT METHOD

The lateral and axial dimension of the pins were calculated by the UltraiQ image quality assessment software. The software automatically detects the pin in the selected ROI, and determines the central axes of the pin. The lateral and axial pin dimensions are determined by grey value analysis along the horizontal and vertical central axis of the pin respectively. Figure 11 shows an example of the grey value analysis along the lateral axis of one of the pins in the ultrasound image.

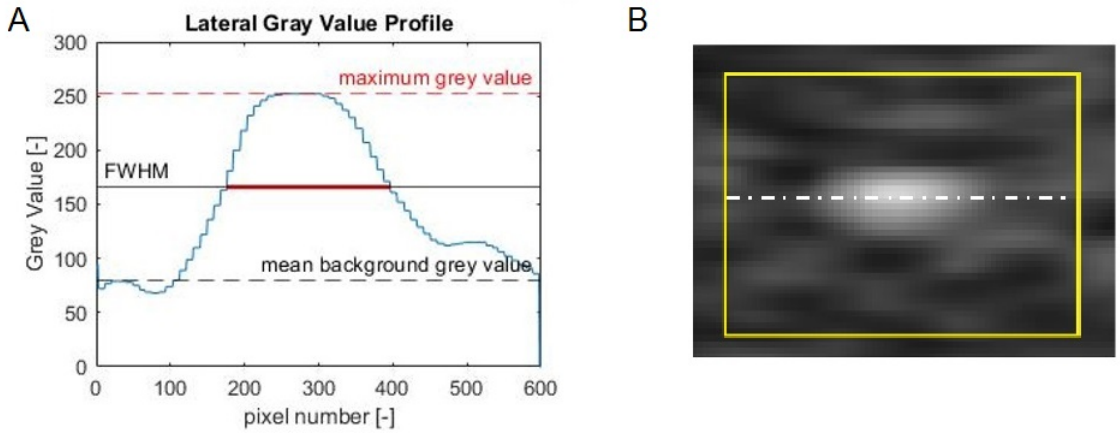

Fig. 11: A:Grey value profile along the lateral axis of one of the pins in the ultrasound image **B**: Close up of the pin, with the lateral axis indicated with the dashed line.

The pixel grey value analysis along the central line of the pin results in a graph representing the grey value of each pixel along that axis (figure 11A). The width of the pin is defined as the width of the grey value curve at the point where the curve intersects a certain threshold. In this thesis, the ”Full-Width, Half-Maximum (FHWM)” threshold was used. The FWHM threshold is standardized by IEC 61391-1 as the threshold for spatial resolution measurement of ultrasound equipment [2].
The maximum grey value along the axis (GV_{max}) and the mean grey value of the background pixels within the ROI (GV_{BG}) are determined. The nominal peak value is the difference between the maximum grey value and the mean background grey value ($GV_{max} - GV_{BG}$). The ’FWHM-width’ is the width of the graph at grey level one half of the nominal peak value above the mean background grey value:

$$GV_{FWHM} = GV_{BG} + \frac{GV_{max} - GV_{BG}}{2} \tag{5}$$

In the example in figure 11, the maximum grey value is 252 (GV_{max} = 252) and the mean background grey value is 80 (GV_{BG} = 80). According to equation 5, the FWHM-grey value is 166. The width of the graph, measured at grey value 166 is 221 pixels; i.e.: the lateral pin size, measured with the FWHM threshold is 221 pixels.
The software calculates the lateral axial dimension of each pin along the line according to the method described above. This yields the lateral and axial resolution of the ultrasound probe, as function of distance from the transducer.

APPENDIX C
MEASUREMENT RESULTS

The results of the measurements are presented in tables III and IV. Table III contains the results of the grey target scans for each probe. Table IV presents the results of the vertical pin scans for each probe. The lateral dimension (Δ_L) and axial dimension (Δ_A) of the displayed pins was calculated with the FWHM threshold.

TABLE III: Results of the grey target scans.

Target dB	**X8-2t** ($\mu \pm \sigma$)	**S7-3t** ($\mu \pm \sigma$)	**ICE** ($\mu \pm \sigma$)
Target Grey Value			
-9	30.2 ± 2.0	54.3 ± 1.6	17.3 ± 1.3
-6	51.5 ± 2.8	61.1 ± 2.5	60.6 ± 2.1
-3	66.1 ± 3.0	69.3 ± 3.4	70.9 ± 3.4
3	94.6 ± 4.4	90.2 ± 1.9	92.1 ± 2.0
6	110 ± 4.03	116.7 ± 2.4	122 ± 1.9
15	154 ± 1.8	151.9 ± 3.1	146 ± 3.5
Contrast to Noise Ratio (CNR)			
-9	3.2 ± 0.3	1.4 ± 0.1	4.3 ± 0.6
-6	1.5 ± 0.3	0.9 ± 0.1	0.9 ± 0.2
-3	0.7 ± 0.2	0.5 ± 0.11	0.5 ± 0.3
3	0.6 ± 0.2	0.5 ± 0.1	0.4 ± 0.1
6	1.3 ± 0.3	1.6 ± 0.3	1.7 ± 0.3
15	3.2 ± 0.9	3.2 ± 0.7	2.6 ± 0.6

TABLE IV: Results of the spatial resolution measurements.

D [mm]	**X8-2t**		**S7-3t**		**ICE**	
	Δ_L **[mm]** ($\mu \pm \sigma$)	Δ_A **[mm]** ($\mu \pm \sigma$)	Δ_L **[mm]** ($\mu \pm \sigma$)	Δ_A **[mm]** ($\mu \pm \sigma$)	Δ_L **[mm]** ($\mu \pm \sigma$)	Δ_A **[mm]** ($\mu \pm \sigma$)
10	0.8 ± 0.0	0.7 ± 0.0	1.2 ± 0.1	0.9 ± 0.0	1.1 ± 0.3	0.6 ± 0.0
20	1.2 ± 0.0	0.8 ± 0.1	1.6 ± 0.0	0.9 ± 0.1	0.8 ± 0.1	0.6 ± 0.0
30	1.4 ± 0.0	0.8 ± 0.0	2.3 ± 0.0	0.9 ± 0.0	1.2 ± 0.0	0.6 ± 0.0
40	1.8 ± 0.1	0.9 ± 0.0	2.6 ± 0.0	0.8 ± 0.0	1.5 ± 0.1	0.6 ± 0.0
50	2.1 ± 0.1	0.9 ± 0.0	3.2 ± 0.1	0.8 ± 0.0	1.7 ± 0.2	0.6 ± 0.0
60	2.6 ± 0.1	0.9 ± 0.0	4.0 ± 0.1	0.8 ± 0.0	1.6 ± 0.2	0.5 ± 0.0
70	3.2 ± 0.1	0.9 ± 0.0	4.4 ± 0.1	0.8 ± 0.0	2.4 ± 0.5	0.7 ± 0.1
80	3.4 ± 0.1	0.9 ± 0.0	$4.2 \pm --$	0.7 ± 0.0	$--$	$--$
90	3.6 ± 0.2	0.7 ± 0.0	$--$	$--$	$--$	$--$
100	3.6 ± 0.3	0.6 ± 0.0	$--$	$--$	$--$	$--$
110	$3.7 \pm --$	0.7 ± 0.1	$--$	$--$	$--$	$--$

Appendix B

Article 2

Objective Image Quality Assessment of Ultrasound Probes used for Trans Esophageal Echocardiography (TEE) - Report II

Grandia, L.

Abstract— **Miniaturized, trans-balloon transesophageal echocardiography (TEE) potentially improves intraprocedural imaging of atrial ablation procedures. Current state of the art TEE probes are not sufficient for intraprocedural imaging of ablation procedures due to discomfort for the patient and limitations in the field of view. In this thesis study, miniaturized, trans-balloon TEE is proposed as imaging modality for AF ablation procedures. A water-filled balloon around the transducer of a miniaturized TEE probe serves as primary coupling medium between transducer and esophageal wall. This study aims to investigate the influence of the water-filled balloon on image quality, by comparison of trans-balloon ultrasound image quality with direct ultrasound image quality. Ultrasound image quality was assessed based on objective image quality analysis of ultrasound phantom scans. The results of this study have shown that contrast resolution, contrast-to-noise ratio (CNR), spatial resolution and penetration depth are not significantly influenced by the water-filled balloon.**

Keywords—Trans Balloon Miniaturized Ultrasound, Image quality, Objective assessment, Performance testing, UltraIQ

I. Introduction

This article is part of a MSc thesis research study. The goal of the thesis is to investigate the feasibility of miniaturized, trans-balloon, trans-esophageal echocardiography (TEE) as imaging modality for intraprocedural monitoring of atrial fibrillation (AF) ablation procedures.

During AF ablation procedures, real time imaging of the cardiac structure and the ablation catheters is required in order to perform ablation accurately. Effectiveness and success rates of ablation procedure strongly depend on the accuracy of ablation. Currently used TEE probes are not suitable for real time imaging during ablation, due to their high level of discomfort for the patient, and limitations in the field of view (FOV).

In this thesis research it is proposed that miniaturized, trans-balloon TEE can provide real time imaging of the cardiac anatomy during ablation procedures, which potentially improves efficacy and outcome of AF ablation procedures.

A water-filled balloon is required to ensure acoustic coupling between the esophageal wall and transducer of the miniaturized probe. The current state of the art TEE probes have a large transducer with a diameter of approximately 1-1.5 cm. The miniaturized ultrasound probe has a diameter of only 3 mm, which makes it almost impossible to achieve consistent acoustic coupling without using a water filled balloon around the transducer as primary coupling medium. In a previous study of this thesis, it was validated that image quality of the miniaturized ultrasound probe is comparable to the image quality of the currently used TEE probes. However, this study did not take into account the effect of the balloon around the transducer of the miniaturized ultrasound probe.

A. Research Objective

This research aims to compare trans-balloon ultrasound image quality to image quality of ultrasound images obtained without a balloon around the transducer, using the miniaturized ultrasound probe. The results of this study are used in a feasibility study of trans-balloon miniaturized TEE imaging for intraprocedural imaging of AF ablation procedures.

II. Materials

A. Image Quality Assessment Phantoms

Standardized ultrasound image quality assessment phantoms were used for measurement of the image quality. Image quality parameters were quantified by objective analysis of the ultrasound images of these phantoms.

Contrast resolution and spatial resolution were measured using the UltraIQ general purpose ultrasound phantom (CablonMedical, Leusden, Netherlands). The attenuation coefficient and speed of sound of the phantom base material are similar to those in parenchymal soft tissue (0.5 dB/(cm·Mhz) $\pm 5\%$ and 1450 m/s respectively). The base material contains a vertically aligned group of 'pins', and a group of 6 echogenic, cylindrical grey targets. Each grey target reflects the incident ultrasound signal with a specific echo intensity (I_T). The background material reflects the incident ultrasound signal with intensity (I_{BG}). The echo intensity of the targets (I_T) with respect to the echo intensity of the background (I_{BG}) is expressed in decibel (dB):

$$\text{target dB level} = 10 \cdot \log\left(\frac{I_T}{I_{BG}}\right) \tag{1}$$

The echogenic grey targets have a relative echo intensity with respect to the background of -9dB, -6dB, -3dB, 3dB, 6dB and 15dB respectively. The distance between the center of the targets and the surface of the phantom is 25 mm (figure 1).
Penetration depth of the ultrasound signal was measured using the UltraiQ uniformity phantom (CablonMedical, Leusden, Netherlands). This phantom consists of a block of uniform echogenic material without any targets.

B. Ultrasound Probe

The Intra-Cardiac Echocardiography (ICE) ultrasound catheter (Philips, Alajuela, Costa-Rica) was used as a miniaturized ultrasound probe for trans-balloon ultrasound image quality measurements (figure 2). The ICE catheter is a 3 mm diameter ultrasound catheter, that was initially developed for intra-cardiac ultrasound imaging. Due to its small size, this ultrasound catheter can also serve as miniaturized ultrasound probe for TEE imaging.

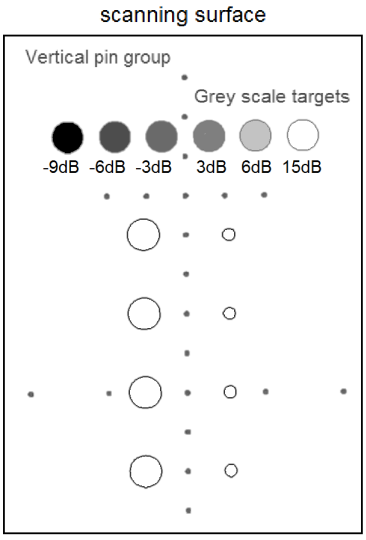

Fig. 1: The target pattern in the UltraIQ General Purpose Phantom (Cablon Medical, Leusden, Netherlands).

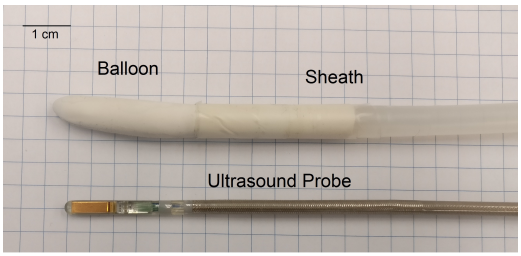

Fig. 2: The miniaturized ultrasound probe (Intra-Cardiac Echocardiography (ICE) ultrasound catheter, Philips, Alajuela, Costa-Rica). For measurement of trans-balloon ultrasound image quality, the probe was inserted in a polymer sheath with a water-filled balloon at the end.

C. Test Setup

The miniaturized ultrasound probe was inserted in a water-filled balloon for measurement of trans-balloon ultrasound image quality. The ultrasound probe was inserted in a 1/4 inch o.d. plastic sheath (48636955, MSC Industrial Direct Co., Melville, NY, USA), with a latex balloon at the distal end of the sheath. On the proximal end of the sheath was a union tee connected (48622088, MSC Industrial Direct Co., Melville, NY, USA). This union tee was connected to a reducer connector, which provided an air- and water tight seal around the shaft of the ultrasound probe. The branch of the union tee connector was connected to a piece of 1/4" o.d. plastic tubing, which was air- and water tight connected to a 140 mL syringe (22257152, FisherScientific, Hampton, NH, USA).

When the catheter was inserted through the sealing connector at the proximal end of the plastic sheath, the catheter was advanced until the probe head was inside the balloon at the distal end of the plastic sheath. The balloon was inflated and deflated with water using the syringe, which was connected to the system via the union tee. Figure 3 provides a schematic overview of the catheter inserted in the tubing system.

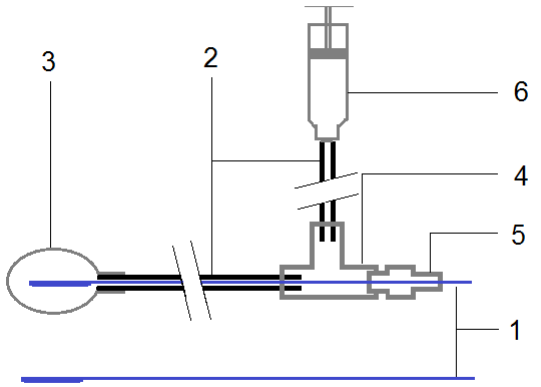

Fig. 3: Schematic of the test setup to measure trans-balloon ultrasound image quality. The miniaturized ultrasound probe (1) was inserted in a plastic tube sheath (2), with a latex balloon (3) at the distal end of the sheath. A union tee (4) was connected at the proximal end of the sheath. A reducer connector (5) in the union tee provided an air- and water tight seal around the shaft of the miniaturized ultrasound probe (1). The branch of the tee connector (4) was via a plastic tube connected to a 140 mL, water-filled syringe (6).

D. Ultrasound System and Software

The ultrasound images were acquired and stored in DICOM format using the Epiq 7Ci Ultrasound system (Philips, Bothell, WA, USA). The DICOM images were analyzed with the UltraIQ ultrasound image quality assessment software (CablonMedical, Leusden, Netherlands). The results of the UltraIQ software were stored in Excel, and imported in MATLAB (R2018b) to visualize the data in graphs.

III. Methods

A. Image Quality Parameters

Image quality of the miniaturized ultrasound probe with balloon around the transducer was compared to image quality of the probe without balloon around the transducer based on measurement of the following image quality parameters: contrast resolution, contrast-to-noise ratio (CNR), spatial resolution and penetration depth.

The *contrast resolution* is defined as the smallest difference in echo intensity of a target (I_T) with respect to the echo intensity of the surrounding background (I_{BG}) that can be detected in the ultrasound image [1]. The contrast resolution depends on the mapping of echo intensity (I), to grey values (GV) in the ultrasound image. Good contrast resolution means that objects with low difference in echo intensity w.r.t. background ($I_T/I_{BG} \approx 1$), still can be resolved in the ultrasound image ($GV_T/GV_{BG} > 1$). Contrast resolution is determined by measuring the "gamma", defined as the increase in grey level per dB echo level (grey value/echo dB).

The *contrast-to-noise ratio* (CNR) is the contrast between background and target divided by the noise in the image [1]. The contrast between background and target is the absolute difference between the mean grey value in the target (GV_T) and the mean grey value in the background (GV_{BG}). The noise is the variance in pixel grey values within the target (σ_T^2) and background (σ_{BG}^2). The ratio between the contrast and the noise yields the CNR:

$$\text{CNR} = \frac{|GV_T - GV_{BG}|}{\sqrt{\sigma_T^2 + \sigma_{BG}^2}} \quad (2)$$

Spatial resolution is defined as the smallest distance between two closely spaced objects in the ultrasound image that can be resolved as separate. Points spaced closer as the spatial resolution cannot be resolved as two distinct points in the image. The spatial resolution of an ultrasound probe is determined by measuring the width of the point spread function (PSF) in axial and lateral direction. [1, 3]. Spatial resolution of ultrasound images is measured with 'axial resolution' and 'lateral resolution'.

The *penetration depth* (PD) of the ultrasound signal is defined as the depth in the ultrasound image where the signal-to-noise ratio (SNR) drops below one.
SNR is defined as the amplitude of the signal squared (A_S^2) divided by the amplitude of the noise in the signal (A_N^2) squared [4]:

$$\text{SNR} = \frac{A_S^2}{A_N^2} \quad (3)$$

Since the signal (amplitude of the returning echos) decreases with depth, and the noise originating from electronic components and signal amplification is depth-independent, the SNR decreases with depth. The depth where SNR is lower than one is the penetration depth of the ultrasound signal [5]:

$$\text{PD} := \text{SNR} < 1 \quad (4)$$

B. Experimental Design

In this study, two experiments were performed:
Experiment 1: scanning the image quality assessment phantoms with the miniaturized ultrasound probe, *without* a balloon around the transducer;
Experiment 2: scanning the image quality assessment phantoms with the miniaturized ultrasound probe, *with* a balloon around the transducer.

A single experiment consists of a series of scans on the ultrasound image quality assessment phantoms. The scans were repeated $N = 20$ times to reduce the influence of stochastic effects.

C. Measurement Protocol

Prior to conducting the experiments the imaging settings of the ultrasound system were selected. To observe the influence of the transducer balloon on image quality only, the influence of image acquisition and processing parameters had to be excluded. Therefore, ultrasound image acquisition and processing parameters were equal across all experiments. Imaging settings are listed in appendix A.
Prior to executing the measurements of the second experiment (with balloon), the ultrasound probe was inserted in the sheath, and the balloon was filled with water by depressing the plunger of the syringe. In the first experiment (without balloon) this step was not applicable. After the system settings are adjusted as listed in appendix A, the image quality measurements were caried out. Within a single experiment, the measurements were repeated twenty times ($N = 20$). The scans were executed in a specific order, which is described below:

Step 1: Scanning the grey targets. First, the system settings for this measurement were adjusted according to appendix A. The scanning surface of the UltraiQ general purpose phantom was covered with coupling gel to ensure consistent acoustic coupling. The 'dual' mode was selected on the ultrasound system which enables the user to acquire two images in one screen. First, the probe was positioned such that the -9, -6 and -3 dB appeared in the ultrasound image. When these targets were visible in the image, the 'dual' button was clicked to switch screen. After that, the probe was repositioned, such that the +3, +6 and +15 dB target were visible in the image, and the 'acquire' button was clicked to store both ultrasound acquisitions in one image. This process was repeated 20 times.

Step 2: Scanning the vertical pin group. The settings were adjusted according to appendix A. The probe was repositioned on the scanning surface of the UltraiQ general purpose phantom, such that the line of vertical pins was aligned with the central axis of the ultrasound image. The 'acquire' button was clicked 20 times to store the ultrasound images.

Step 3: Scanning the uniformity phantom The settings were adjusted according to appendix A, and any coupling gel was removed from the transducer. An ultrasound image was acquired holding the probe in air to measure the noise. After acquiring the image in air, the probe was positioned on the scanning surface of the UltraiQ uniformity phantom, and the 'acquire' button was clicked 20 times to store the ultrasound images.

The acquired ultrasound images were stored in DICOM format by the ultrasound system. After finishing the measurement, the DICOM files were exported to USB, and imported in the UltraIQ software. Analysis of the DICOM images with the UltraiQ software yielded the data to quantify the image quality assessment parameters. The data processing is described in the next section.

D. Data Processing

The ultrasound images of the series of scans in the experiments were stored in DICOM format. These DICOM files were imported in the UltraiQ software for analysis. Analysis of the ultrasound images using UltraiQ was used to quantify the image quality parameters. The quantification of these parameters using UltraiQ software is described in this section.

The *contrast resolution* was determined by analysis of the ultrasound images of the grey targets. After the grey target images were imported in the UltraiQ image quality assessment tool, the software automatically created a circular Region Of Interest (ROI) which was manually placed over the grey targets in the image, by clicking on each target in an order from -9dB to +15dB (see figure 4). The UltraiQ software calculated the grey value of each target (GV_T) by averaging grey values of the pixels within the circular ROI (figure 4B). Knowing the grey value and echo dB value of each target allows to calculate the average increase in grey value per unit change of echo dB value. This grey step per unit change of echo dB is called the "gamma", and is a measure for contrast resolution.

The *contrast-to-noise ratio* of each target in figure 4A was calculated according to the definition of CNR in equation 2. The UltraiQ software automatically calculated the mean grey value of each target (GV_T) and background (GV_{BG}), and the the variance of grey values, σ_T^2 and σ_{BG}^2, within the target ROI and background ROI respectively (figure 4B). These values were used to calculate the CNR for each target according to equation 2.

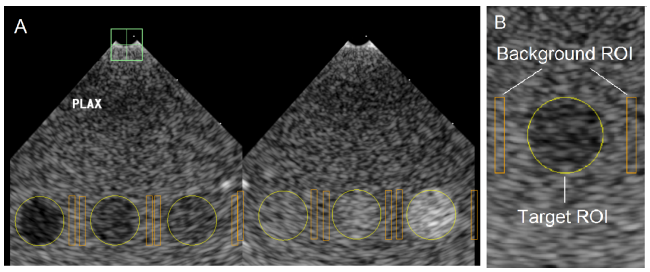

Fig. 4: A: Grey targets in the ultrasound image (-9dB, -6dB, -3dB, 3dB, 6dB, 15dB). **B:** close up of one of the targets. The software automatically calculates the mean value and standard deviation of the grey values in the target ROI and the background ROI. These values are used to determine the contrast resolution and CNR.

The *spatial resolution* was determined by analysis of the vertical pins in the ultrasound image (figure 5). The images obtained from scanning the vertical pin group were imported in the UltraIQ software. The software automatically created a rectangular ROI that was manually placed over each pin in the image by clicking on it, starting from to upper most pin to the bottom one in the image (see figure 5). After all pins were selected, the software automatically calculated the lateral and axial dimensions of each pin in the image using the 'Full Width, Half Maximum'(FWHM) measurement method. Details of this measurement method are explained in appendix B. The point spread in lateral direction (Δ_L) and axial direction (Δ_A) are a measure for the lateral and axial resolution respectively.

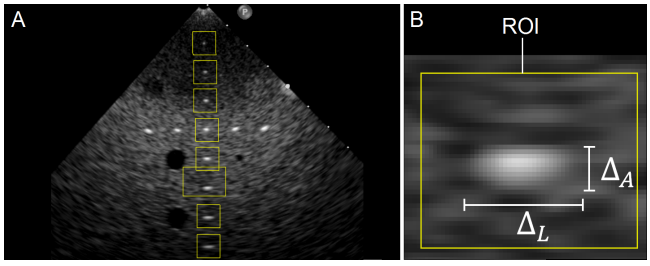

Fig. 5: A Vertical pins in the ultrasound image. **B:** Close-up of one of the pins in the ultrasound image. The software automatically calculates the lateral (Δ_L) and axial (Δ_A) dimension of each pin.

The *penetration depth* of the ultrasound signal was determined by analysis of the "air scan" image (figure 6A) and the "uniform-phantom scan" image (figure 6B). First, the air scan image was loaded in, and a rectangular ROI was placed over the central axis of the ultrasound image (figure 6A). The software automatically calculated the grey levels along the central axis of the ultrasound image by laterally averaging the grey levels in the ROI. The grey value profile along the central axis of the air-scan image shows the grey values of the noise as a function of depth (d) in the image: $GV_N(d)$. Next, the uniform scan image was loaded in, and the same process was repeated (figure 6B). The grey value profile of the uniform phantom image shows the grey values of the noise added to the echo signal as a function of depth $GV_{S+N}(d)$. The penetration depth was calculated using these values according to the theory as explained in chapter 3 of the thesis document.

After finishing the analysis of all DICOM images, the results were saved and exported to Excel. A MATLAB-function file was used to read the data from the Excel file, and present the data in figures.

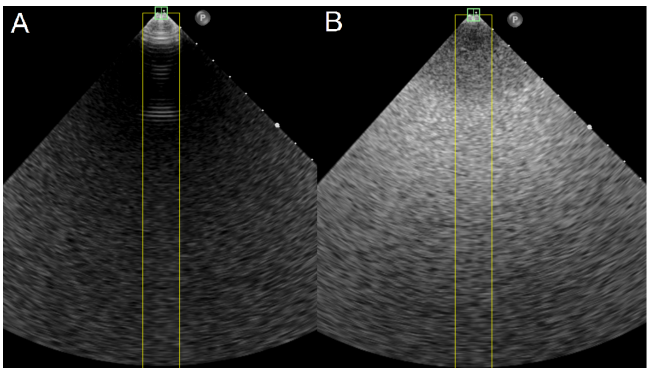

Fig. 6: A: Ultrasound image of the probe in air. **B**: Ultrasound image of the uniform phantom. A rectangular ROI is placed over the central axis of the images, and the laterally averaged grey value profile along the central axis is calculated.

IV. Results

In general, no significant influence of the balloon on image quality was observed.

Figure 8A shows the measured grey value of each target plotted against the target dB value. Figure 8B shows a linear least-square regression line through the datapoints in figure 8A. The errorband indicates the 95% confidence interval of the linear fit. The regression coefficient of the line is defined as the "gamma" (γ), which is a measure for the contrast resolution.

Multiple regression analysis was used to test if the regression coefficient for the ICE probe without balloon and the ICE probe with balloon are significantly different. The gamma of the ICE probe without balloon ($\gamma_{\text{ICE, no balloon}} = 5.1$) and the ICE probe with balloon ($\gamma_{\text{ICE, balloon}} = 5.0$) were not significantly different, t(1) = 0.11, p = 0.913.

Figure 9 shows the results of the CNR measurements. No significant difference in CNR was observed between the two experimental conditions.

The spatial resolution measurements in figure 7 show no significant influence of the balloon around the transducer on spatial resolution.

The average ratio between the lateral pin size (Δ_L) of the ICE probe with balloon and without balloon was $(\Delta_{\text{L, balloon}}/\Delta_{\text{L, no balloon}}) = 1.1 \pm 0.1$,

The average ratio between the axial pin size (Δ_A) of the ICE probe with balloon and without balloon was $(\Delta_{\text{A, balloon}}/\Delta_{\text{A, no balloon}}) = 1.0 \pm 0.1$.

Figure 10 shows the penetration depth of the probe with and without balloon. No significant difference between the penetration depth of the ICE ultrasound probe without balloon (69.8 ± 1.8 mm) and the ICE ultrasound probe with balloon (71.1 ± 1.3 mm) was observed, t(1) = 1.43, p = 0.185.

Details of the measurement results are presented in tables III and IV, Appendix C. Table III contains the results of the grey target scans for each probe. Table IV contains the results of the spatial resolution measurements.

V. Discussion

In this study, the image quality of a miniaturized ultrasound probe was compared to the image quality of

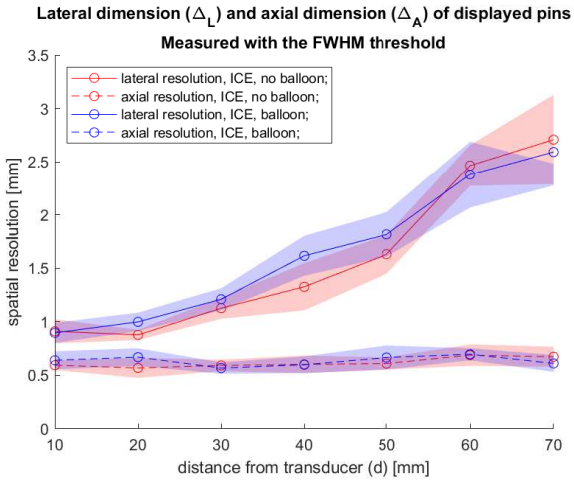

Fig. 7: The lateral and axial dimension (Δ_L, Δ_A) [mm] of the pins at depth (d) [mm]. The solid line represents the lateral dimension, the dashed line represents the axial dimension. Data points are mean values of the measurements ($N = 20$), variance is indicated with the errorband ($\mu \pm \sigma$).

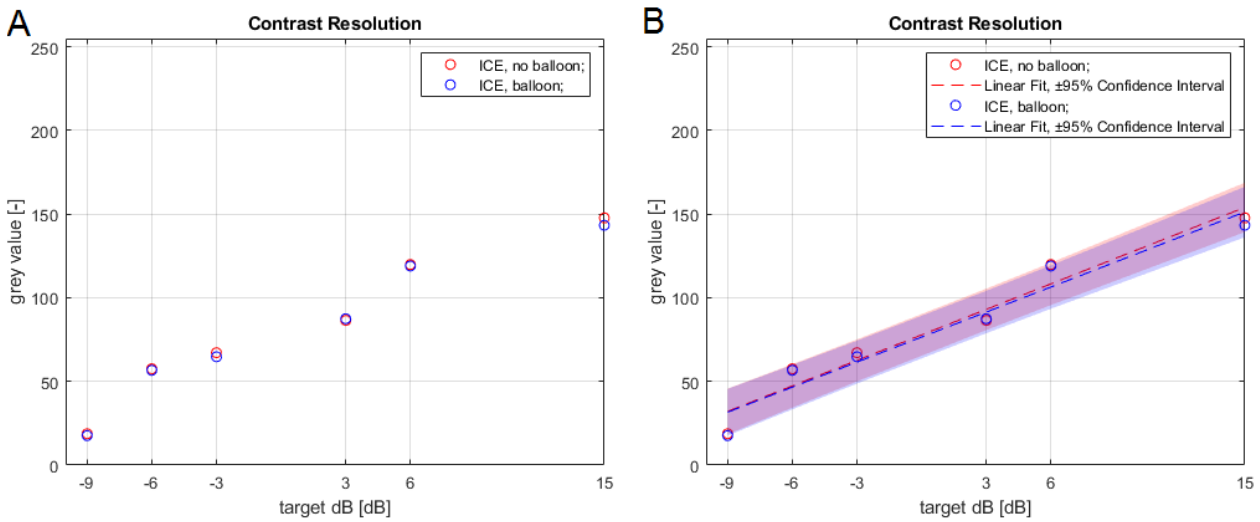

Fig. 8: A: Mean grey value of each target plotted against target echo level (dB). B: Linear fit through datapoints, the errorband indicates the 95% confidence interval of the linear fit. Steepness of the line is the contrast resolution of the probe.

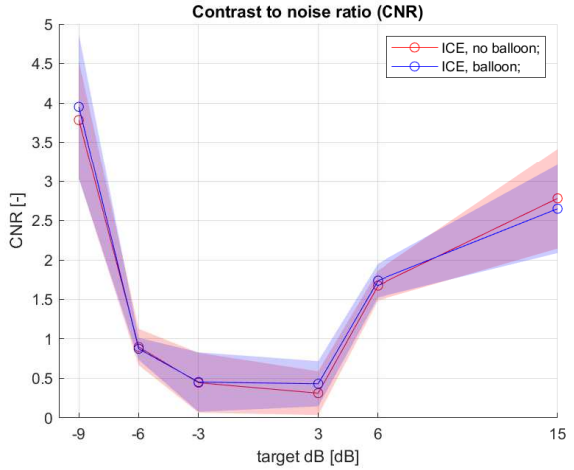

Fig. 9: The contrast-to-noise ratio for the ICE probe without balloon and with balloon around the transducer. Data points are mean values of the measurements ($N = 20$), variance is indicated with the errorband ($\mu \pm \sigma$).

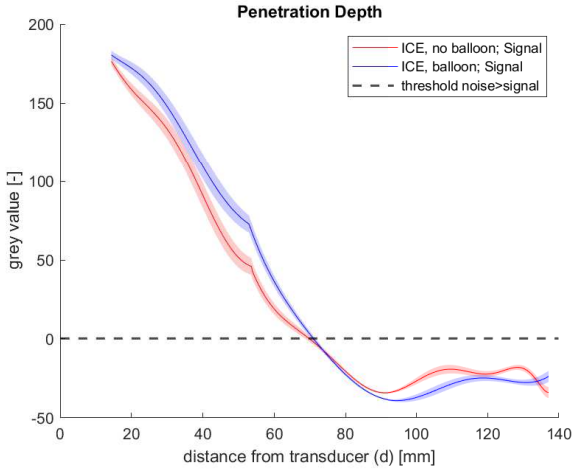

Fig. 10: Penetration depth of the signal. The dashed lines shows the threshold where the signal is lower than the noise (SNR $\leq$ 1). Data points are mean values of the measurements ($N = 20$), variance is indicated with the errorband ($\mu \pm \sigma$).

an intra-balloon miniaturized ultrasound probe to study the influence of the balloon on image quality. The results have shown that the balloon did not negatively influence image quality.

Compared to direct ultrasound imaging, trans-balloon ultrasound imaging adds extra interfaces between the transducer and the insonated tissue: the ultrasound waves travel from the transducer in medium inside the balloon (water), than from the medium into the balloon wall, and from the balloon wall into the insonated tissue. It was expected that these extra interfaces would absorb some of the ultrasound energy, which results in a lower ultrasound image quality. However, the results have shown that the influence of the water-filled balloon on image quality are negligible.

A. *Study Limitations and Recommendations*

A major limitation to the aforementioned observations is that the balloon was inflated with only 10 ml of water, which does not fully deploy the balloon. For the intended application of trans-balloon TEE imaging, the water-filled balloon needs to be inflated to a diameter of approximately 20 mm (30 ml).

The reason why the balloon was not further inflated, was that inflating the balloon to a diameter of 20 mm induced severe mirroring artifacts of the balloon wall, which influenced the image quality such that measurements could not be performed. It was observed that these artifacts became stronger with increasing balloon diameter. Therefore, it was decided to perform measurements with a minimum diameter of the balloon.

The mirroring artifacts are due to the balloon-air interface where the balloon is not in contact with the scanning surface of the phantom. At this interface, all scattered ultrasound waves are reflected back, and are detected by the transducer as an echo. This echo causes an artifact in the image (see figure 11).

It is expected that these mirroring artefacts will not occur when the balloon is inserted in the esophagus, because the esophageal wall entirely surrounds the balloon. This means that scattered ultrasound signals will be absorbed in the tissue, and will not reflect on the balloon-air interface as it was the case in the measurement setup.

It is recommended to perform a follow-up study, where the balloon is inserted in a phantom with a tubular cavity that entirely surrounds the balloon to validate whether this reduces the mirroring artifacts.

VI. Conclusion

This study has shown that contrast resolution, CNR, spatial resolution and penetration depth are not negatively influenced by a water-filled balloon around the transducer of a miniaturized ultrasound probe. Inflating the water-filled balloon to a diameter of 20 mm induced strong artifacts in the ultrasound image, but it is expected that these effects are specific to the measurement setup, and will not occur when the balloon is inserted in the esophagus.

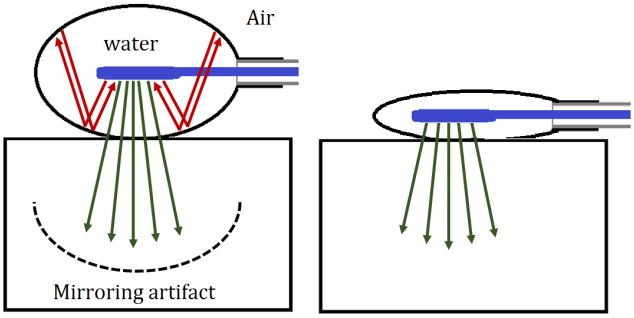

Fig. 11: When the balloon was fully inflated, mirroring of the balloon wall causes artifacts in the ultrasound image. These mirroring effects occur from reflected ultrasound waves at the balloon-air interface, where the balloon is not in contact with the phantom surface. It was observed that deflating the balloon reduced the mirroring artifacts.

References

[1] J. Thijssen, G. Weijers, and C. de Korte, "Objective performance testing and quality assurance of medical ultrasound equipment.," *Ultrasound in Medicine and Biology*, vol. 33, no. 3, pp. 460–471, 2007.

[2] Z. Long, D. Tradup, S. Stekel, K. Gorny, and H. N.J., "Evaluations of ultraiq software for objective ultrasound image quality assessment using images from a commercial scanner," *Journal of Applied Medical Physics*, vol. 19, no. 2, pp. 298–304, 2018.

[3] "Ultrasonics - pulse-echo scanners - techniques for calibrating spatial measurement systems and measurement of system point-spread function response," standard, International Electrotechnical Commission, Geneva, CH, july 2017.

[4] J. T. Bushberg, J. A. Seibert, E. M. Leidholdt, and J. M. Boone, *The Essential Physics of Medical Imaging*. Wolters Kluwer/Lippincott Williams Wilkins, 2012.

[5] "Ultrasonics - pulse-echo scanners - simple methods for periodic testing to verify stability of an imaging system's elementary performance," standard, International Electrotechnical Commission, Geneva, CH, july 2016.

APPENDIX A
SYSTEM SETTINGS EPIQ

For consistent comparison of image quality it is important that the image acquisition and image processing settings of the ultrasound system are equal for the probes that are compared. The system settings were adjusted according to the settings listed in table I and II. The settings in table I are the same for all measurements. The gain, scanning depth, focal depth and autoscan are dependent on the measurement and are listed in table II.

TABLE I: System settings for the Epiq. The Touch Screen Module (TSM) on the Epiq has two screens for selecting image aquisition and processing settings. The settings for each screen are shown in the collumns 'TSM screen 1' and 'TSM screen 2'.
* These settings are only applicaple to the X8-2t and ICE probe.

TSM screen 1		**TSM screen 2**	
Chroma Map	'off'	Grey Map	'4'
Harmonics	'off'	Xres	'off'
Quick Angle*	'0'	LGC	'off'
		Autoscan	See table II
Capture Type	'prospective'		
ECG Lead	'II'	Up/Down	'up'
		Left/Right	'left'
View	PLAX2D	Elevation Compounding*	'off'
Xplane	'off'	Temp.	'Celsius'
3D-Zoom	'off'	Temp. Disp.	'on'
Full Volume	'off''		
		Output power	'-0.5dB'
2Dopt	'gen'		
Res/Spd	'middle'		
Compress	'50'		
Loop Length	'2 beats'		
Sector Widht	'max'		
Seek Angle*	'0'		

TABLE II: Measurement dependent system settings.

	Grey Target Measurement	**Vertical Pin Measurement**	**Penetration Depth Measurement**
ICE, no balloon	Gain: 50%	Gain: 55%	Gain: 75%
	Scanning Depth: 50mm	Scanning Depth: 91mm	Scanning Depth: 150mm
	Focal Depth: at targets	Focal Depth: deep	Focal Depth: deep
	Autoscan: 'On'	Autoscan: 'On'	Autoscan: 'Off'
ICE, balloon	Gain: 50%	Gain: 55%	Gain: 75%
	Scanning Depth: 50mm	Scanning Depth: 91mm	Scanning Depth: 150mm
	Focal Depth: at targets	Focal Depth: deep	Focal Depth: deep
	Autoscan: 'On'	Autoscan: 'On'	Autoscan: 'Off'

APPENDIX B
AXIAL AND LATERAL PIN SIZE MEASUREMENT METHOD

The lateral and axial dimension of the pins were calculated by the UltraiQ image quality assessment software. The software automatically detects the pin in the selected ROI, and determines the central axes of the pin. The lateral and axial pin dimensions are determined by grey value analysis along the horizontal and vertical central axis of the pin respectively. Figure 12 shows an example of the grey value analysis along the lateral axis of one of the pins in the ultrasound image.

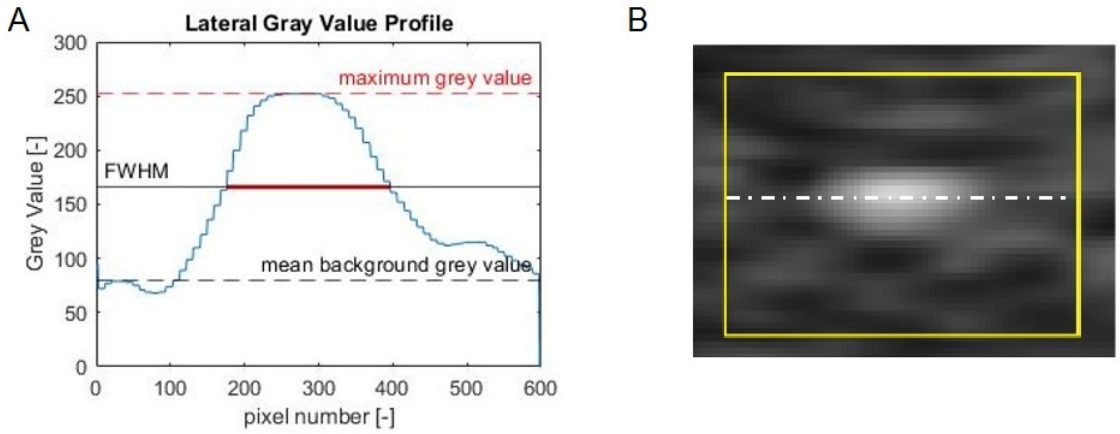

Fig. 12: A:Grey value profile along the lateral axis of one of the pins in the ultrasound image **B**: Close up of the pin, with the lateral axis indicated with the dashed line.

The pixel grey value analysis along the central line of the pin results in a graph representing the grey value of each pixel along that axis (figure 12A). The width of the pin is defined as the width of the grey value curve at the point where the curve intersects a certain threshold. In this thesis, the ”Full-Width, Half-Maximum (FHWM)” threshold was used. The FWHM threshold is standardized by IEC 61391-1 as the threshold for spatial resolution measurement of ultrasound equipment [3].
The maximum grey value along the axis (GV_{max}) and the mean grey value of the background pixels within the ROI (GV_{BG}) are determined. The nominal peak value is the difference between the maximum grey value and the mean background grey value ($GV_{max} - GV_{BG}$). The ’FWHM-width’ is the width of the graph at grey level one half of the nominal peak value above the mean background grey value:

$$GV_{FWHM} = GV_{BG} + \frac{GV_{max} - GV_{BG}}{2} \tag{5}$$

In the example in figure 12, the maximum grey value is 252 (GV_{max} = 252) and the mean background grey value is 80 (GV_{BG} = 80). According to equation 5, the FWHM-grey value is 166. The width of the graph, measured at grey value 166 is 221 pixels; i.e.: the lateral pin size, measured with the FWHM threshold is 221 pixels.
The software calculates the lateral axial dimension of each pin along the line according to the method described above. This yields the lateral and axial resolution of the ultrasound probe, as function of distance from the transducer.

APPENDIX C
MEASUREMENT RESULTS

The results of the measurements are presented in tables III andIV. Table III contains the results of the grey target scans for each probe. Table IV presents the results of the vertical pin scans for each probe. The lateral dimension (Δ_L) and axial dimension (Δ_A) of the displayed pins was calculated with the FWHM threshold.

TABLE III: Results of the grey target scans.

Target dB	**ICE, no balloon** ($\mu \pm \sigma$)	**ICE, balloon** ($\mu \pm \sigma$)
	Target Grey Value	
-9	18.7 ± 2.6	17.6 ± 5.5
-6	57.6 ± 2.4	56.7 ± 2.6
-3	67.2 ± 4.5	64.8 ± 6.7
3	86.5 ± 4.9	87.5 ± 12.9
6	120 ± 3.6	119 ± 3.1
15	148 ± 3.3	143 ± 7.7
	Contrast to Noise Ratio (CNR)	
-9	2.6 ± 0.7	2.8 ± 0.9
-6	1.9 ± 0.3	2.0 ± 0.1
-3	0.8 ± 0.4	0.7 ± 0.4
3	0.4 ± 0.3	0.5 ± 0.3
6	1.3 ± 0.2	1.3 ± 0.2
15	3.7 ± 0.6	3.4 ± 0.6

TABLE IV: Results of the spatial resolution measurements.

D [mm]	**ICE, no balloon**		**ICE, balloon**	
	Δ_L **[mm]** ($\mu \pm \sigma$)	Δ_A **[mm]** ($\mu \pm \sigma$)	Δ_L **[mm]** ($\mu \pm \sigma$)	Δ_A **[mm]** ($\mu \pm \sigma$)
10	0.9 ± 0.1	0.6 ± 0.0	0.9 ± 0.1	0.6 ± 0.1
20	0.9 ± 0.0	0.6 ± 0.1	1.0 ± 0.1	0.7 ± 0.1
30	1.1 ± 0.1	0.6 ± 0.1	1.2 ± 0.1	0.6 ± 0.1
40	1.3 ± 0.2	0.6 ± 0.1	1.6 ± 0.2	0.6 ± 0.1
50	1.6 ± 1.2	0.6 ± 0.1	1.8 ± 0.2	0.7 ± 0.1
60	2.5 ± 0.2	0.7 ± 0.1	2.4 ± 0.3	0.7 ± 0.1
70	2.7 ± 0.4	0.7 ± 0.1	2.6 ± 0.2	0.6 ± 0.1

Appendix C

Balloon and Sheath System for Trans-Balloon US Imaging

Trans-balloon image quality of the Philips Intra-Cardiac Echocardiography (ICE) probe was measured using the balloon and sheath system described in this appendix.

The ICE ultrasound probe (1) was inserted in a 1/4 inch outer diameter plastic sheath (2), with a latex balloon (3) at the distal end of the sheath. On the proximal end of the sheath was a union tee connected (4). This union tee was connected to a reducer connector (5), which provided an air- and water tight seal around the shaft of the ICE ultrasound probe. The branch of the union tee connector was connected to a piece of 1/4 inch outer diameter plastic sheath (4), which was air- and water tight connected to a 140 ml syringe (6). The components of the tubing setup are listed in table C-1. A schematic drawing of the tubing system is provided in figure C-2. A photo of the tubing system is provided in C-3. A detail photo of the tee connector is provided in figure C-1.

Depressing the plunger of the syringe allowed to inflate the balloon with water. In the deflated state, the balloon was filled with approximately 10 ml of water (figure C-4). Inflating the balloon with 30 ml, increased the diameter of the balloon to approximately 20 mm (figure C-5).

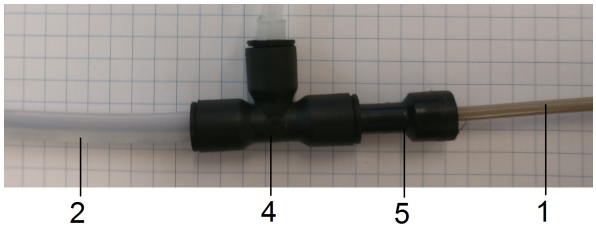

Figure C-1: A tee connector (4) was attached at the proximal end of the plastic sheath (2). A reducer connector (5) was connected to the tee connector to provide a water- and air- tight seal with the shaft of the ICE catheter (1).

Table C-1: Components of the test setup for measuring trans-balloon ultrasound image quality

Component Number	Component Description
1	Philips Intra-Cardiac Echocardiography (ICE) probe (Philips Healthcare, Alajuela, Costa-Rica)
2	1/4 inch outer diameter plastic sheath (48636955, MSC Industrial Direct Co., Melville, NY, USA)
3	latex balloon
4	union tee connector (48622088, MSC Industrial Direct Co., Melville, NY, USA)
5	reducer connector (62378609, MSC Industrial Direct Co., Melville, NY, USA)
6	syringe (22257152, FisherScientific, Hampton, NH, USA)

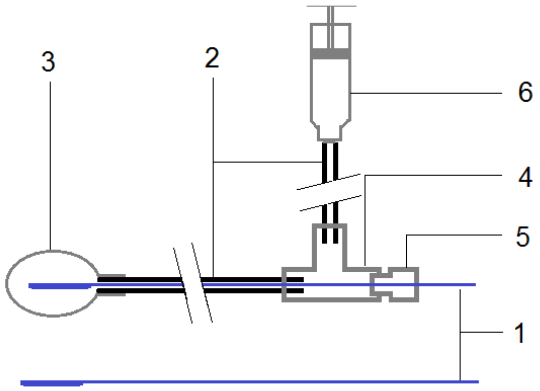

Figure C-2: Sketch of the setup. The ICE probe (1) was inserted in a plastic tube sheath (2), with a latex balloon (3) at the distal end of the sheath. A union tee (4) was connected at the proximal end of the sheath. A reducer connector (5) in the union tee provided an air- and water tight seal around the shaft of the miniaturized ultrasound probe (1). The branch of the tee connector (4) was via a plastic tube connected to a 140 mL, water-filled syringe (6)

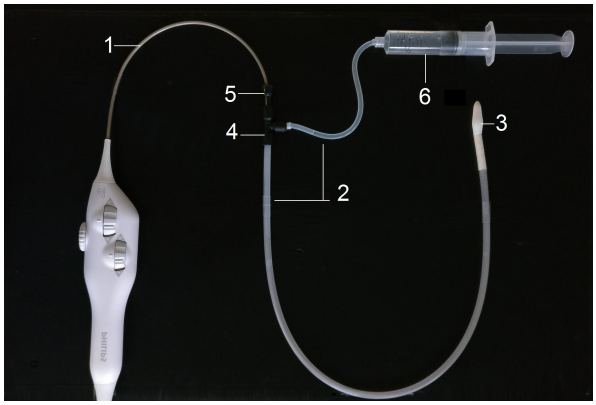

Figure C-3: Photo of the setup. The ICE probe (1) was inserted in a plastic tube sheath (2), with a latex balloon (3) at the distal end of the sheath. A union tee (4) was connected at the proximal end of the sheath. A reducer connector (5) in the union tee provided an air- and water tight seal around the shaft of the miniaturized ultrasound probe (1). The branch of the tee connector (4) was via a plastic tube connected to a 140 mL, water-filled syringe (6)

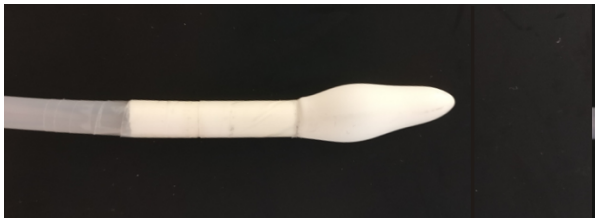

Figure C-4: Balloon in deflated state (filled with 10 ml water).

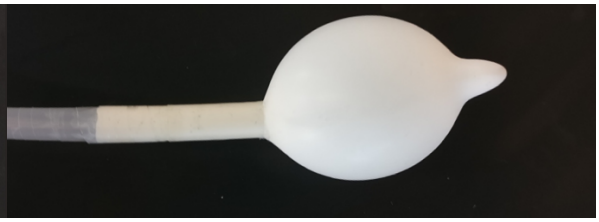

Figure C-5: Balloon in inflated state (filled with 30 ml water), diameter is 20 mm.

Bibliography

[1] A. Jaidkja, H. Hobbs, S. Koenig, S. Millington, and R. Arntfield, "Better With Ultrasound, Transesophageal Echocardiography," *Chest*, vol. 155, no. 1, pp. 194–201, 2019.

[2] V. Fridman and M. J. Garcia, *Practical Manual of Echocardiography in the Urgent Setting*. Wiley-Blackwell, 2013.

[3] E. N. Marieb and K. Hoehn, *Human Anatomy and Physiology*. Pearson, 2014.

[4] A. Haak, *Augmenting Electrophysiology Interventions with Advanced 3D Transesophageal Echocardiography*. PhD thesis, Erasmus University Rotterdam, 2015.

[5] Z. Starek, F. Lehar, J. Jez, M. Scurek, J. Wolf, T. Kulik, and A. Zbankova, "Esophageal Positions Relative to the Left Atrium; Data from 293 Patients before Catheter Ablation of Atrial Fibrillation," *Indian Heart Journal*, vol. 70, no. 1, pp. 37–44, 2017.

[6] D. Sanchez Quintana, J. Cabrera, J. Farre, M. Mendonca, and S. Ho, "Anatomic Relations between the Esophagus and Left Atrium and Relevance for Ablation of Atrial Fibrillation.," *Circulation*, vol. 112, no. 10, pp. 1400–1405, 2005.

[7] H. Tsao, W. Mei-Han, H. Satoshi, L. Kun-Tai, T. Ching-Tai, H. Nai-Wei, C. Cheng-Yen, and C. Shih-Ann, "Anatomic Relationship of the Esophagus and Left Atrium," *Chest*, vol. 128, no. 4, pp. 2581–2587, 2005.

[8] "Philips X8-2t TEE probe." https://www.philips.co.uk/healthcare/resources/feature-detail/ultrasound-tee-imaging. Accessed: 2019-06-14.

[9] J. T. Bushberg, J. A. Seibert, E. M. Leidholdt, and J. M. Boone, *The Essential Physics of Medical Imaging*. Wolters Kluwer/Lippincott Williams Wilkins, 2012.

[10] L. Smith, R. Dworakowski, A. Bhan, I. Delithanasis, J. Hancock, P. MacCarthy, O. Wendler, M. Thomas, and M. Monaghan, "Real-Time Three-Dimensional Transesophageal Echocardiography Adds Value to Transcatheter Aortic Valve Implantation," *Journal of the American Society of Echocardiography*, vol. 26, no. 4, pp. 359–369, 2013.

[11] J. Ender and S. Sgouropoulou, "Value of transesophageal echocardiography (TEE) guidance in minimally invasive mitral valve surgery," *Anals of Cardiothoracic Surgery*, vol. 2, no. 6, pp. 796–802, 2013.

[12] S. Biner, S. Kar, R. Siegel, A. Rafique, and T. Shiota, "Value of Color Doppler Three-Dimensional Transesophageal Echocardiography in the Percutaneous Closure of Mitral Prosthesis Paravalvular Leak," *The American Journal of Cardiology*, vol. 105, no. 7, pp. 984–989, 2010.

[13] R. Hahn, M. Nabaur, M. Zuber, M. Nazif, J. Hausleiter, M. Taramasso, A. Pozzoli, I. George, S. Kodali, V. Bapat, and F. Maisano, "Intraprocedural Imaging of Transcatheter Tricuspid Valve Interventions," *JACC Cardiovascular Imaging*, vol. 12, no. 3, pp. 532–553, 2019.

[14] F. Faletra, L. Biasco, G. Pedrazzini, M. Moccetti, E. Pasotti, L. Leo, G. Cautilli, T. Moccetti, and M. Monaghan, "Echocardiographic-Fluoroscopic Fusion Imaging in Transseptal Puncture: A New Technology for an Old Procedure," *Journal of the American Society of Echocardiography*, vol. 30, no. 9, pp. 886–895, 2017.

[15] F. Faletra, G. Nucifora, F. Regoli, S. Ho, T. Moccetti, and A. Auricchio, "Anatomy of pulmonary veins by real-time 3D TEE: implications for catheter-based pulmonary vein ablation.," *Journal of the American College of Cardiology*, vol. 5, no. 4, pp. 456–462, 2012.

[16] F. Faletra, S. Ho, and A. Auricchio, "Anatomy of right atrial structures by real-time 3D transesophageal echocardiography.," *Journal of the American College of Cardiology*, vol. 3, no. 9, pp. 966–975, 2010.

[17] A. Ames and W. Stevenson, "Catheter Ablation of Atrial Fibrillation," *Circulation*, vol. 113, no. 13, pp. 666–668, 2006.

[18] J. E. P. Waktare, "Atrial Fibrillation," *Circulation*, vol. 106, no. 1, pp. 14–16, 2002.

[19] F. Musharbash, M. Schill, L. Sinn, R. Schuessler, H. Maniar, M. Moon, S. Melby, and R. Damiano, "Performance of the Cox-maze IV procedure is associated with improved long-term survival in patients with atrial fibrillation undergoing cardiac surgery," *Journal of Thoracic and Cardiovascular Surgery*, vol. 155, no. 1, pp. 159–170, 2017.

[20] N. Calvo, L. Mont, B. Vidal, M. Nadal, S. Montserrat, D. Andreu, D. Tamberro, C. Pare, M. Azqueta, A. Berruezo, J. Brugada, and M. Sitges, "Usefulness of transoesophageal echocardiography before circumferential pulmonary vein ablation in patients with atrial fibrillation: is it really mandatory?," *Europace*, vol. 13, no. 6, pp. 486–491, 2011.

[21] A. Brooks, M. Stiles, J. Laborderie, D. Lau, P. Kuklik, N. Shipp, L. Hsu, and P. Sanders, "Outcomes of long-standing persistent atrial fibrillation ablation: A systematic review," *Heart Rythm*, vol. 7, no. 6, pp. 835–846, 2010.

[22] K. Kettering, F. Gramley, and S. Bardeleben, "Catheter ablation of atrial fibrillation facilitated by preprocedural three-dimensional transesophageal echocardiography: Long-term outcome," *World Journal of Cardiology*, vol. 9, no. 6, pp. 539–546, 2017.

[23] F. Faletra, S. Ho, F. Regoli, M. Acena, and A. Auricchio, "Real-time three dimensional transoesophageal echocardiography in imaging key anatomical structures of the left atrium: Potential role during atrial fibrillation ablation," *Heart*, vol. 99, no. 2, pp. 133–142, 2013.

[24] J. Kautzner and P. Peichl, "The role of imaging to support catheter ablation of atrial fibrillation," *Cor et Vasa*, vol. 54, no. 6, pp. e375–e385, 2012.

[25] T. Skala and M. Taborsky, "Electromechanical mapping in electrophysiology and beyond," *Cor et Vasa*, vol. 57, no. 10, pp. 470–482, 2015.

[26] H. Calkins, G. Hindricks, R. Cappato, Y. Kim, E. Saad, L. Aguinaga, J. Akar, V. Badhwar, J. Brugada, J. Camm, P. Chen, S. Chen, M. Chung, J. Nielsen, A. Curtis, D. Davies, J. Day, and A. Avila, "2017 HRS/EHRA/ECAS/APHRS/SOLAECE expert consensus statement on catheter and surgical ablation of atrial fibrillation.," *Heart Rythm*, vol. 14, no. 10, pp. 275–444, 2017.

[27] M. Nilesh, "Role of TEE before atrial fibrillation ablation: Is less really more?," *Heart Rhythm*, vol. 13, no. 1, p. 20, 2015.

[28] S. Stec, B. Zaborska, M. Sikora-Frac, T. Krynski, and P. Kulakowski, "First experience with microprobe transoesophageal echocardiography in nonsedated adults undergoing atrial fibrillation ablation: Feasibility study and comparison with intracardiac echocardiography," *Europace*, vol. 13, no. 1, pp. 51–56, 2011.

[29] T. Bunch and J. Day, "Examining the Risks and Benefits of Transesophageal Echocardiogram Imaging During Catheter Ablation for Atrial Fibrillation," *Circulation: Arrhythmia and Electrophysiology*, vol. 5, no. 4, pp. 621–623, 2012.

[30] A. Babkin, P. Littrup, and S. Kovalcheck, "Endoesophageal balloon catheter, system, and related method," september 2016. US20160249859A1.

[31] E. Begot, F. Dalmay, C. Etchecopar, M. Clave, N. Pichon, B. Francois, R. Lang, and P. Vignon, "Hemodynamic assessment of ventilated ICU patients with cardiorespiratory failure using a miniaturized multiplane transesophageal echocardiography probe," *Intensive Care Medicine*, vol. 41, no. 11, pp. 1886–1894, 2015.

[32] S. Perveen, V. Dhir, R. Paramasivam, M. Hossain, M. A. Ahmed, and A. Maydeo, "Endoscopic Ultrasound : A New Hope for Patients," *Journal of Bangladesh College of Physicians and Surgeons*, vol. 33, no. 1, pp. 23–31, 2014.

[33] S. Raman, E. Fishman, and A. Lennon, "Endoscopic ultrasound and pancreatic applications: What the radiologist needs to know," *Abdominal Imaging*, vol. 38, no. 6, pp. 1360–1372, 2013.

[34] J. Thijssen, G. Weijers, and C. de Korte, "Objective Performance Testing and Quality Assurance of Medical Ultrasound Equipment," *Ultrasound in Medicine and Biology*, vol. 33, no. 3, pp. 460–471, 2007.

[35] "Ultrasonics - pulse-echo scanners - simple methods for periodic testing to verify stability of an imaging system's elementary performance," standard, International Electrotechnical Commission, Geneva, CH, july 2016.

[36] "Ultrasonics - pulse-echo scanners - techniques for calibrating spatial measurement systems and measurement of system point-spread function response," standard, International Electrotechnical Commission, Geneva, CH, july 2017.

[37] H. Grazhdani, E. David, O. Spagnolo, F. Buemi, A. Perri, N. Orsogna, S. Gigli, and R. Chimenz, "Quality assurance of ultrasound systems: current status and review of literature," *Journal of Ultrasound*, vol. 21, no. 3, pp. 173–182, 2018.

[38] J. Thijssen, M. van Wijk, and M. Cuypers, "Performance testing of medical echo/Doppler equipment," *European Journal of Ultrasound*, vol. 15, pp. 151–164, 2002.

[39] Z. Long, D. Tradup, S. Stekel, K. Gorny, and H. N.J., "Evaluations of UltraiQ software for objective ultrasound image quality assessment using images from a commercial scanner," *Journal of Applied Medical Physics*, vol. 19, no. 2, pp. 298–304, 2018.

[40] "UltraiQ General Purpose Phantoms." https://cablon.nl/producten/ultraiq-general-purpose-phantoms-en/. Accessed: 2019-05-15.

[41] H. N.J., S. Stekel, D. Tradup, K. Gorny, and D. King, "Four-year experience with a clinical ultrasound quality control program.," *Ultrasound in Medicine and Biology*, vol. 37, no. 8, pp. 1350–1357, 2011.

[42] W. Zhou, D. Tradup, S. Stekel, J. Browne, D. Brown, and H. N.J., "Ultrasound grayscale image quality comparison between a 2D intracavitary transducer and a 3D intracavitary transducer used in 2D mode: A phantom study," *Journal of Applied Clinical Physics*, pp. 1–7, 2019.

[43] K. Gorny, D. Tradup, and H. N.J., "Implementation and validation of three automated methods for measuring ultrasound maximum depth of penetration: Application to ultrasound quality control.," *Medical Physics*, vol. 32, no. 8, pp. 2615–2628, 2005.

[44] D. Dausch, K. Gilchrist, J. Carlson, S. Hall, J. Castelluci, and O. Ramm, "In Vivo Real-Time 3D Intracardiac Echo Using PMUT Arrays," *IEEE Transactions on Ultrasonics, Ferroelectrics and Frequency Control*, vol. 61, no. 10, pp. 1754 – 1764, 2014.

[45] R. Hahn, T. Abraham, M. Adams, C. Cruce, E. Glas, R. Lang, S. Reeves, J. Shanewise, S. Siu, W. Stewart, and M. Picard, "Guidelines for Performing a Comprehensive Transesophageal Echocardiographic Examination: Recommendations from the American Society of Echocardiography and the Society of Cardiovascular Anesthesiologists," *Journal of the American College of Cardiology*, vol. 26, no. 9, pp. 921–964, 2013.

[46] M. Hlaing, J. He, N. Haglund, H. Takayama, and B. Flynn, "Impact of a Monoplane Hemodynamic TEE (hTEE) Monitoring Device on Decision Making in a Heterogeneous Hemodynamically Unstable Intensive Care Unit Population: A Prospective, Observational Study," *Journal of Cardiothoracic Vascular Anesthesiology*, vol. 32, no. 3, pp. 1308–1313, 2018.

[47] C. Dietrich, Jenssen, and F. C. Herth, "Endobronchial ultrasound elastography," *Endoscopic Ultrasound*, vol. 5, no. 4, pp. 233–238, 2016.

Glossary

List of Acronyms

EP electrophysiology

TEE Transesophageal Echocardiography

ICE Intra-Cardiac Echocardiography

CT Computerized Tomography

MRI Magnetic Resonance Imaging

LA Left Atrium

RA Right Atrium

LV Left Ventricle

RV Right Ventricle

PV Pulmonary Veins

LSPV Left Superior Pulmonary Vein

LIPV Left Inferior Pulmonary Vein

RSPV Right Superior Pulmonary Vein

RIPV Right Inferior Pulmonary Vein

AF Atrial Fibrillation

AV atrioventricular

SA sinoatrial

SHD Structural Heart Disease

FOV Field of View

IQA Image Quality Assessment

CNR Contrast-to-Noise Ratio

SNR Signal-to-Noise Ratio

ROI Region of Interest

PSF Point Spread Function

SPL Spatial Pulse Length

PRP Pulse Repetition Period

PRF Pulse Repetition Frequency

FAM Fast Anatomical Mapping

EBUS Endobronchial Ultrasound